UNIVERSITY OF CALIFORNIA
RIVERSIDE

Novel Materials and Methodologies for Surface-Based Label-Free Analysis of Biomolecular Interactions

A Dissertation submitted in partial satisfaction
of the requirements for the degree of

Doctor of Philosophy

in

Chemistry

by

Cole Pattric Ebel

June 2026

Dissertation Committee:
Dr. Quan Cheng, Chairperson
Dr. Joseph Genereux
Dr. Linlin Zhao

The Dissertation of Cole Pattric Ebel is approved:

Committee Chairperson

University of California, Riverside

Acknowledgements

What an honor and privilege it has been to attend, learn, teach, and grow as an individual and scientist here at the University of California Riverside. I can't imagine where I would be today without the opportunity provided to me by this institution and all of the wonderful people who keep it running. I hope the following acknowledgements will convey even a fraction of the gratitude I have for the individuals that made this possible. I'd like to begin by expressing my appreciation for the most integral person in guiding me during this journey, my advisor and mentor professor Quan Jason Cheng.

Dr. Cheng, when I first entered the program here I had no idea what to expect beyond what was presented by online anecdotes that depict graduate school as a miserable and grueling marathon. However, what I found here is that while it is no doubt challenging to obtain a PhD, the process can be an immensely enjoyable and rewarding experience if a lab culture is fostered to encourage collaboration, companionship, and personal development. Your ability to guide us the best versions of ourselves in such a positive environment is a testament to your quality as an advisor and mentor. I want to extend my sincere thanks for your unwavering support in improving my abilities and confidence as a scientist and making the entire experience something I can forever look back upon with a smile.

I now must extend my thanks to the wonderful group of lab mates that I've worked in close collaboration with over the past five years. Each person mentioned below played a part, big or small, in making this all possible, and for that I am forever grateful. Lambert,

not only were you a fantastic teacher and colleague, but you were the person who convinced me to join the group, invariably changing the course of my life. Santino, it was great sharing our little corner of the lab where your endless curiosity and enthusiasm for science inspired me every day. Daniel, you were the bedrock of the lab for much of my time here, and I doubt I could have made it this far without your guidance and friendship. Malinick, you not only made coming to the lab every day so much fun, but without you I never would have met the love of my life. Xin, I'd like to thank you for bringing such a bright presence in the lab every day and for all of your assistance in learning the ropes of the biosafety lab. Victor, you've been a great colleague to teach and learn from, and I've always appreciated and tried to replicate the confidence you bring to every situation. Westley, you're not only one of the most capable and hardworking scientists I've met, but I also consider you to be a close friend. Without your help, I don't think I'd be half as successful as a scientist or Counter-Strike player.

To my family, but my parents first and foremost, thank you for your endless support. At no point did I receive anything other than unwavering encouragement to pursue higher education and knowing I always had your support gave me the confidence to tackle this challenging and uncertain opportunity. To my awesome group of friends, Joaquin, Jesse, Khristian, and Al, to name a few, thanks for keeping my spirits (and humility) high. To Paris, meeting you was not only the highlight of my time here, but it was the best thing to happen in my entire life. It is such a blessing to have a counterpart who understands me perfectly at both a personal and professional level. Thanks for your endless support, advice, companionship, and most of all, thanks for always pretending to like my cooking.

Copyright Acknowledgement

Portions of figure 1.8 were reprinted, with permission, from *J. Phys. D: Appl. Phys.* **2014**, 48, 18, 184001 and *Nanotechnology* **2017**, 28, 46, 465704.

Portions of the text and figures of Chapter 2 were adapted from *ACS Appl. Nano Mater.* **2025**, 8, 48, 23237–23246. This chapter was supported by collaboration with Daniel Stuart, Santino Valiulis, Westley Van Zant, and Quan Cheng. The corresponding author, Dr. Quan Jason Cheng, directed and supervised the research that formed the basis of that chapter.

The work presented in Chapter 3 was supported by the material and intellectual contributions of Dr. Carlo Baggio and Dr. Maurizio Pellecchia.

The text and figures of Chapter 4 were adapted from our manuscript titled "Ganglioside-Mediate Membrane Diffusion and Effects on EGFR Regulation in Highly Controlled Biomimetic Systems Enabled by Chemoenzymatic Synthesis" that is, at the time of this writing, submitted to *Chem. Sci*. First authorship is shared with Dr. Arin Gucchait, whose lab conducted the synthesis and characterization of the ganglioside library utilized in the work. This work was further supported by contributions from coauthors Hai Yu, Westley Van Zant, Victor Hanson, and Daniel Stuart. The corresponding authors Dr. Quan Jason Cheng and Dr. Xi Chen directed and supervised the research that formed the basis of that chapter.

ABSTRACT OF THE DISSERTATION

Novel Materials and Methodologies for Surface-Based Label-Free Analysis of Biomolecular Interactions

by

Cole Pattric Ebel

Doctor of Philosophy, Graduate Program in Chemistry
University of California, Riverside, June 2026
Dr. Quan Cheng, Chairperson

Biosensing technology represents a core and often underappreciated pillar upon which most of the major discoveries in the life sciences rest. The development of new biosensing materials and methodologies has continually enabled life-saving advancements in medical diagnostics, drug discovery, and environmental monitoring, to name only a few major areas. Surface-based biosensing techniques mark a major subclass of biosensors, ranging from the simple colorimetric lateral flow assays found in COVID-19 tests to powerful techniques used for characterizing the binding behavior of a broad range of biological interactions. Among these is surface plasmon resonance (SPR), a highly sensitive real-time biosensing modality that has been used extensively in the fields of drug discovery, vaccine research, toxicology, and fundamental explorations of other biophysical interactions. The aim of the work presented in this dissertation is the advancement of all major aspects of the SPR sensing workflow, including the underlying plasmonic materials,

the sensing biointerface, and experimental design. These developments enable, and are utilized in combination with, numerous other analytical techniques for the exploration of previously unanswered biophysical questions.

Chapter 2 presents the development and application of the rarely explored metal of indium for use in thin film plasmonic sensing, thereby expanding the range of available materials to researchers in the field. Chapter 3 focuses on the methodological considerations for achieving optimal characterization of the binding kinetics of therapeutics based on their valency, providing an experimental and analytical framework for SPR analysis of drugs with non-standard binding behaviors. In Chapters 4 and 5, new SPR biointerfaces are designed to quantify and correlate the effects of membrane composition on lateral diffusion and transmembrane protein function. All of these developments contribute to the overall aim of this dissertation, which is to provide tools that inform our understanding of biological systems and enable both identification and treatment of human disease.

TABLE OF CONTENTS

List of Figures

Figure 1.10. An overview of the structural diversity of gangliosides. Gangliosides are composed of an oligosaccharide headgroup containing at least one sialic acid attached to a ceramide tail. Headgroup structure determines ganglioside nomenclature. Sialic acid structure also varies depending on the source.

Figure 1.11. Overview of the three most common methods for bilayer formation on sensing surfaces. A) Supported lipid bilayers can be spontaneously formed on hydrophilic surfaces such as silica through incubation of vesicle suspensions. B) Tethered lipid bilayers can be formed on pre-functionalized surfaces (usually through gold-thiol bonds), creating a sub-membrane hydration layer that accommodates transmembrane proteins and diffusion across the membrane. C) Incorporation of large polymers such as polyethylene glycol (PEG) can allow for single-step bilayer formation on hydrophobic substrates and provides a hydration layer similar to tethered bilayers.

Figure 1.12. Schematic illustration of fluorescence recovery after photobleaching on a supported lipid bilayer containing fluorophore labeled lipids. Top-down views of the surface and corresponding intensities within the bleach area are plotted against time. The time points correspond to pre-bleach (1), immediate post-bleach (2), half-time recovery (3), and final recovery (4).

Figure 2.1. Schematic illustration of fabrication of plasmonically active indium thin films using e-beam physical vapor deposition (left). After deposition, a passivating oxide layer quickly forms upon exposure to air (middle). A conductive chromium adhesion layer between the glass and indium layers rescues propagating surface plasmon resonance response from interruptions caused by gaps between indium grains (right).

Figure 2.2. Calculated reflectivity curves of 20 nm and 40 nm indium films after oxidation. The 20 nm film was determined to be optimal for SPR and SPRi applications. The 40 nm film still promises a usable plasmonic response while achieving better surface coverage.

Figure 2.3. SEM images at 30 kx magnification (scale bars = 2 μm) of a 40 nm In film on glass (A) and 2 nm of chromium (B). C) Histogram showing the particle size distributions of the two films. D) Comparison of a 2/40 nm Cr/In film reflectivity spectrum with that of a typical gold SPR film. Curves were acquired on the same SPRi instrument with water (n = 1.33) in the flow cell.

Figure 2.4. Surface XPS analysis comparison of the two films showing a reduction in gaps and complete coverage of non-conductive Si (A and B). The bottom curves show In 3d orbital XPS depth profiles of C) 20 nm In film on glass and D) 2/40 nm Cr/In film.

Figure 2.5. Compositional analysis of A) 20 nm In film and B) 2/40 nm Cr/In films during XPS depth profiling.

Figure 2.6. A) Refractive index response of 2/40 nm Cr/In film using sucrose solutions (0.5-10.0% w/v). B) Refractive index response of 2/50 nm Cr/Au film using sucrose solutions (0.5-10.0% w/v). C) Comparison of the angle shift response to refractive index

change for 2/40 nm Cr/In and 2/50 nm Au. D) Comparison of sensitivity between the two films represented as °/RIU.

Figure 2.7. A) GIXRD scans of ~26 nm In_2O_3 films sputtered on silicon wafers and glass slides compared to the bare substrates. B) GIXRD scan of 40 nm In film deposited on a glass slide. All ordered crystalline peaks correspond to metallic indium, but a broad amorphous peak corresponding to those observed on the sputtered films is also observed (top right).

Figure 2.8. A) Refractive index vs. wavelength for sputtered In_2O_3 films at varying thicknesses and SE-calculated thicknesses. The data was collected by spectroscopic ellipsometry with a transparent film model ($k = 0$). B) Refractive index at $\lambda = 382$ nm vs. film thickness plot showing the transition from bulk to thin film properties around 40 nm. C) Real (n) and imaginary (k) refractive index vs. wavelength for the ~150 nm In_2O_3 film collected by ellipsometry with an absorbing film model.

Figure 2.9. Comparison of SPR reflectivity curve models utilizing best available refractive index values from literature[44] at 650 nm (n = ~2.10, k = ~0.009) and values we acquired experimentally (n = 1.964, k = 0.0024). The model uses an optimized metallic indium thickness at 16 nm, with varying oxide thicknesses to illustrate the increasing importance of accurate optical constants as film thickness increases.

Figure 2.10. A) 2D AFM and B) 3D image of a 3x3 μm section of a 40 nm indium film on glass with a resolution of 1024x1024 pixels. A 1x1 μm section of this image was used for FDTD simulations.

Figure 2.11. A) Top-down image of 40 nm In/In_2O_3 films obtained by AFM (scale bar = 200 nm) that was converted to an STL. B) Film model imported to FDTD software and placed on a 1x1x1 μm glass cube. C) Example of a frequency-domain field profile of a Z-plane on the oxidized film under 382 nm excitation. D) Maximum E_{loc}/E_{inc} for oxidized and unoxidized films under 382 nm and 532 nm excitement and the corresponding EF determined by the EF ≈ $|E|^4$ law. The oxide positively effects the enhancement under near-UV excitation, but not at 532 nm.

Figure 2.12. Heatmaps of the z-planes where the highest observed $\frac{E_{local}}{E_{incident}}$ was found for each simulated film. A) 382 nm excitation with oxide. B) 382 nm excitation without oxide. C) 532 nm excitation with oxide. D) 532 nm excitation without oxide.

Figure 3.1. Demonstration of NTA capture and regeneration consistency for the ligand used in this work. A) Left axis shows ligand capture is extremely consistent across the all cycles of the experiment. Right axis shows the raw SPR response before ligand capture across each cycle, with no drift up indicating complete regeneration. B) Overlayed sensorgrams showing cycle to cycle consistency for ligand capture and rinse, indicating highly accurate blank subtraction.

Figure 3.2. Kinetic SPR plots for the MA1 (A), MA2 (B), and MA3 (C) acquired under the same conditions on sensor chip NTA. Strong overlap between the experimental data and the kinetic fits can be observed along with distinct kinetic profile differences between the novel analytes in this work (MA1 & MA2) and the literature analyte (MA3).

Figure 3.3. A) Double reference subtracted sensorgrams for BA1 on sensor chip NTA. B) Sensorgram without blank subtraction, showing clearly that injections of the bivalent analyte reduce ligand rinse off compared to a buffer blank, explaining the lack of dissociation observed after blank subtraction.

Figure 3.4. Potential mechanisms for reduced ligand dissociation from sensor chip NTA when using bivalent analytes. A) Illustrates a doubly-bound analyte decreasing the likelihood of ligand dissociation by keeping it in proximity to the surface. B) Free-floating dissociated ligand may be recaptured by free warheads on the singly-bound bivalent analytes.

Figure 3.5. A) Labelled full sensorgram of the process for covalent capture on sensor chip NTA. The use of an NTA chip allows for preconcentration of ligand near the surface without needing to induce negative charge through the use of low pH buffers. B) Initial testing of BA1 on the covalently linked NTA surface showed artifacts such as negative shifts at low concentrations and upward drift during dissociation, making kinetic insights unreliable.

Figure 3.6. Results of initial testing of CA1 on sensor chip NTA. At 25 ºC (A), clear covalent binding shifts are apparent, particularly at higher concentration. At 37 ºC (B), the experiment completely fails due to accelerated ligand rinse off.

Figure 3.7. A) Ligand capture shift plotted vs the dilution factor of the cap-tagged ligand stock. Single cycle kinetic sensorgrams of BA1 (B) and BA2 (C) at concentrations of 0.2 - 125 nM in 5-fold dilutions.

Figure 3.8. A) 800 second injections of BA1 at different concentrations demonstrating how it may be impossible to reach steady state below R_{max} for analytes with very slow dissociation. B) Single cycle kinetic sensorgram of BA1 from 0.33 – 81 nM in 3-fold dilution steps. Three distinct R_{max} values can be observed as higher concentrations favor the bivalent analyte being singly bound to the ligands.

Figure 3.9. Single cycle kinetic sensorgrams of BA1 (A), BA2 (B), and MA1 (C) with concentration ranges of 8 pM to 25 nM in 5-fold dilution steps. Fitted line (black) was generated using a bivalent binding model for BA1 and BA2, and a 1:1 fitting model for MA1.

Figure 3.10. Single cycle kinetic sensorgrams of CA1 at 25 ºC (A) and 37 ºC (B) with concentrations between 15.625-1000 nM in 2-fold dilutions, showing clear covalent binding. Higher temperatures seem to drive higher rates of covalent binding despite less affinity for the initial reversible interaction.

Figure 4.1. Illustration of the structural modifications incorporated into the diverse ganglioside library utilized in this study. Key variations include glycan headgroup composition, sialic acid structure, ceramide chain length, and the position of fluorescent tags. These synthetic gangliosides are incorporated into biomimetic lipid bilayers for the investigation of their effects on the diffusion properties of membrane lipids and the binding affinity of membrane-associated proteins.

Figure 4.2. Synthesis of (A) *N*-hydroxysuccinimidyl 18-[(9-fluorenylmethoxycarbonyl)amino]octadecanoate, (B) 2-azido-octadecanoic acid, and their use in the preparation of ganglioside derivatives (C) 18-NBD-GM3 (d18:1; 18:0) and 18-NBD-GM1 (d18:1; 18:0), as well as (D) 2-NBD-GM3 (d18:1; 18:0) and 2-NBD-GM1 (d18:1; 18:0).

Figure 4.3. FRAP recovery curves (left) and fluorescence images (right) of POPC:CH:SP:DGS-NTA membranes containing 1% A) NBD-PE, B) 2-NBD-GM3, and C) 18-NBD-GM3.

Figure 4.4. Comparison of diffusion coefficients of NBD-PE, 2-NBD-gangliosides, and 18-NBD-gangliosides on 58:30:10:1:1 POPC:CH:SP:DGS-NTA:NBD SLBs before and after incubation with EGFR-ECD.

Figure 4.5. Tail group effects on NBD-PE lateral diffusion in POPC:CH:SP SLBs. A) Synthetic GM3s with fatty acyl chain lengths between 14 and 22 carbons show an inverse relationship between length and diffusion. The 22:0 GM3 containing membrane has similar diffusion to a membrane containing bovine milk derived GM3. B) Increasing the length of the sphingosine from 18 to 20 carbons results in a substantial reduction in membrane diffusion.

Figure 4.6. High-resolution mass spectrum (HRMS) of bovine milk ganglioside GM3 purchased from Avanti Polar Lipids (Cat. # 860058). The labelled peaks correspond to GM3 (d18:1) with varying fatty acyl chain lengths.

Figure 4.7. Membrane effects of GM3 sialic acid modifications. A) Differences in diffusion of NBD-PE in 58:30:10:1:1 POPC:CH:SP:NBD-PE:GM3 SLBs containing 1% GM3 (d18:1; 18:0) with different sialic acids. B) Comparison of the zeta potentials of 95:5 POPC:GM3 vesicles and plain zwitterionic POPC vesicles.

Figure 4.8. Diffusion coefficients of NBD-PE in 59:30:10:1 POPC:CH:SP:GM3 membranes containing 1% Neu5Ac, Neu5Gc, and fluorinated GM3 plotted versus the zeta potentials of vesicles composed of 95:5 POPC:respective GM3. Larger zeta potentials appear to be correlated with lower membrane diffusion, but the trend is not perfectly linear, indicating other factors other than charge may be affecting ganglioside cluster formation.

Figure 5.5. Overlayed brightfield and fluorescence images of A431 cells treated with annexin V. A) No annexin V control. Cells after 2 hours (B), 4 hours (C), and 6 hours (D) of serum starvation. E.) Healthy cells. Cells after 2 hours (F), 4 hours (G), and 6 hours (H) of chemical treatment.

Figure 5.6. Brightfield images of A431 cells at different stages in the osmotic shock process. A) Pre-treatment. B) Hypotonic PBS. C) Vesiculation buffer. D) Vesiculation buffer after shaking.

Figure 5.7. Nanoparticle tracking analysis results comparing the size of A431 blebs generated through A) serum starvation, B) chemical treatment, C) and osmotic shock. Note the osmotic shock blebs were extruded through a 200 nm filter prior to analysis, and table shows the dilution-adjusted particle concentrations.

Figure 5.8. A) Sensorgram showing the capture of A431 osmotic shock blebs on a Biacore L1 chip, followed by passivation with BSA that showed very little binding. B) Unstable capture of the blebs leads to consistent rinse-off during injections, potentially obscuring detection of anti-EGFR binding.

List of Tables

Chapter 1: Introduction and Background

1.1 Introduction

Over the past century, there have been tremendous improvements in the identification, understanding, and treatment of all manner of human diseases. Crucial and perhaps underappreciated in all of these areas are the numerous concurrent advancements that have been achieved in biosensing technology. This chapter provides background on biosensing as a whole, along with the foundational knowledge needed to understand the subdomains and biological systems relevant to subsequent chapters. Here we will cover a range of techniques relevant to the biosensing workflow, including those involved in the fabrication, characterization, and deployment of new biosensing platforms, with particular emphasis placed on surface plasmon resonance (SPR). Finally, background will be provided on the development of biomimetic lipid bilayer biointerfaces along with some systems in which their deployment helps to elucidate fundamental biophysical interactions.

1.2 Biosensing Overview

At their most fundamental level, a biosensor is a device that utilizes a biological recognition element along with a transducing unit to convert a biorecognition event into a measurable signal (Figure 1.1). Given this relatively broad definition, there exist an incredible diversity of biosensing devices in terms of not just the utilized biorecognition and transduction elements, but also the formfactor, accessibility, and the clinical, environmental, and industrial contexts in which they're deployed. The main broad areas of biosensor deployment include medical diagnostics,[1] drug development,[2] and

environmental monitoring.[3] Each specific application within these areas requires careful design and optimization of the biosensing platform to achieve the required sensitivity and limit of detection without compromising on needed practical elements such as portability, cost, and needed user expertise. Meeting these requirements demands careful selection of the sensing and detection modalities, as well as the biorecognition element.

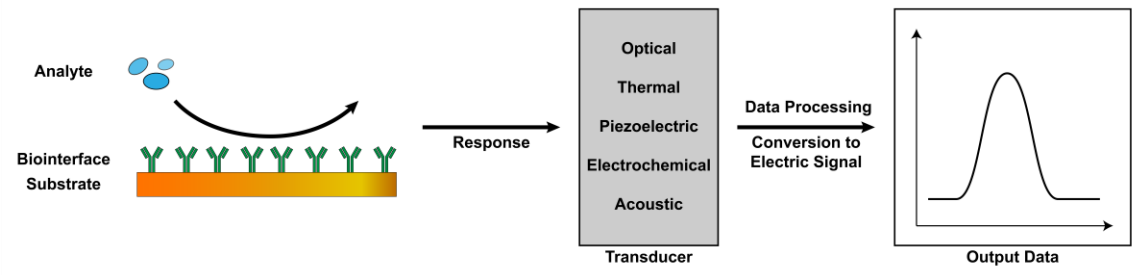

Figure 1.1. General scheme depicting the core components of a biosensor. Recognition events occurring between the biointerface and analyte result in a response in the transducing element that is converted to an electrical signal. This signal is then captured and processed by a computer and converted to readable data.

The three major classes of biosensor transduction/detection elements are optical, electrochemical, and mass-based, with multiple subdivisions within each. Mass-based sensors rely on changes in mechanical or oscillatory behavior after binding events, and include those based on piezoelectric effects such as quartz crystal microbalance (QCM) and surface acoustic wave (SAW), as well as cantilever-based sensors with sensing resulting from beam deflection caused by mechanical stress changes after binding events.[4] The primary advantages of these mass-based detection methods are their universal applicability. Detection is not dependent on, or affected by, the chemical or optical nature of the analyte, thereby allowing for consistent real-time detection across a range of analyte classes without the need for labelling, specific electrochemical properties, or complex

optical setups. Mass-based sensors have been deployed for numerous applications including detection of exosomes,[5] microbial monitoring,[6] and enzymatic processes[7] to name a few.

Electrochemical biosensors are extremely popular and have long been utilized, with many compelling advantages. First, they generally offer higher sensitivity than mass-based sensors and can often match or exceed the sensitivity of optical sensors depending on the sensing scheme and analyte.[8] Furthermore, with recent developments in nanofabrication techniques, they can be easily scaled down to allow for multiplexing and high portability without sacrificing sensitivity.[9] Direct electrical readouts also contribute to their compactness by avoiding the need for multiple lasers, alignment, and detectors to convert incoming light to an electrical signal. Finally, electrochemical sensors are far less sensitive to interference from non-specific binding and light absorption, making them often superior to optical sensors, but almost universally superior to mass-based sensors for biosensing in complex matrices.[10] For these reasons, electrochemical sensors are the most commonly utilized biosensor subdivision for point-of-care and commercial diagnostics. The most well-known example of their deployment is in glucose sensors for diabetics, but they've also seen extensive use in the monitoring of various other disease-related metabolites in humans as well as the study of various bacterial toxins.[11]

Optical biosensing, which is the primary modality discussed in this work, is the most diverse and widely utilized biosensing methodology in modern research, particularly in the fields of cell and molecular biology.[12] This subdivision can be further broken into the categories of labelled and label-free biosensing. Of the two methods, labelled

techniques are utilized far more commonly in both research and commercial settings owing primarily to their high sensitivity and specificity, ability to be multiplexed, and the diversity of methods for signal generation and detection.[13] Labelled biosensing techniques can generate signals through fluorescence, luminescence, or absorbance changes as binding events occur.

Absorbance, also often referred to as colorimetric, biosensors are valued for their simplicity and ability to be integrated into commercially available devices in which analyte binding events can be observed with the naked eye. The most common examples of these types of sensors are pregnancy and COVID lateral flow assays in which antibodies conjugated to a colorimetric reporter are captured on the test line in the presence of an antigen. While inexpensive and rapid, they have many notable downsides in terms of the sensitivity (false negatives), reusability, quantification (only provide yes or no binding), and specificity (false positives).[14,15] Luminescence-based assays offer substantially improved sensitivity, quantification, and specificity, but the more complex reagent requirements generally limit their usage primarily to professional settings.[16] The well-established and robust horseradish peroxidase (HRP) detection methods are utilized extensively in the detection of clinical biomarkers as well as environmental and food contaminants, primarily through antibody sandwich assays. Despite these many positive qualities, luminescence assays are fundamentally limited by the transient nature of their enzyme-based signal generation, with depletion of the substrate often precluding use in longer experiments.

Fluorescence-based biosensing combines many of the advantages of luminescence, with improved compatibility with experiments requiring multiplexing and long observation times.[17] The rapidly expanding library of fluorescent molecules offers researchers numerous options in terms of excitation and emission wavelengths, brightness, photostability, and biocompatibility, enabling highly tailored sensing strategies for a wide range of analytes and biological environments.[18] Though many fluorescence techniques carry complex and expensive instrumental requirements, their distinct advantages often justify their use in research and clinical contexts where the infrastructure is available. The uses of fluorescence biosensing are extensive with some examples including clinical diagnostics,[19] drug discovery,[20] cell imaging,[21] and environmental monitoring.[22]

However, all fluorescence-based methods carry one fundamental quality that may or may not have an effect on experimental results – the fluorescent label. While incredibly difficult to identify, the size, structure, and location of the fluorescent tag on an analyte or biorecognition molecule can perturb the conformation, binding affinity, and/or biological activity of the labelled molecule.[23,24] This effect is particularly important to consider when measuring the binding affinity of small molecule drugs where the fluorescent tag may be comparable in size to the drug it is attached to. Furthermore, the use of fluorescent tags can introduce other complications to the measurement of biorecognition events through increased assay complexity and cost introduced by the labelling process. Additionally, temporal changes in fluorescent intensity via photobleaching can lead to substantial run-to-ruin variability. These limitations create a need for techniques that provide many of the benefits of optical biosensing without the need for labels.

Many label-free optical biosensing techniques are utilized extensively across industrial (particularly pharmaceutical) and academic research to fill roles where the aforementioned limitations of labelled techniques may make them unsuitable.[25] Label-free optical biosensors generally achieve sensing through two phenomena – refractive index change and interference change. Interferometric biosensors measure the constructive and/or destructive interference patterns that arise on functionalized surfaces after binding events, compared to a reference. Some examples of techniques utilizing this effect include Mach-Zehnder, Fabry-Pérot, and biolayer interferometry (BLI), with BLI being routinely utilized in drug discovery pipelines.[26] As an alternative to interferometric sensing, many techniques have emerged to elucidate binding events on a substrate based on the accompanying refractive index change. Some examples include SPR spectroscopy, localized SPR (LSPR), waveguide, and ring resonator sensors, which all operate on the principle of total internal reflection (TIR) and the resulting evanescent field generation – an optical phenomenon that will be reviewed in more detail in the next section. These techniques are able to achieve exceptional sensitivity, with SPR specifically seeing widespread adoption into drug discovery processes due in part to its reproducibility and reliability.[26,27]

1.3 Surface Plasmon Resonance Fundamentals

Put very generally, surface plasmon resonance sensing operates at the nanoscale, where it is achieved by measuring the change in matching conditions of light with the substrate as binding events occur. At both the fundamental and practical level, however, there exists considerable diversity in how the SPR effect is physically realized and translated into a biosensing measurement. Thus, the SPR biosensing developments reported in this thesis must first be understood in the context of a solid theoretical framework, which is therefore established here before proceeding.

1.3.1 Evanescent Field Theory

The fundamental optical phenomenon that underpins the usage of SPR as a sensing methodology is the total internal reflection of incident light and the accompanying generation of an evanescent field that extends into the sensing medium. Though it is important to note that while TIR is not a necessary condition for achieving evanescent field excitation, having a clear angle of minimal light reflection is crucial for the most common SPR spectroscopy and imaging setups.[28] In TIR configurations, incident light is passed through one medium into another medium with a different refractive index, with these refractive indices commonly denoted as n_1 and n_2.

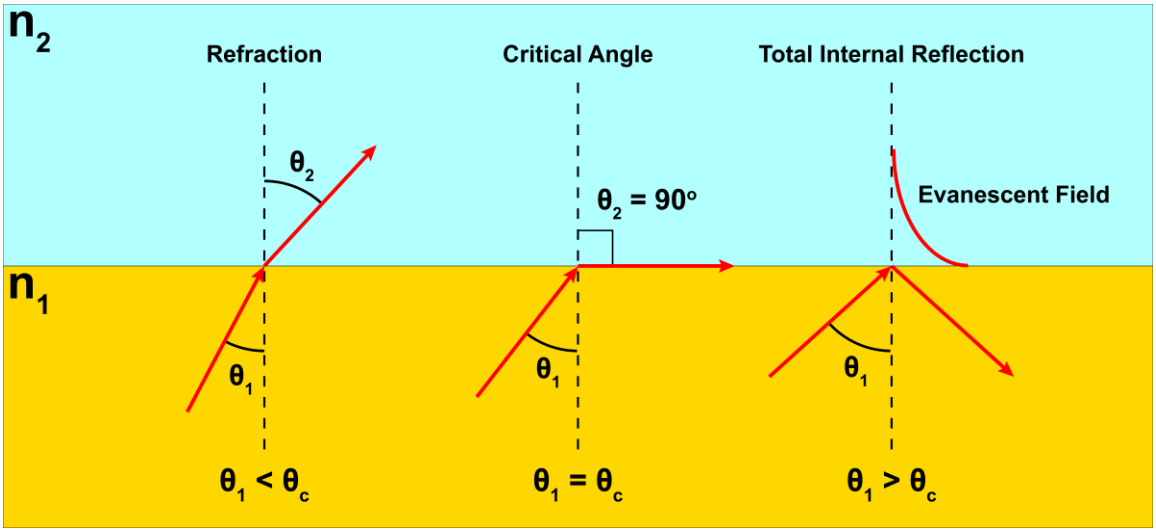

Figure 1.2. Depiction of how incident angle affects the behavior or light when passing between two materials with different refractive indices. Past the critical angle light undergoes total internal reflection, generating a decaying evanescent field at the interface.

The behavior of the light upon reaching the interface between the two media is highly dependent on its incident angle (Figure 1.2). Snell's law defines the critical angle (θ_c) as the minimum angle at which light no longer enters the second medium, instead being refracted perpendicular to the interface. The critical angle can be derived mathematically from Snell's law using the following equation:

$$\theta_c = \sin^{-1}\left(\frac{n_2}{n_1}\right) \tag{1.1}$$

Beyond the critical angle, light is considered to be entirely reflected back into the first material with no refraction into the second medium or perpendicular propagation. However, while the reflection is complete it does not mean that nothing is occurring past the interface, with the oscillating electrical and magnetic fields of the incoming light still extending a short distance into the second material. This phenomenon is known as an evanescent field, with its strength decaying exponentially as the distance from the interface

increases. The wave vector of the field (k_{ev}) in nondispersive media can be determined by the following equation:

$$k_{ev} = \frac{\omega}{c} n \sin\theta \tag{1.2}$$

The terms ω and c denote the angular frequency and speed of light (in a vacuum) respectively. The refractive index of the medium that the light is traveling through (n_1 in equation 1.1) is denoted simply as n. This equation can be modified for easier use with the following relationship:

$$2\pi c = \lambda\omega \tag{1.3}$$

Integrating this relationship into equation 1.2 provides the final wave vector equation in terms of the wavelength of incoming light (λ), which is a more relevant parameter in experimental and instrumental design:

$$k_{ev} = \frac{2\pi}{\lambda} n \sin\theta \tag{1.4}$$

Similar to the wave vector, the wavelength of incoming light also affects the distance into the second medium that the evanescent field can extend, commonly referred to as the penetration depth. The approximate value can be determined quite simply by dividing λ by two ($\lambda/2$), with depths between 100-300 nm common in typical SPR setups. However, it can be determined more accurately through more complex mathematical relationships.[29] This is relevant to sensing because it defines the maximum distance into the second medium where the refractive index (n_2) will affect the critical angle. To explain more clearly how the evanescent field is used in SPR biosensing applications, changes in

the local refractive index within the evanescent field (e.g. during binding events near the substrate) can be indirectly identified from changes in the detected reflectance profile of the incident beam.

1.3.2 Surface Plasmons and Polaritons

To utilize this sensing methodology effectively in practice, the change in the profile of reflected light must be highly distinct, behave consistently, and provide high sensitivity. Unfortunately, simple critical angle/reflectance tracking on a glass slide, for example, is not able to fulfill these requirements, with broad reflectance curves making minimum angle identification difficult, thereby increasing baseline noisiness.[29,30] Luckily, these limitations have long been resolved through the integration of metal films as the sensing substrate. Conduction band electrons in metals form a free electron gas at their surface that is subject to fluctuations from equilibrium, with the restoring forces from the positively charged metal ions causing coherent oscillations along the interface known as surface plasmons.[31] Important for biosensing, these surface plasmons are able to couple with incoming light, provided proper matching conditions are satisfied, leading to strong absorption of the light and a characteristic plasmonic dip.

The exact conditions by which coupling can be achieved are dependent on a multitude of factors. From a material perspective, the reflectance behavior of different metals can be predicted based on the real and imaginary components of their refractive indices[32] (n and k respectively) at single light wavelengths and polarizations using two Fresnel equations:

$$r_{\mathrm{p}} = \frac{n_2 \cos\theta_{\mathrm{i}} - n_1 \cos\theta_{\mathrm{t}}}{n_2 \cos\theta_{\mathrm{i}} + n_1 \cos\theta_{\mathrm{t}}} \tag{1.5}$$

$$r_{\mathrm{s}} = \frac{n_1 \cos\theta_i - n_2 \cos\theta_{\mathrm{t}}}{n_1 \cos\theta_i + n_2 \cos\theta_{\mathrm{t}}} \tag{1.6}$$

It is important to note that the values n_1 and n_2 shown here correspond to the complex refractive indices of the materials whereby n_1, for example, is equal to $n_1 + ik_1$. These equations also represent a simplified two-layer scheme that is not directly applicable to plasmonic systems because the absorption of incoming light is dependent on momentum coupling of the surface plasmons and the incident light.

Predicting plasmonic/reflective behavior of a film in these setups requires more complex mathematical modelling that integrates the Lorentz-Drude electron transport in materials model. The refractive indices of the material determine the reflectivity coefficient (R), with the relationship represented mathematically below:

$$R = \frac{(n-1)^2 + k^2}{(n+1)^2 + k^2} \tag{1.7}$$

Using this formula, software packages are able to generate reflectivity curves for defined metal thin films at specified wavelengths with high accuracy based on experimentally determined n & k values.[33,34] However, identification of why particular metals are plasmonically active and their optimal coupling wavelengths requires a deeper understanding of the properties of the material. Every metal has a unique frequency for the oscillations of its conduction band electrons known as the metal plasma frequency (ω_{p}), which is dependent on the free electron density (n_{e}), determined based on the following equation:

$$n_e = \frac{N_A Z p_m}{M} \tag{1.8}$$

Here N_A is equal to Avogadro's constant, Z is the number of free electrons, and p_m is the density of the metal. With this value determined, the plasma frequency can then be calculated using the following equation, where e and m are the charge and mass of an electron respectively, and ε_0 is the permittivity of free space.

$$\omega_p^2 = \frac{n_e e^2}{m\varepsilon_0} \tag{1.9}$$

With the plasma frequency now determined, understanding the plasmonic response requires understanding how, based on the ω_p, the metal responds to an applied electromagnetic field. The quantitative measure of this relationship is denoted by the dielectric constants, broken down into their real (ε_r) and imaginary (ε_i) parts, calculated with the metal's damping frequency (Γ) at a particular frequency of incident light (ω) as follows:

$$\varepsilon_r = 1 - \frac{\omega_p^2}{\omega^2 + \Gamma^2} \tag{1.10}$$

$$\varepsilon_i = 1 - \frac{\omega_p^2 \Gamma}{\omega(\omega^2 + \Gamma^2)} \tag{1.11}$$

These calculated dielectric constants can next be converted into the real and imaginary refractive indices for non-ferromagnetic metals using:

$$n = \sqrt{\frac{\sqrt{\varepsilon_r^2 + \varepsilon_i^2} + \varepsilon_r}{2}} \tag{1.12}$$

$$k = \sqrt{\frac{\sqrt{\varepsilon_r^2 + \varepsilon_i^2} - \varepsilon_r}{2}} \tag{1.13}$$

These refractive index values can be used in conjunction with equation 1.7, thus completing the process for generating reflectivity curves based on the fundamental electronic and physical properties of the metal. This provides a method for understanding or predicting plasmonic behavior in situations where experimentally obtained n and k values are unavailable or unreliable.

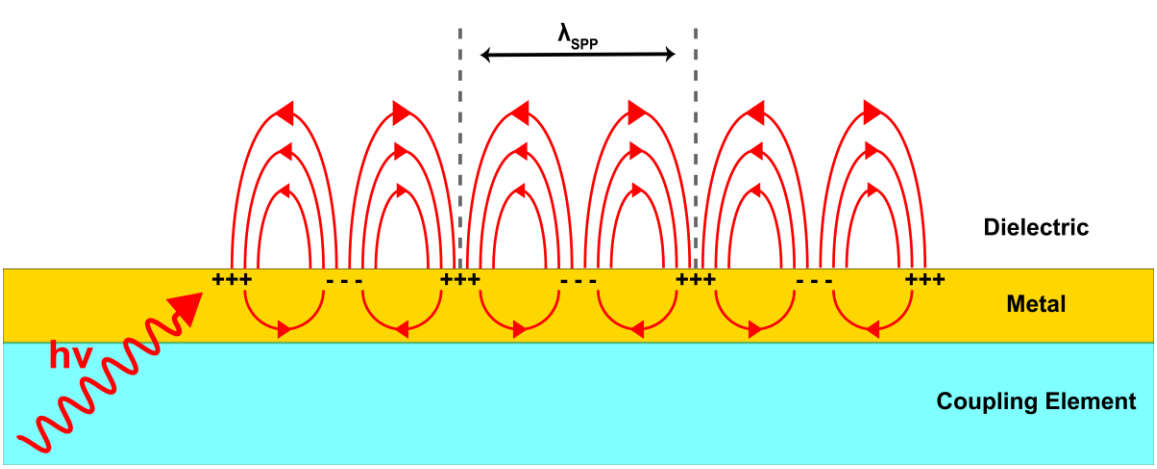

Figure 1.3. Illustration of the propagation of surface plasmon polaritons along a metal-dielectric interface after surface plasmons are coupled to incoming light.

These mathematical modelling techniques allow for the assessment of optimal film materials for plasmonic sensing without costly fabrication and experimentation, but this gives rise to the question of what photonic behavior makes for an optimal substrate for biosensing. As was alluded to earlier, the coupling of incident light and the surface plasmon wave is the critical process. These coupled photonic and electronic waves, referred to as surface plasmon polaritons (SPPs), are quasiparticles that propagate perpendicular to the metal surface at the interface with a dielectric material (Figure 1.3). The formation of SPPs

is accompanied by the generation of a strong evanescent field and can be visualized experimentally as a drop in reflectance resulting from light being tightly confined to the surface. Generally, an optimal surface should show a significant drop in reflectance at a narrow range of incident angles, with the shape and magnitude of this drop having large implications on sensing performance.[35]

1.3.3 Surface Plasmon Resonance Spectroscopy

With a solid understanding of what surface plasmons and evanescent fields are, and the photophysical or electromagnetic processes dictating their formation established, the obvious question that arises is how they're harnessed together to achieve sensing in SPR setups. Standard SPR configurations are composed of a plasmonic thin metal film, light source, detector, fluidic channels, and a coupling element. Beginning with the coupling element, if generation of SPPs is the goal, the frequency and momentum of incident light must match those of the surface plasmons. To achieve this experimentally requires the use of a coupling element such as a high refractive index prism or grating, with prisms being used most commonly.[36] Just as critical as the presence of the coupling element are the angle and wavelength of the incident light, with the optimal values determined by the metal film and its thickness, as well as the refractive index and geometry of the coupling element. Given the need to balance all these factors to obtain a strong response within an experimentally feasible angle and wavelength range, the value of computationally modelling the reflectivity curve becomes more apparent.

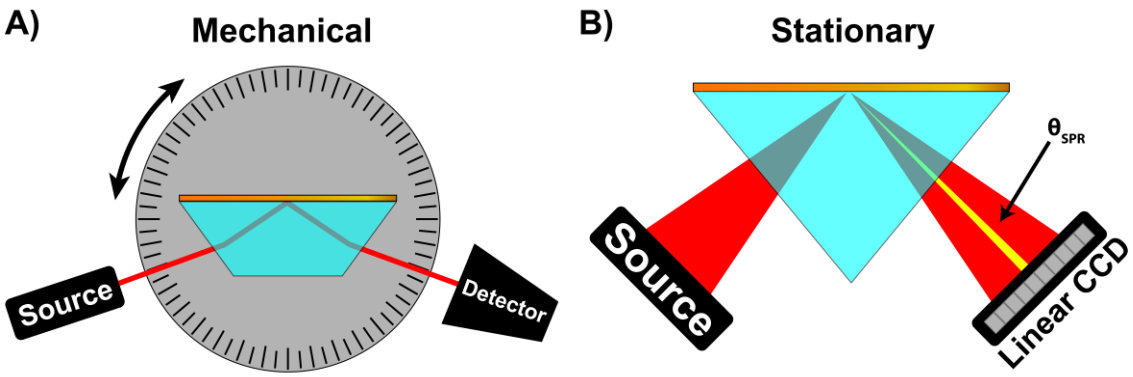

Figure 1.4. Illustration of the two most common setups for Kretschmann configuration SPR sensing. A) Mechanical setup in which the entire prism and sensing surface is rotated on a goniometer. B) Stationary setup where a linear CCD can sample all angles simultaneously, including the change in resonant angle shown in yellow.

For spectroscopic SPR, the Kretschmann configuration where the plasmonic metal film is in contact with the prism is often the first choice, though other options such as the Otto configuration were utilized historically.[37,38] In these configurations, light passes through the prism at an angle, comes into contact with the metal film, and is reflected back to the detector. In angular systems, a plot of angle vs. light intensity (reflectivity curve) to identify an angle of minimum reflectivity can be done by physically rotating the prism and attached film across a range of angles (Figure 1.4A). Alternatively, and more commonly in commercial systems, the entire system is held static by using a linear detector that can measure reflected light across multiple angles simultaneously (Figure 1.4B). This allows for significantly higher sampling rates and improves reliability by minimizing mechanical elements in the system, with the downside of limiting the accessible angle ranges. In these systems, real-time label-free sensing is achieved by simply monitoring the change in the angle of minimum reflectivity as binding events at the surface change the local refractive

index. Wavelength scanning is another method for spectroscopic SPR, commonly utilized in more portable fiber optic SPR systems, where a range of wavelengths isolated from a white light source are used to identify changes in resonant wavelength as the refractive index changes at the surface.[39]

Binding events are visualized and monitored in SPR spectroscopy as a plot of resonant angle or wavelength vs. time, also referred to as a sensorgram (Figure 1.5). In angle scanning SPR, binding near the surface will appear as a positive shift in the resonant angle, with the magnitude being correlated to the refractive index change. With the instrumentation and underlying mechanisms established, the main question remaining is how to functionalize the surface to allow for clear observation of the interaction of choice. Here lies the greatest challenge and diversity of options in generating data that most closely resembles the reality of the biological system being investigated. The main hurdle to overcome in SPR is how to tease out real binding from non-specific binding and bulk refractive index changes.

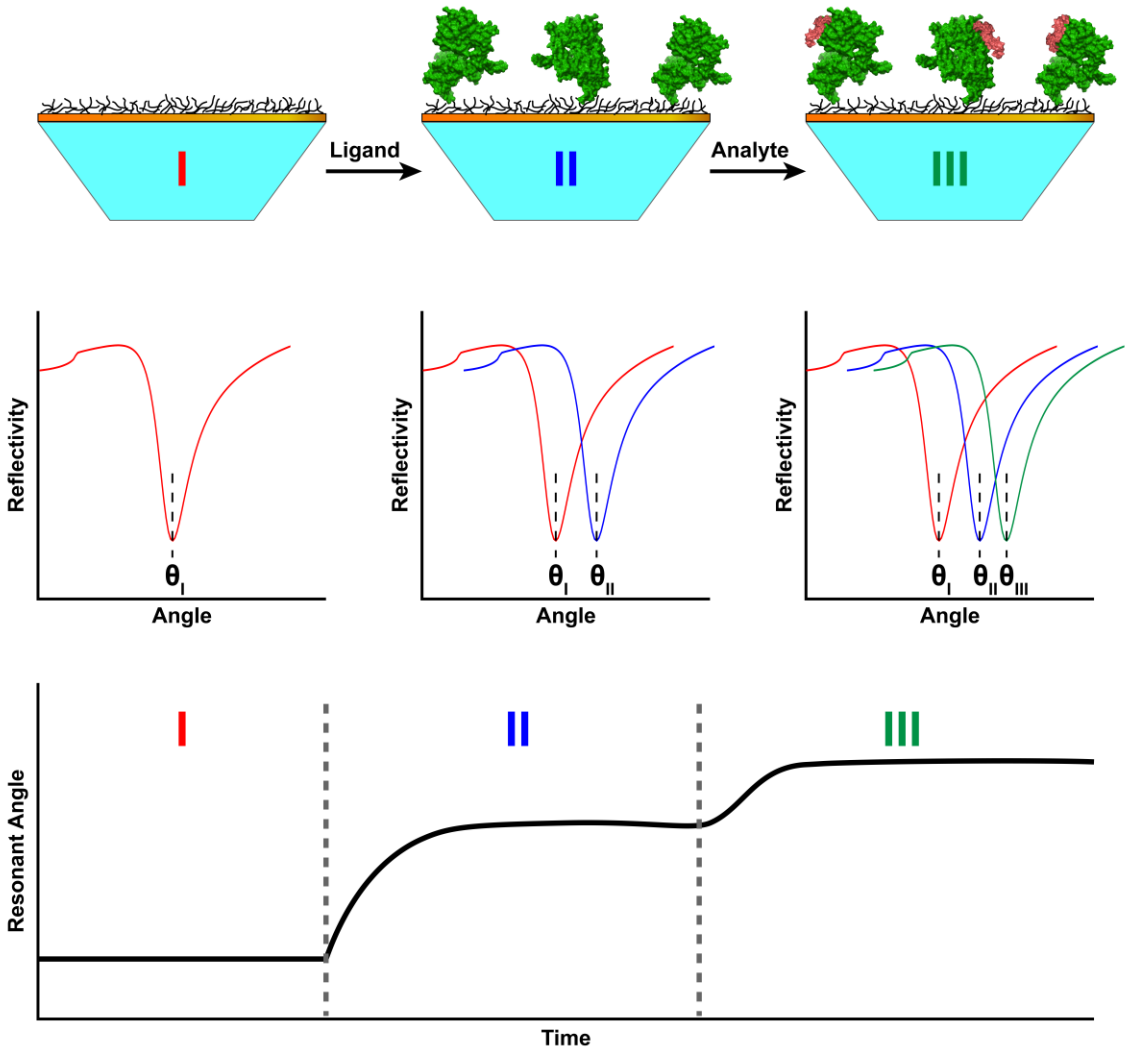

Figure 1.5. Illustration of how surface binding events are translated into real-time analysis during an SPR spectroscopy experiment. The angle of minimum reflectivity is extracted from reflectivity curves and plotted against time, with the change being roughly proportional to the refractive index change at the surface.

Reduction of non-specific binding requires many factors to be considered simultaneously to achieve a good result. First and foremost, the surface must be passivated through functionalization or blocking steps prior to analysis.[40] Most commercial SPR surfaces are functionalized with carboxymethylated dextran chains of varying lengths, forming dense hydrogels that prevent non-specific binding through both charge repulsion and steric blocking of access to the often-hydrophobic metal film below. However, while work has been done to make replicating these films accessible to individual researchers, many of their syntheses are complex and guarded industrial processes. This has led researchers to seek out simpler, more accessible, and less expensive alternatives. A few examples include covalently attached self-assembled monolayers,[41] zwitterionic polymer or lipid coatings,[42] and passivation with polyethylene glycol (PEG).[43,44] Beyond surface functionalization, non-specific binding during analysis is often reduced through surface blocking after ligand capture, with bovine serum albumin (BSA) being the most common option. Finally, optimizations to the running buffer can further reduce non-specific binding through either introduction of carrier proteins and/or surfactants, along with changes to pH or ionic strength.

Beyond experimental considerations, data processing and method development can aid in extracting the wanted binding signal from the raw sensorgrams (Figure 1.6A). Absolutely necessary to obtain high quality data is the use of a reference channel that is otherwise identical to the active channels beyond the absence of the capture molecule. This allows for subtraction of shifts resulting from non-specific binding and bulk refractive index differences between the running buffer and analyte solutions (Figure 1.6B). While

this massively improves data quality, perfect subtraction relies on both channels behaving identically during analyte injections. However, both channels having identical sensitivity to refractive index change is unlikely, particularly with high ligand immobilizations on the active channel actively dampening the sensitivity of that channel. Additionally, components in the analyte solution may interact differently on the active channel, or ligand may rinse off the active channel, leading to an altered response. To resolve these issues, more recent instrumentation, aided by highly consistent injection systems, are capable of performing blank cycles that can be subtracted from analysis cycles (Figure 1.6C). Combining these techniques generates double reference subtracted sensorgrams that allow for high-quality analysis, particularly in systems where the analyte solutions have compositions very different from the running buffer (e.g. small molecule analytes that require high concentrations of DMSO for solubility).

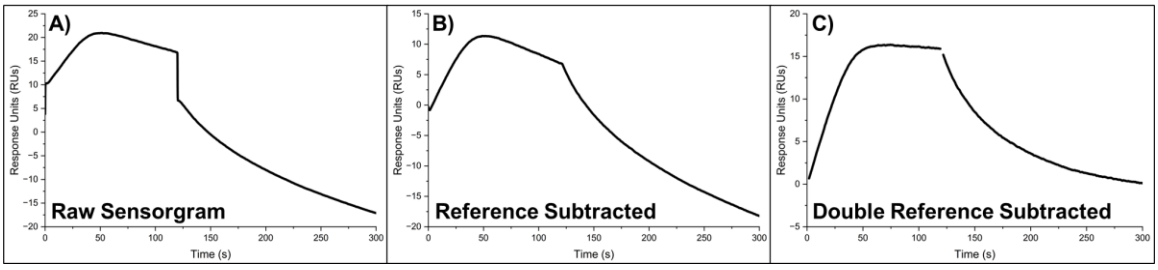

Figure 1.6. Demonstration of the importance of reference subtraction for acquiring high quality kinetic curves with SPR. Single reference subtraction (B) removes the influence of bulk refractive index change on the sensorgram. Double reference subtraction (C) corrects for ligand rinse off and differences in bulk refractive index response between channels.

The final step in SPR spectroscopy is analysis of the data, with both the shapes and magnitudes of the curves providing valuable insights. Endpoint data, or the total shift from baseline after long incubations or injections have been utilized in biophysical studies to understand how properties of the ligand affect analyte binding.[45,46] However, SPR's main

value over many other biosensing techniques is its ability to extract dissociation (k_d or k_{off}) and association (k_a or k_{on}) kinetic constants, along with the overall affinity of the interaction (K_D). The relationship between the kinetic constants and the affinity in 1:1 binding system is as follows:

$$K_D = \frac{k_d}{k_a} = \frac{k_{off}}{k_{on}} \tag{1.14}$$

While other techniques such as isothermal titration calorimetry (ITC), fluorescence polarization (FP), and enzyme-linked immunosorbent assays (ELISA) can provide ratios of the kinetic parameters (equilibrium affinity), the individual values can have significant implications on drug efficacy in living systems.[47,48] Residence time (which is dependent on the k_d) of a drug in its binding site is increasingly being recognized as the most relevant parameter in vivo, meaning two drugs with the same K_D may perform very differently depending on their kinetics.[49]

Furthermore, observation of the binding kinetics can open the door for improved mechanistic understandings of interactions. Kinetic values are extracted from sensorgrams through the use of sophisticated fitting algorithms built for specific binding models (e.g. 1:1 Langmuir binding model).[50] Significant deviations from the expected fits of a model can indicate different mechanisms, such as 2:1 (bivalent) interactions or more complex two-state reactions where one interaction is dependent on another.[51] Beyond just identifying these interactions, purpose built binding models can extract the secondary rate constants, further adding to the utility of SPR spectroscopy.

1.3.4 Nanostructures and Localized SPR

To this point we've only examined the role of SPR in the thin film or propagating regime, but numerous other morphologies are capable of plasmonic coupling to incident light, with some key differences. More specifically, metal nanostructures or nanoparticles have been utilized extensively for plasmonic applications, with the primary requirement being that the structure is much smaller than the wavelength of the incident light. When these structures are exposed to light, their conduction band electrons do not form a propagating wave. Instead, the electron cloud is pulled to one side of the structure before being subjected to the restoring force of the now positively charged metal ions, causing frequent oscillations and strong enhancement of the electric field at the surface (Figure 1.7).[52] Compared to propagating SPR, the confinement of this field is an order of magnitude smaller (10-30 nm vs 100-300 nm), giving rise to the name of localized surface plasmon resonance (LSPR). Similar to propagating SPR, LSPR is sensitive to refractive index changes at the surface, but the tight confinement limits sensitivity with certain analytes such as large proteins.[53] However, the confinement does aid in reducing sensitivity to bulk refractive index changes.[54] Additionally, LSPR carries the advantage of simpler instrumentation owing to there being no need to satisfy angle and momentum matching conditions.

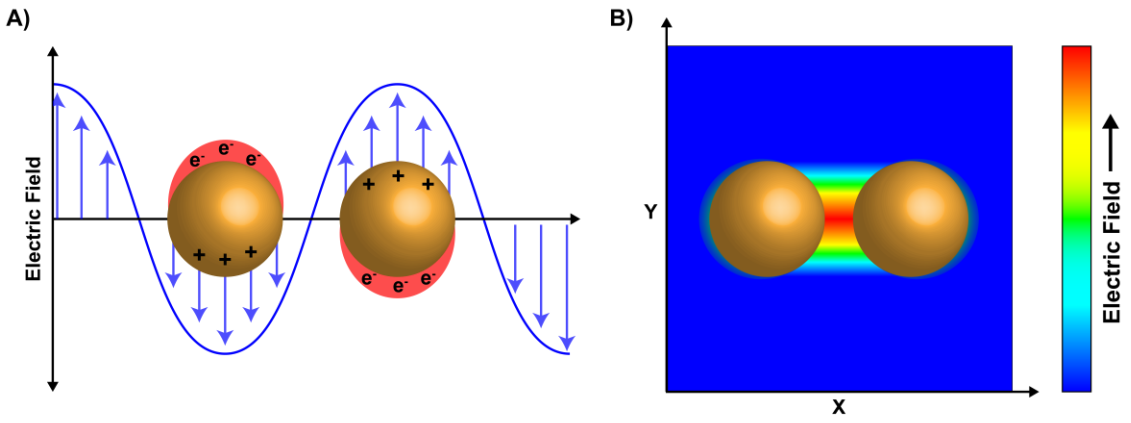

Figure 1.7. A) Localized surface plasmon resonance of gold nanoparticles. Incident light (blue) cause rapid oscillation of conduction band electrons, greatly increasing free electron density around the surface of the particles. B) Illustration of an FDTD simulation showing the strong field enhancement created in the gap between two nanoparticles – the basis of SERS.

The uses of LSPR are not limited to sensing analogous to propagating SPR, and the effect has been harnessed for many other purposes, both inside and outside of the realm of biosensing. Most frequently for sensing, the nanostructures are not used as the vehicle for signal generation, but rather as signal enhancement mechanisms. For example, nanoparticles conjugated to biomolecules (most commonly antibodies) can substantially increase signal in mass-based sensing techniques, with this effect further enhanced through plasmonic coupling if used with standard spectroscopic SPR.[55] The LSPR effect also forms the basis of surface enhanced Raman spectroscopy (SERS), where the structures' surfaces act as electromagnetic hotspots that improve Raman signal by as much as 11 orders of magnitude.[56] Beyond sensing, LSPR has been harnessed by humans since at least the 4th century, with the distinct absorption profiles of nanoparticles being used to stain glass. In modern industry and research, the effect is used extensively in catalysis, solar energy

conversion,[57] microscopy,[58] and cancer treatment[58] to name just a few major areas, though these applications are not relevant to this work.

1.4 Plasmonic Metals

With the broad range of applications for propagating and localized SPR, it stands to reason that there would also be a great diversity of plasmonic metals, but the field is actually quite limited due to both practical and theoretical limitations.[59] From the standpoint of the metal's optical qualities, certain dielectric functions lend themselves to high sensitivity (S) and the sharp resonances defined by the full width at half maximum (FWHM) of the plasmonic dip. The sensitivity is defined as the sine of the change in the angle of maximal surface plasmon resonance ($\sin\theta_{sp}$) proportional to the change in refractive index in the sensing area (n_s):

$$S = \frac{\Delta \sin\theta_{sp}}{n_s} \tag{1.15}$$

The quality of SPR substrates can be quantitatively compared using the figure of merit (FOM), which can be calculated in a few ways,[60] with the following method being the most common:

$$FOM = \frac{S}{FWHM} = \frac{\Delta \sin\theta_{sp}}{FWMH \Delta n_s} \tag{1.16}$$

The primary fundamental qualities of a metal that dictate its FOM for SPR sensing are the dielectric constants. As a general rule, large negative real and small imaginary dielectric constants lend to improved performance:

$$\text{FOM} \propto \frac{|\varepsilon_r|}{\varepsilon_i} \tag{1.17}$$

However, it's crucial to note that the performance of a particular metal substrate is heavily dependent on the wavelength of the incident light. For a metal to be practical to use, the resonance must be achievable in an experimentally feasible wavelength range, which generally restricts it to the visible and very near infrared (IR) ranges.[61]

At high frequencies, such as in the ultraviolet (UV) and deep ultraviolet, while some metals satisfy the plasmonic matching conditions well, multiple practical issues begin to arise. For example, optical components and detectors compatible with UV light are generally more specialized and expensive. Furthermore, high frequency light has the potential to damage biomolecules, optics, and detectors over long exposures. On the other side of the visible spectrum is IR light with its own challenges in acquiring proper optical materials and detectors. Additionally, and more importantly, absorptive losses to both the film and water in the sensing area becomes a growing issue as the wavelength increases. For these reasons, the typical wavelengths used in commercial instruments, and consequently, the compatible metals are quite limited.[62]

The group 11 "noble" metals of gold and silver are the favored materials for visible to near-IR plasmonic sensing (~400-850 nm), with silver performing optimally in the lower end of that range and gold performing better at the higher end.[63] Between the two, silver offers better sensitivity and a more narrow (smaller FWHM) plasmonic dip, owing to its higher plasma frequency and more favorable dielectric constants in the visible range. However, plasmonic response must not be the only consideration as, among these two,

gold is much more widely used, with the commercially standard SPR substrate being a gold film of approximately 40-50 nm.

This leads into the practical considerations when identifying what metal should be used for a specific application. From a commercial standpoint, where quality control and consistent performance are key, gold is unmatched due to its exceptional chemical stability. Unlike silver, gold does not oxidize and is much less likely to have its surface layers fouled by other trace gases in the air.[64] Because of this, surface modification to gold films, particularly if done shortly after fabrication, can be made highly consistent. Gold is most often functionalized through its very well characterized reactivity with thiol groups, with carboxymethyldextran hydrogels attached through this chemistry being the commercial standard. Silver, however, does enjoy some popularity in research contexts, where maximal sensitivity is the goal of the work, or necessary for the application. Additionally, much work has been done to harness the sensitivity of silver while improving the surface stability through surface coatings, alternating gold and silver layers, or alloying.[65–68]

1.4.1 Group 13 Plasmonic Metals

In recent years, there has been growing exploration of the use of alternative metals for SPR, thereby expanding the range of available applications. Particular interest has been drawn towards metals capable of coupling with UV excitation, where the high energy and absorption by biomolecules could serve to improve performance. Aluminum has arisen as a promising candidate, with nanostructure-based techniques such as SERS being popular choices due to simplified optical setups reducing the practical limitations of using UV light.

Aluminum, along with other metals in its periodic group, has three conduction band electrons compared to gold and silver, which have one. This difference leads to some distinct changes in the electronic and photonic behavior of the material with implications for plasmonic response and coupling conditions. The higher electron density results in a higher ω_p, with associated changes in the dielectric functions that facilitate better performance at shorter wavelengths. For example, at 380 nm, the $|\varepsilon_r|$ for aluminum is roughly an order of magnitude larger (Figure 1.8A), and the ε_i is approximately three times smaller (Figure 1.8B) than that of gold.[69] However, aluminum and other metals in its group (namely indium), are not limited to short wavelengths, and actually have useable plasmonic response across a much-expanded range when compared to gold and silver (Figure 1.9).[70] This leads to interesting potential applications in multiwavelength SPR methodologies.[71]

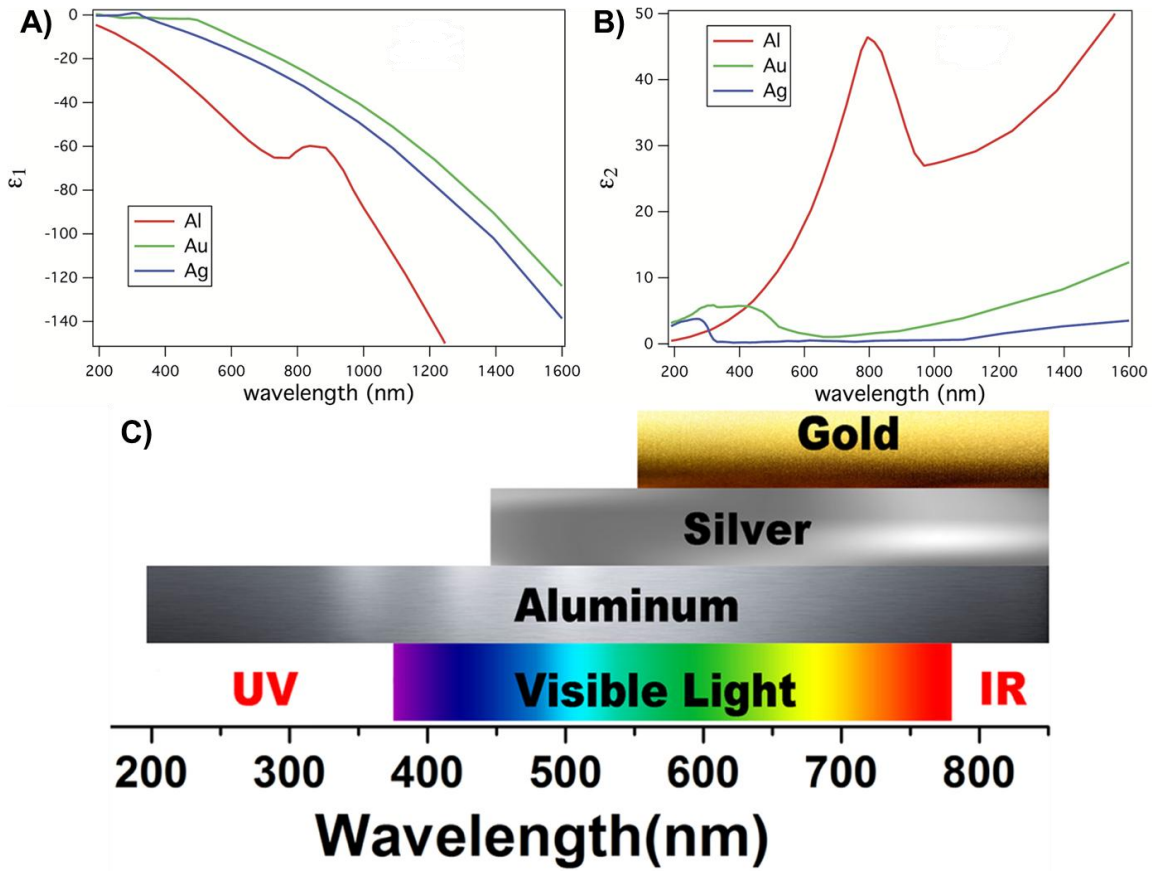

Figure 1.8. Plots comparing the real (A) and imaginary (B) components of the dielectric functions for gold, silver, and aluminum from 200-1600 nm. Reprinted with permission from reference 69. C) Plasmonic tuning ranges of gold, silver, and aluminum. Reprinted with permission from reference 70.

With the benefits established, these metals do carry certain downsides when compared to the noble metals. First and foremost, they lack the chemical stability of gold, with rapid formation of a thin oxide layer occurring shortly after exposure to air, which can broaden SPR dips, dampen sensitivity, and/or shift the resonant angle (Figure 1.9B).[72,73] Additionally, these oxide layers are generally less stable in both water and air, making them prone to corrosion in the long term.[74] However, some recent work has demonstrated that aluminum SPR chips are stable in buffer over a reasonable experimental time course.[75] Another downside to these metals is that they show quite broad resonance peaks,

particularly at longer wavelengths. Despite this, aluminum films at an optimal thickness have shown competitive performance with gold films in angle scanning SPR, and superior performance in SPR imaging with a 650 nm excitation source.[75] Regarding other group 13 metals, investigation of the performance as well as the optical and physical properties of indium forms the basis of the following chapter, while gallium and thallium are unsuitable for SPR primarily due to their melting points and toxicity respectively.

1.5 Optimizing Thin Films for SPR Sensing

To achieve good plasmonic response, with well-defined dips and high sensitivity for an SPR substrate, demands a few conditions are satisfied. For example, the thickness of films must be carefully optimized based on the specific metal being used and the excitation wavelength. When films are too thin, the ability of the evanescent field to couple properly is compromised, resulting in broad and shallow resonant peaks. When the films become too thick, the evanescent field generated at the interface between the prism and the film decays too much by the time it reaches the outer surface of the film, again leading to poor coupling (Figure 1.9).[76] While the most impactful, film thickness is not the only factor that can lead to reduced sensitivity and broadened resonances, with some examples including surface roughness, crystallinity, and grain boundaries.[77] Popular methods to characterize the morphology of thin films, as well as fabrication considerations for minimizing undesirable features will be presented in the following subsections, with particular focus on the methods utilized in future chapters.

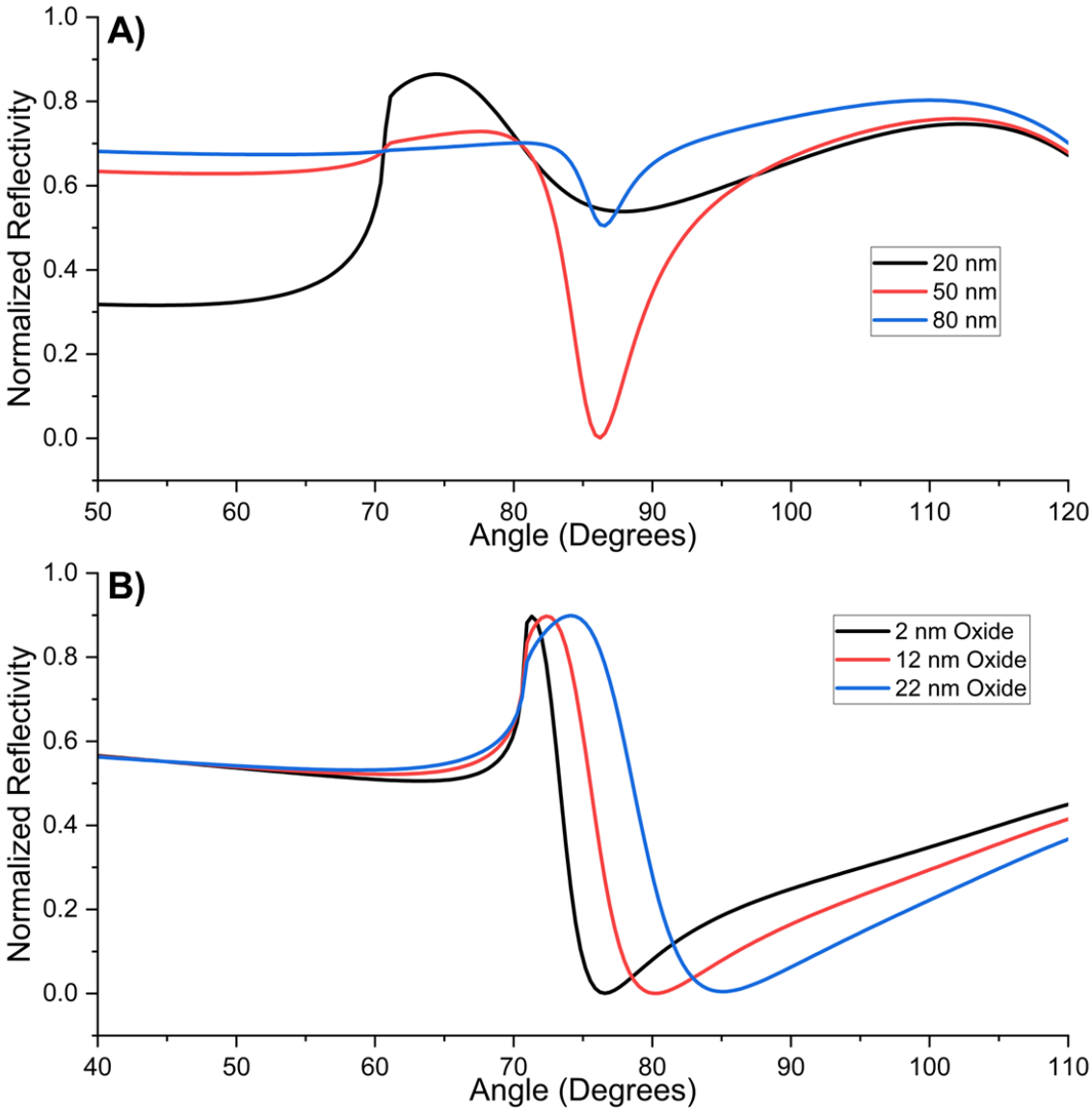

Figure 1.9. Demonstration of the effects of film thickness on simulated SPR reflectivity curves. A) SPR curves of gold films at different thicknesses in water (n = 1.33), coupled with a BK-7 prism (n = 1.51). When too thin (20 nm), the films demonstrate a very broad resonance, while it becomes shallow then too thick (80 nm). B) Demonstrates effects of the oxide layer (Al_2O_3) on a 12 nm aluminum film with increasing thicknesses shifting and broadening the reflectivity dip.

1.5.1 Importance and Characterization of Film Morphology

Because the previously outlined morphological factors have such tremendous implications on the SPR performance of a film, it becomes necessary to have an appropriate toolset to characterize every relevant parameter. For standard materials that form well understood and uniform films (such as gold), the film thickness can generally be accurately monitored in real time during deposition using piezoelectric mass measurements. Characterization beyond this requires additional techniques and processes, with each providing unique and oftentimes orthogonal information about film morphology. The degree of necessary characterization is dependent on material and application, with nonstandard, nanostructured, multilayered, and/or oxidizing films usually requiring additional steps for comprehensive understanding.

Beginning with the more macroscopic film characteristics such as film thickness, roughness, and surface feature sizing, microscopy techniques are extremely powerful and most broadly utilized. Scanning electron microscopy (SEM) is a rapid, non-destructive, and high-resolution method for generating 2D images of the film surface. By bombarding the film with a focused electron beam, surface features such as grain sizes, grain boundaries, and film continuity can be examined in great detail. Most modern instruments are also equipped for energy dispersive x-ray spectroscopy (EDX), which can be used to identify the chemical makeup of the imaged material. However, high penetration depths risk observation of the substrate below thin films, limiting its usefulness in these applications.[78]

For more quantitative assessments of film surfaces, atomic force microscopy (AFM) is nearly unmatched, providing 3D characterization of films with potential for sub-nanometer resolution. AFM is indispensable for development of SPR substrates, primarily due to its ability to provide quantitative assessment of film roughness, which is a highly relevant parameter for sensing performance.[79] Surface roughness is negatively correlated with performance for a few different reasons. SPR fundamentally relies on wave vector matching, and different thicknesses across a surface introduces spatial variations in optimal matching conditions, thereby causing more shallow and broad dips. Furthermore, high roughness can lead to spatial variations in surface area, potentially leading to inconsistent surface functionalization, binding response, and/or nonspecific binding, thereby increasing run-to-run variability.

AFM works by sweeping a small tip, generally composed of silicon or silicon nitride, on a flexible cantilever across the surface. A laser is focused on the cantilever, and as the tip interacts with the surface, corresponding bends to the cantilever cause the beam to slightly deflect. By tracking the change in the angle of the beam, heights of structures across the surface can be monitored. The tip interaction with the surface of metal films is generally conducted in two different modes: contact and tapping. Contact mode operates by simply dragging the tip across the surface, allowing for quick and accurate analysis of hard and flat surfaces. However, it is less ideal for softer and rough surfaces, where material can be scraped away or the tip can be quickly damaged. Tapping mode is more gentle, but slower, making it more appropriate for softer metals such as gold if throughput is not a concern.[80]

Gold and silver, with their long and widespread usage in the thin film regime, are well characterized. However, nonstandard materials are generally less well understood and require additional forms of characterization to properly optimize their performance. Crystallinity of SPR films is a generally overlooked parameter due to the high performance and strong preference of evaporated gold and silver films to form (111) planes.[77,81] The refractive index and resulting plasmonic behavior of a material are highly dependent on crystallinity, and nonstandard materials may need specific deposition or post-deposition treatments to achieve optimal sensing performance.[82] Characterization of crystallinity under different conditions and identification of corresponding refractive indices can inform simulations of reflectivity curves and sensitivity, forming a strong methodology for optimization.

X-ray diffraction (XRD) is the most common method for determining crystallinity of materials. However, in the standard Bragg-Brentano geometry, the penetration depth of the X-ray beam is in the low micron range, making it less than ideal for characterizing thin films.[83] In this geometry, measurement of the crystallinity of the substrate beneath the films can overwhelm any signal generated by the material of interest. Glancing incidence XRD (GIXRD), where the X-rays are focused on the surface at a very narrow angle, allows for much shallower penetration depths as low as the single nanometer scale, providing clearer analysis of surface layers.[84,85] There are a multitude of methods to alter and potentially improve crystallization of films for SPR. When fabricating the films, choice of deposition method (thermal evaporation, sputtering, etc.), substrate temperature, deposition rate, gas pressure, and the substrate can all have substantial effects.[86] Additionally, post-deposition

treatments such as thermal, electrical, or chemical treatments are used to alter the surfaces of thin films.[87,88] There is not one optimal method for SPR substrate fabrication, and each material will differ both in its response to treatment and its optimal crystallinity for a specific application.

Another important step for informing modelling and optimization of thin films for SPR is quantification of the thicknesses of individual material layers. In nonstandard metals, the specific chemical structure and thickness of oxide layers may not be known or reliably reported in literature. There are many methods for performing chemical analysis of a surface, with X-ray-based methods being a particularly powerful and widely available option. Amongst these methods, X-ray photoelectron spectroscopy (XPS) provides the best surface sensitivity and lowest penetration depths.[89] It works by bombarding the sample with X-rays, causing ejection of photoelectrons with binding energies characteristic of both the atoms themselves and their chemical state. Furthermore, this method can be coupled stepwise with etching processes to create depth profiles of films, allowing for rough quantification of layer thicknesses.[90]

The final crucial information that must be extracted to inform SPR optimization is the refractive indices of each layer of the material. Here again there are many techniques for determining these values, but ellipsometry is the most informative and commonly used. By measuring the change in the polarization of light as it travels through/reflects off a material, ellipsometry can quickly determine the refractive indices across a large spectral range.[91] This works best for systems where all layers excluding the one for measurement are well defined. The substrate the film is deposited on should also be highly reflective

across the measurement range, usually requiring that the films be deposited on a silicon wafer instead of glass, as is typical for SPR. For multilayered films (such as those that oxidize), where neither material is well characterized, it may be necessary to deposit and analyze each layer individually to obtain accurate measurements.[92]

1.6 Ganglioside-Protein Interactions

Gangliosides are a class of glycolipids in the membranes of cells that play numerous roles throughout much of the human body. They're composed of two primary components, with each carrying a great deal of structural diversity (Figure 1.10). The first is the ceramide group, composed of a sphingosine tail and a fatty acyl chain, that is inserted primarily into the outer leaflet of cell membranes. Here, each tail can vary substantially in length,[93–95] with certain profiles being disease associated.[96] The ceramide is attached to an oligosaccharide headgroup that extends into the extracellular space. What distinguishes gangliosides from the general class of glycosphingolipids is the presence of at least one sialic acid moiety on their headgroup. The number of sialic acids and other monosaccharides, as well as their linkages, determines their naming, with mono-, di-, and tri- sialic acid gangliosides denoted as GM, GD, and GT respectively. Human cells contain primarily the neu5Ac form of sialic acid, but other forms such as neu5Gc can be integrated from dietary sources, with higher incidence noted in certain forms of cancer.[97]

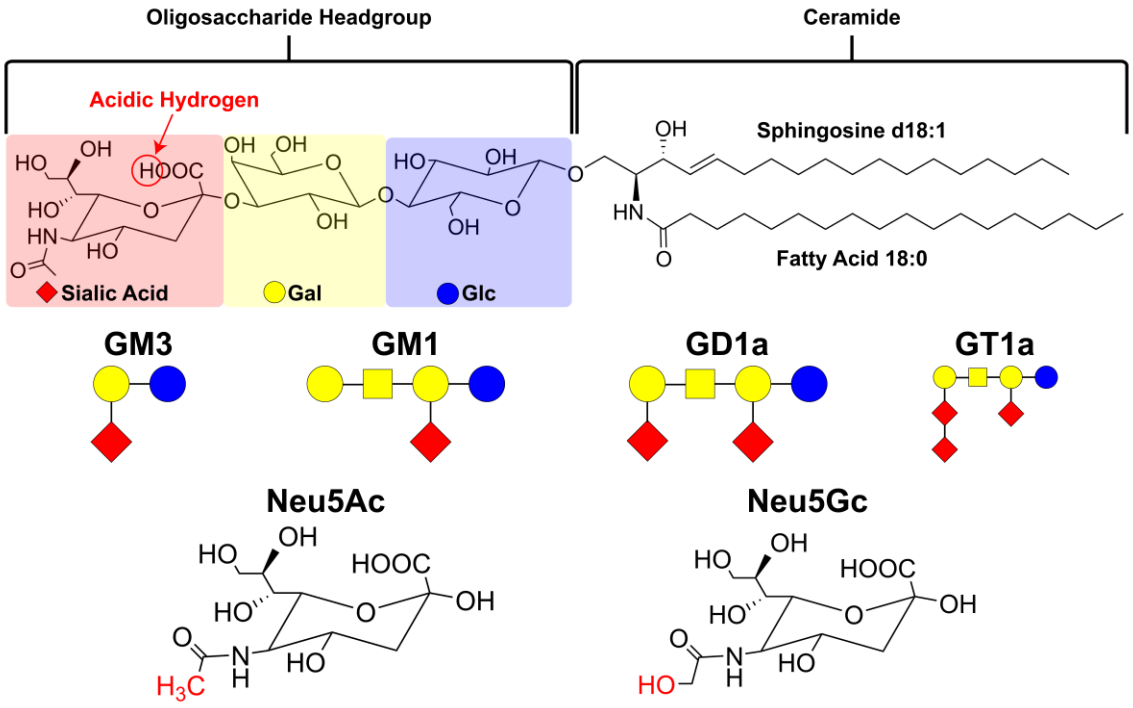

Figure 1.10. An overview of the structural diversity of gangliosides. Gangliosides are composed of an oligosaccharide headgroup containing at least one sialic acid attached to a ceramide tail. Headgroup structure determines ganglioside nomenclature. Sialic acid structure also varies depending on the source.

Gangliosides have been observed to cluster into microdomains such as caveolae[98] or lipid rafts,[99] with other membrane components such as cholesterol and sphingomyelin, where they are implicated in a wide range of biological processes including cell-to-cell communication, adhesion, growth signaling, immunogenic response, and neuroprotection.[100] Because of their ubiquity and importance, many pathologies are also associated with aberrant expression of the gangliosides, mutations to ganglioside-interacting proteins, or the introduction of exogenous toxins that recognize them.[96,101–103] Exploring these broad and often difficult-to-elucidate ganglioside-mediated processes has required the development of new biosensing methodologies that will be the subject of future chapters.

1.6.1 Canonical Ganglioside-Binding Proteins

Many classes of proteins directly recognize sialic acid moieties or specific ganglioside structures. Lectins are a general class of carbohydrate-recognizing proteins with roles in cellular adhesion, recognition, and immune response.[104] They exist as transmembrane proteins, where they can bridge neighboring cells or participate in the internalization of glycosylated cargo in the extracellular space. Alternatively, many soluble lectins also exist with roles in immune response by binding to sugars on pathogen surfaces, along with roles in cellular adhesion and crosslinking.

Many lectins also specifically recognize sialic acid moieties and/or individual classes of gangliosides. The most relevant example is sialic acid binding immunoglobulin-type lectins (siglecs), with many forms residing in the membranes of B cells, mast cells, macrophages, and other immune cells, where they play critical roles in biomolecular recognition.[105] Additionally, myelin-associated glycoprotein (MAG) is a siglec believed to strongly influence myelination and myelin repair, offering one explanation for the high prevalence of gangliosides in neuronal tissue as well as their association with neuroprotection.[106] Gangliosides also act as recognition sites for numerous viral and bacterial toxins preceding entrance into cell membranes. Influenza hemagglutinin specificity for different sialic acid linkages (e.g. α2-6 for human respiratory tract and α2-3 for birds), determines which hosts can be infected, and mutations here are critical for jumping host species.[107] Bacterial toxins including cholera, tetanus, and botulinum have extremely high affinity for specific ganglioside structures, with the cholera toxin-GM1 interaction affinity values in the picomolar range reported.[108] Direct measurement of

ganglioside binding by recognizing molecules has long been conducted by a variety of methods, leaving few novel and/or valuable avenues of research remaining in this area.

1.6.2 Ganglioside-Regulated Membrane Proteins

Much harder to characterize and less explored are the effects of membrane ganglioside composition on neighboring transmembrane proteins. Often referred to as ganglioside lateral interactions, they've long been recognized as critical for cellular regulatory processes across a variety of different protein classes. The importance of understanding these regulatory mechanisms has become clear as changes resulting from altered ganglioside profiles have been increasingly associated with numerous pathologies. For example, accumulation of GM3 in adipose tissue has been recognized as having an inhibitory effect on insulin receptor signaling, thus leading to insulin resistance and downstream metabolic disease.[109] Additionally, gangliosides have been demonstrated to have complex roles in cellular Ca^{2+} homeostasis through plasma membrane Ca^{2+}-ATPASE (PMCA) and sarco/endoplasmic reticulum Ca^{2+}-ATPASE (SERCA), with tremendous implications on neuronal and vascular health respectively.[110,111] Interestingly, this system shows that different ganglioside structures can have completely opposite effects on protein activity, with poly-sialogangliosides having a positive effect and mono-sialogangliosides greatly reducing it.

Regulatory effects of gangliosides on receptor tyrosine kinases (RTKs), with specific emphasis on growth factor receptors, have been of particular interest due to their relevance to the proliferation of cancer. Gangliosides have been demonstrated to enhance

or retard downstream signaling of vascular epidermal, platelet-derived, and fibroblast growth factor receptors (VEGFR, PDGFR, and FGFR respectively), as well as every member of the ErbB family of proteins, depending on the particular protein and the ganglioside structure.[112] The ErbB family is one of the most widely researched groups of proteins due to their aberrant expression or activation being linked to uncontrolled cell growth and cancer.[113] Amongst this family is epidermal growth factor receptor (EGFR, HER1, ErbB1), with a long-known regulatory association with gangliosides. Specifically, the monosialoside GM3, in its most common biological form, has been shown to cause the greatest degree of inhibition for ligand-induced phosphorylation of EGFR.[114]

There are many different explanations for this inhibitory relationship that have been proposed including steric or conformational inhibition through direct binding, sequestration by lipid rafts, or regulation of endocytosis to name just a few.[115–118] Despite decades of research, the multifaceted mechanism of this regulation is not fully understood, and the relative impacts of these factors have not been established. In other words, the relationship between ganglioside structure, protein function, and downstream signaling has not been clearly and concisely established to show clear agreement between computational analysis and experimental results. The current understanding of EGFR's signaling mechanisms in relation to direct interactions with GM3 is largely reliant on computational modelling due primarily to the challenges of controlling for the many variables in a cellular system experimentally. For example, experimentally it has been shown that treating cells with GM3 reduces ligand-induced phosphorylation of EGFR,[114] but it is challenging to compare the relative effects of different GM3 structures. The difficulty arises from

assessing relative uptake and incorporation of the GM3, as well as how the structural differences can influence cellular enzymatic processes that degrade or modify the gangliosides. Furthermore, genetic drift of cell lines as well as experimental factors such as cell culture medium, fetal bovine serum choice, and treatment times can introduce significant variability. For these reasons, there is a growing need for platforms that allow for more precise control of the membrane environment, ganglioside structures, and other experimental conditions.

1.7 Lipid Bilayer Biointerfaces

From a biosensing perspective, there are a number of reasons to utilize a lipid membrane as the basis of the sensing platform. The first use case does not seek to elucidate lipid interactions, but rather the exact opposite. Lipid bilayers can act as excellent antifouling layers that greatly reduce nonspecific binding to the underlying substrate.[42] In the case of SPR, they can act as effective and more biologically relevant alternatives to the common carboxymethyl dextran surfaces, though with a reduced stability under certain buffer and regeneration conditions.[119,120] Furthermore, they can be formed through a huge variety of methods – each with particular benefits and drawbacks that can be selected based on the experimental needs and sensing modality.

Our group has demonstrated methods for the fabrication and application of silica-coated gold sensing chips for SPR generated through calcination or plasma-enhanced chemical vapor deposition (PECVD).[121–123] Hydrophilic surfaces such as silica, mica, and titanium dioxide can cause small lipid vesicles to spontaneously rupture, easily forming a

continuous supported lipid bilayer (SLB) that retains some lateral fluidity.[124] Other (hydrophobic) substrates such as gold can also achieve bilayer coverage, though often with more difficulty. Some examples of alternative deposition methods include Langmuir-Blodgett deposition,[125] solvent-assisted lipid bilayer formation,[126] and spin coating.[127] One large limitation of these methods that makes them poorly suited to use with SPR is that it is difficult or impossible to form the membranes in-line in the flow system, hurting reproducibility and precluding real-time monitoring of the membrane formation. It is also worth noting that lipid bilayers are also often captured on polymer cushions or tethers that offer a sub-membrane hydration layer that better accommodates diffusion studies and the incorporation of transmembrane proteins (Figure 1.11).[44,128]

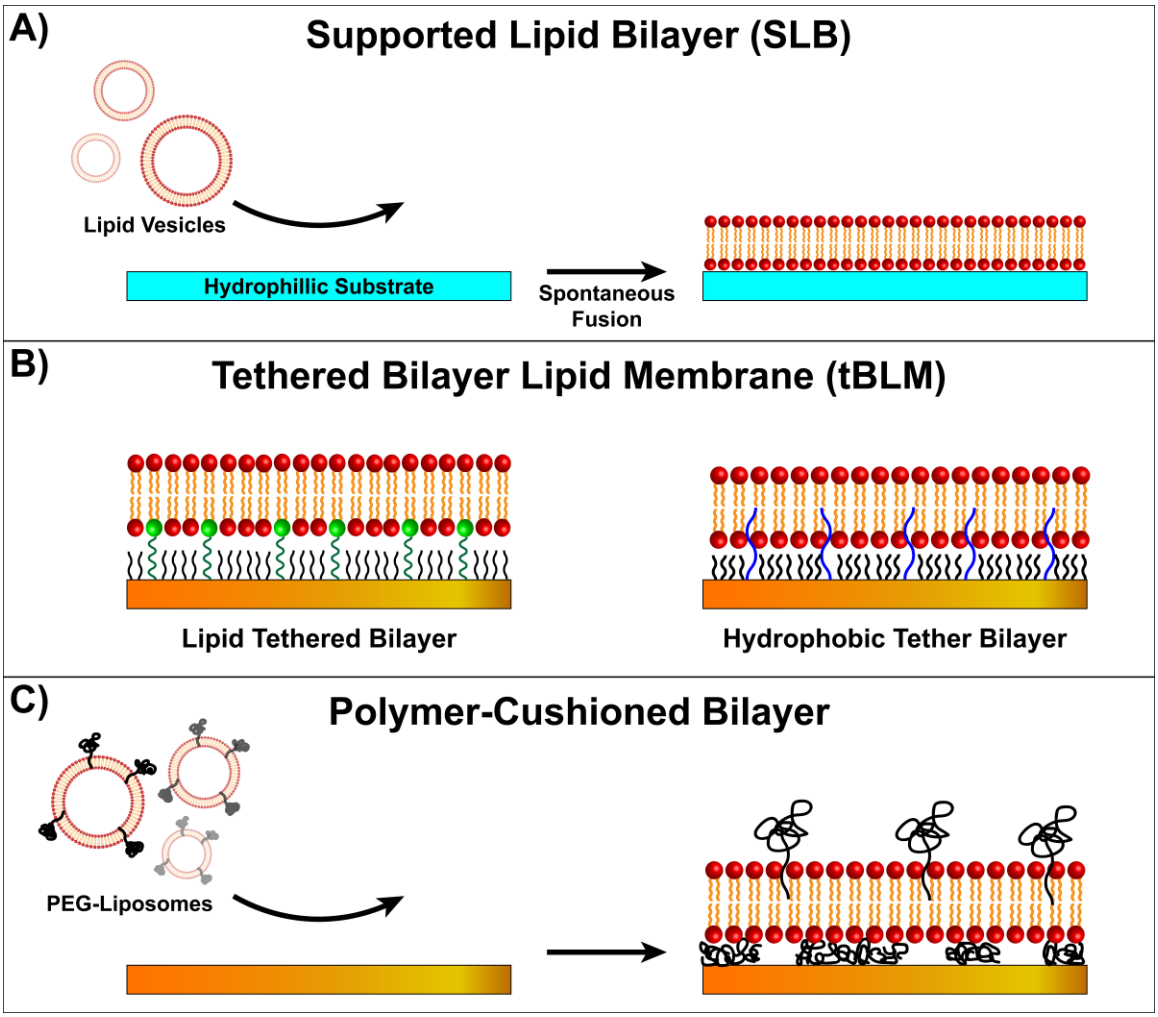

Figure 1.11. Overview of the three most common methods for bilayer formation on sensing surfaces. A) Supported lipid bilayers can be spontaneously formed on hydrophilic surfaces such as silica through incubation of vesicle suspensions. B) Tethered lipid bilayers can be formed on pre-functionalized surfaces (usually through gold-thiol bonds), creating a sub-membrane hydration layer that accommodates transmembrane proteins and diffusion across the membrane. C) Incorporation of large polymers such as polyethylene glycol (PEG) can allow for single-step bilayer formation on hydrophobic substrates and provides a hydration layer similar to tethered bilayers.

Bilayer interfaces are commonly used with electrochemical methods such as impedance spectroscopy to explore diffusion of molecules (drugs, ions, etc.) through the membrane either in the presence of or without channel proteins.[129] Additionally, they've been used extensively for the examination, disruption, and detection of pore-forming bacterial toxins such as streptolysin O (SLO) and cholera toxin (CT).[130,131] Other uses for lipid biointerfaces include mechanistic studies of proteins that directly interact with lipids based on their curvature or composition such as bridging integrator 1 (BIN1) and alpha synuclein (α-syn).[123] Another growing area of interest is in exploring how the presence of a membrane or its composition affects the binding properties of membrane-associated proteins through mechanisms such as lateral interactions and diffusion. Determining these correlations, however, requires methods that allow for thorough characterization of the lipid bilayer.

1.7.1 Characterization of Membrane Properties

There are a great deal of membrane properties that may be of interest depending on the scientific question being explored. Some important ones include membrane formation dynamics, electrical sealing, lateral diffusion, protein incorporation, bilayer thickness, presence of lipid subdomains (rafts), and membrane charge. As it is not feasible to cover every technique used for characterizing this vast swath of membrane properties, we will focus on those most relevant to the goals of this work – namely those for quantification of lateral diffusion, lipid subdomain formation, and protein incorporation. Amongst these areas, microscopy techniques are the most relevant and informative.

In living membrane systems, as well as specifically formulated artificial systems, certain membrane components have a propensity to be sequestered into microdomains often referred to as lipid rafts. These domains are generally enriched in cholesterol, sphingomyelin, and other specialized membrane components such as gangliosides. These domains are both dynamic and transient, and act as important terminals for numerous cellular processes.[132] Most important for this work is their role in signal transduction regulation, where they can act to either concentrate or isolate cell surface receptors that are dependent on proximity to other receptors and coreceptors for function. EGFR is one of these receptors, with many studies indicating that clustering in these low-fluidity domains after ligand-binding is crucial for downstream signaling.[133] Furthermore, computational studies have also shown clustering of GM3 around EGFR in lipid rafts, offering potential insights into GM3's inhibitory mechanisms.[117]

Due to their small size and transient nature, direct imaging of lipid rafts has been difficult to achieve with optical methods. However, imaging of these domains has been achieved in solution using liquid AFM, thereby allowing for both quantification and analysis of their interactions with proteins such as α-syn.[134,135] The downside of this option is that it requires specialized instrumentation, probes, and procedures to achieve high quality imaging. However, raft formation through their general effects on lipid diffusion can be indirectly inferred using a more accessible method, possible on most modern fluorescent confocal microscopes, called fluorescence recovery after photobleaching (FRAP).[136]

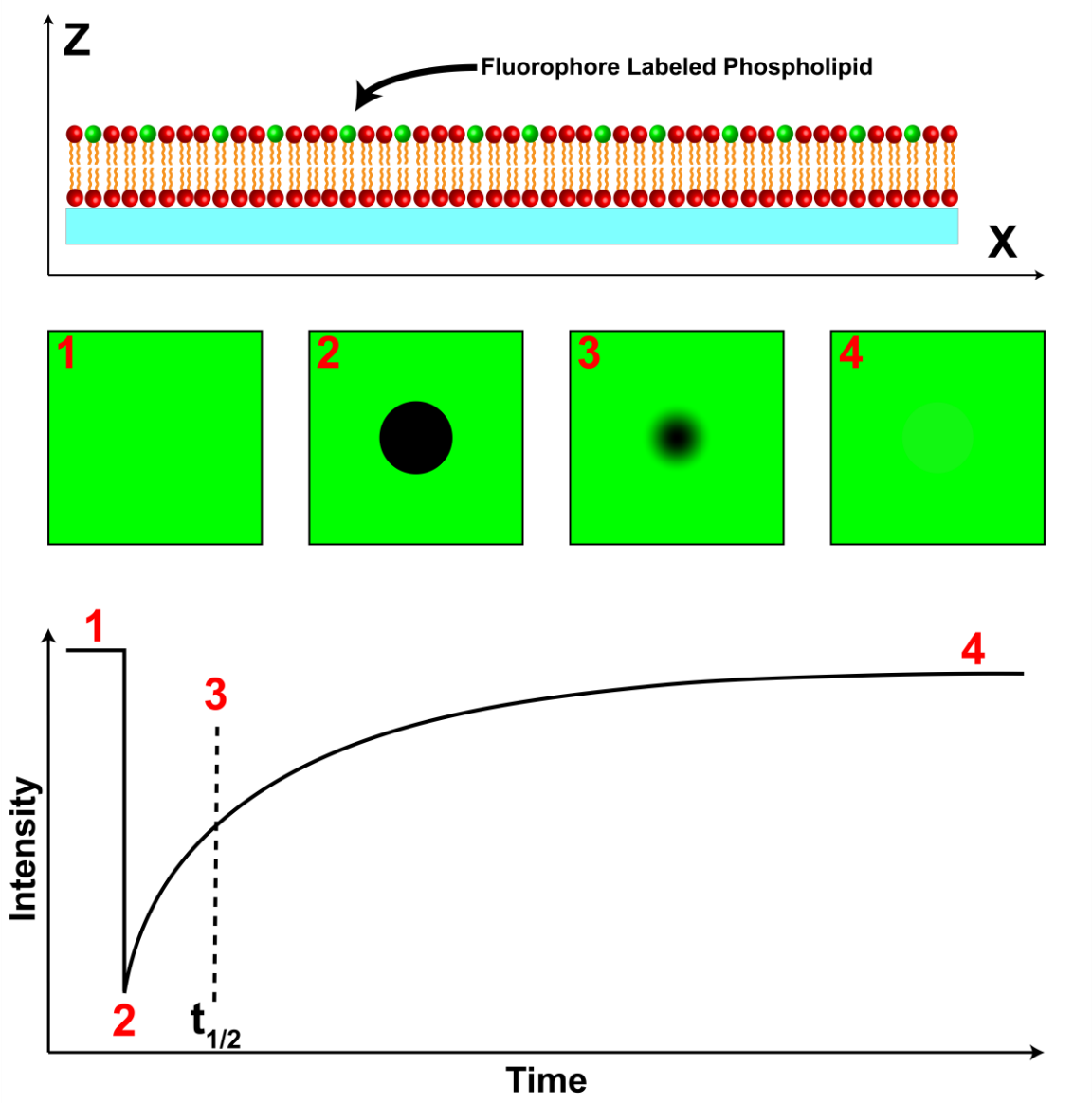

Figure 1.12. Schematic illustration of fluorescence recovery after photobleaching on a supported lipid bilayer containing fluorophore labeled lipids. Top-down views of the surface and corresponding intensities within the bleach area are plotted against time. The time points correspond to pre-bleach (1), immediate post-bleach (2), half-time recovery (3), and final recovery (4).

This technique works through the introduction of a small percentage of fluorophore-tagged lipids to the membrane. To determine fluidity, a small region of the membrane can be bleached under intense illumination, followed by monitoring of the recovery of fluorescence within that region (Figure 1.12). Because the entire imaged area will slowly bleach during measurement, the fluorescence intensity within the bleach area (F_{bleach}) must be corrected ratiometrically with the intensity in a reference area ($F_{\text{reference}}$).

$$F_{\text{c}} = \frac{F_{\text{bleach}}}{F_{\text{reference}}} \tag{1.17}$$

These values, taken at many time points over the recovery period, can be used to the fluorescence fractional recovery (F_{FR}), otherwise describable as the intensity of the bleached reason normalized to the pre-bleach intensity (F_0).

$$F_{\text{FR}} = \frac{F_{\text{c}} - F_0}{1 - F_0} \tag{1.18}$$

Next, the F_{FR} values are plotted vs time and fitted the plot with the following first-order exponential equation:

$$y = a(1 - e^{-bx}) \tag{1.19}$$

Taking the determined variable b from the best fit of the recovery curve, the half-time recovery ($t_{1/2}$) can then be calculated:

$$t_{1/2} = \frac{\ln(2)}{b} \tag{1.20}$$

Finally, the $t_{1/2}$ can be used to determine the diffusion coefficient (D), typically presented in units of $\mu m^2 s^{-1}$. Where ω is equal to the radius of the bleach spot, the following equation is used:

$$D = \frac{\omega^2}{4t_{1/2}} \tag{1.21}$$

It should be noted that these equations only hold for uniform (flat) bleaching profiles that can be easily achieved on modern confocal microscopes, rather than the gaussian profiles that might be expected in the past. If the bleach profile is gaussian, the beam profile and a correction factor must be considered as was proposed in early FRAP by Axelrod in 1976.[137] While we have only presented FRAP in the context of measuring the diffusion of lipids, and that application is the only one demonstrated later in this work, please note that it is often used to determine the diffusion of membrane proteins as well. This could be of particular interest when evaluating the effects of membrane lipids on protein diffusion, with implications on their regulatory mechanisms.[138]

1.8 Aims and Scope of Dissertation

The overall goal of this dissertation is to expand the range of applications that can be explored with biosensing technologies. Across this work, developments across every major aspect of SPR biosensing will be reported. This begins with the transduction element, where fundamental explorations in the characterization and utilization of new plasmonic materials will be conducted. Next, we explore methodological considerations for collection and analysis of high quality SPR data for drugs with non-standard binding behaviors. Finally, we focus on the development of biointerfaces that allow for the exploration of entirely new biological phenomena with SPR. The primary value of these innovations is the broad applicability of the methods to address any number of material or biological systems.

Chapter 2 presents an exploration of the physical, optical, and plasmonic properties of indium thin films. In this chapter we provide the first ever example of Kretschmann configuration SPR sensing with these substrates, thereby expanding the range of accessible metals. Furthermore, characterization of previously unavailable optical and morphological information about indium and its oxide layer should aid future researchers in optimizing indium films for SPR, as well as other applications. Finally, a new workflow for generating models of thin film surfaces obtained from AFM and importing them into finite-difference time domain (FDTD) for simulations of electronic field enhancement was demonstrated.

Chapter 3 changes gears to consider methodology and data analysis for protein-drug interactions on commercially available SPR chips. Here high-quality SPR data is generated for monovalent, bivalent, and covalent inhibitors by determining the optimal experimental parameters for each class of drug, with a particular focus on the choice of immobilization method. Furthermore, we present the importance of the choice of fitting model based on drug class, as well as how to extract and compare the wanted kinetic and affinity information from those fits. From this information it was determined that the bivalent analytes here have affinities that far outperform their monovalent counterparts, mainly owing to greatly reduced dissociation rates. It was also found that the covalent inhibitors showed slightly higher inactivation efficiencies at higher temperatures, driven by much faster rates of inactivation and dampened by lower binding affinity. The ability of SPR to provide these individual parameters and guide future optimization of the inhibitors is presented as particularly valuable.

Chapter 4 focuses on the development of a lipid bilayer biointerface for interrogating the effects of ganglioside structures on both lipid diffusion and EGFR regulation. Implementing synthetically pure gangliosides with artificial membrane mimics allows for high control of membrane composition that is not possible in cell studies. In this chapter we screen the diffusion coefficients of membranes containing gangliosides with different fatty acyl chains, sphingosines, and headgroup compositions. Additionally, with new chemoenzymatic synthetic methods, fluorophore-tagged gangliosides were synthesized and examined for their membrane diffusion. Finally, a new bilayer-based platform and methodology was developed to examine how the presence and composition

of the membrane affects EGFR's affinity for EGF. This dual synthetic and bioanalytical study provides valuable information about how ganglioside structure affects biological function and provides a platform with broad applicability to numerous protein systems.

Chapter 5 details our attempts to isolate full-length membrane-bound EGFR for implementation into biosensing platforms. We achieved this by inducing the release of membrane fractions from EGFR-containing HeLa and A431 cells. We optimized and compared three different methods for forming these cell membrane fractions using nano tracking analysis and western blot quantification. Through these experiments we identified osmotic shock as the most optimal in terms of both EGFR yield and experimental feasibility. Finally, we detail initial testing to capture the membrane fractions on a commercial lipophilic SPR chip, thereby laying the groundwork for future surface-based biosensing explorations of ganglioside effects on the function of full-length EGFR.

1.9 References

1. Haleem, A., Javaid, M., Singh, R. P., Suman, R. & Rab, S. Biosensors applications in medical field: A brief review. *Sensors International* **2**, 100100 (2021).

2. Acharya, B., Behera, A. & Behera, S. Optimizing drug discovery: Surface plasmon resonance techniques and their multifaceted applications. *Chemical Physics Impact* **8**, 100414 (2024).

3. Williams, A. *et al.* Biosensors for Public Health and Environmental Monitoring: The Case for Sustainable Biosensing. *ACS Sustain. Chem. Eng.* **12**, 10296–10312 (2024).

4. Skládal, P. Piezoelectric biosensors: shedding light on principles and applications. *Microchimica Acta* **191**, 184- (2024).

5. Suthar, J., Parsons, E. S., Hoogenboom, B. W., Williams, G. R. & Guldin, S. Acoustic Immunosensing of Exosomes Using a Quartz Crystal Microbalance with Dissipation Monitoring. *Anal. Chem.* **92**, 4082–4093 (2020).

6. Wang, H. *et al.* Rapid and Sensitive Detection of Campylobacter jejuni in Poultry Products Using a Nanoparticle-Based Piezoelectric Immunosensor Integrated with Magnetic Immunoseparation. *J. Food Prot.* **81**, 1321–1330 (2018).

7. Yao, J. *et al.* Blood Coagulation Testing Smartphone Platform Using Quartz Crystal Microbalance Dissipation Method. *Sensors 2018, Vol. 18, Page 3073* **18**, 3073 (2018).

8. Kim, N. S. & Kim, J. Advancing non-faradaic impedance biosensors: sensitivity enhancement strategies using microfluidics, multiscale labeling, and CMOS technology. *Microsystems & Nanoengineering 2026 12:1* **12**, 117- (2026).

9. Hassan, R. Y. A. Advances in Electrochemical Nano-Biosensors for Biomedical and Environmental Applications: From Current Work to Future Perspectives. *Sensors (Basel)* **22**, 7539 (2022).

10. Pashchenko, O., Shelby, T., Banerjee, T. & Santra, S. A comparison of optical, electrochemical, magnetic, and colorimetric point-of-care biosensors for infectious disease diagnosis. *ACS Infect. Dis.* **4**, 1162 (2018).

11. Singh, A. *et al.* Recent Advances in Electrochemical Biosensors: Applications, Challenges, and Future Scope. *Biosensors 2021, Vol. 11, Page 336* **11**, 336 (2021).

12. Akgönüllü, S. & Denizli, A. Recent advances in optical biosensing approaches for biomarkers detection. *Biosens. Bioelectron. X* **12**, 100269 (2022).

13. Strianese, M. *et al.* Fluorescence-based biosensors. *Methods in Molecular Biology* **875**, 193–216 (2012).

14. Koczula, K. M. & Gallotta, A. Lateral flow assays. *Essays Biochem.* **60**, 111 (2016).

15. Park, J. An Optimized Colorimetric Readout Method for Lateral Flow Immunoassays. *Sensors (Basel)* **18**, 4084 (2018).

16. Roda, B. *et al.* Shining light on biosensors: Chemiluminescence and bioluminescence in enabling technologies. *TrAC Trends in Analytical Chemistry* **180**, 117975 (2024).

17. Wang, X. *et al.* Fluorescent Probes for Disease Diagnosis. *Chem. Rev.* **124**, 7106 (2024).

18. Tian, X., Murfin, L. C., Wu, L., Lewis, S. E. & James, T. D. Fluorescent small organic probes for biosensing. *Chem. Sci.* **12**, 3406 (2021).

19. Musumeci, D., Platella, C., Riccardi, C., Moccia, F. & Montesarchio, D. Fluorescence Sensing Using DNA Aptamers in Cancer Research and Clinical Diagnostics. *Cancers 2017, Vol. 9, Page 174* **9**, 174 (2017).

20. Banik, S. M. *et al.* Lysosome-targeting chimaeras for degradation of extracellular proteins. *Nature 2020 584:7820* **584**, 291–297 (2020).

21. Chen, K., Yan, R., Xiang, L. & Xu, K. Excitation spectral microscopy for highly multiplexed fluorescence imaging and quantitative biosensing. *Light: Science & Applications 2021 10:1* **10**, 97 (2021).

22. Hussain, A. *et al.* Fluorescence-based sensors for environmental monitoring of small hazardous molecules: Recent trends and future prospects. *Microchemical Journal* **218**, 115386 (2025).

23. Toseland, C. P. Fluorescent labeling and modification of proteins. *J. Chem. Biol.* **6**, 85 (2013).

24. Yin, L. *et al.* How does fluorescent labeling affect the binding kinetics of proteins with intact cells? *Biosens. Bioelectron.* **66**, 412 (2014).

25. Kabashin, A. V., Kravets, V. G. & Grigorenko, A. N. Label-free optical biosensing: going beyond the limits. *Chem. Soc. Rev.* **52**, 6554–6585 (2023).

26. Jha, R., Gorai, P., Shrivastav, A. & Pathak, A. Label-Free Biochemical Sensing Using Processed Optical Fiber Interferometry: A Review. *ACS Omega.* **9**, 3 (2023).

27. Butt, M. A. Surface Plasmon Resonance-Based Biodetection Systems: Principles, Progress and Applications—A Comprehensive Review. *Biosensors (Basel).* **15**, 35 (2025).

28. Topor, C. V., Puiu, M. & Bala, C. Strategies for Surface Design in Surface Plasmon Resonance (SPR) Sensing. *Biosensors (Basel).* **13**, 465 (2023).

29. Homola, J. Surface plasmon resonance sensors for detection of chemical and biological species. *Chem. Rev.* **108**, 462–493 (2008).

30. Maisonneuve, M., Song, I.-H., Patskovsky, S. & Meunier, M. Polarimetric total internal reflection biosensing. *Optics Express.* **19**, 7410–7416 (2011).

31. Raether, H., Hohler, G. & Niekisch, E. A. Surface Plasmons on Smooth and Rough Surfaces and on Gratings. *Springer Tracts in Modern Physics* **111**, 136 (1988).

32. Heavens, O. S. Optical properties of thin films. *Reports on Progress in Physics* **23**, 1 (1960).

33. Hansen, W. N. Electric Fields Produced by the Propagation of Plane Coherent Electromagnetic Radiation in a Stratified Medium. *JOSA* **58**, 380–390 (1968).

34. Costa, E. B., Rodrigues, E. P. & Pereira, H. A. Sim-SPR: an Open-Source Surface Plasmon Resonance Simulator for Academic and Industrial Purposes. *Plasmonics* **14**, 1699–1709 (2019).

35. Yu, X. *et al.* Sensitivity enhancement of surface plasmon resonance biosensors based on versatile nanostructures: principle, fabrication, and illustrative applications. *Microsystems & Nanoengineering 2026* **12**, 45 (2026).

36. Murugan, D. *et al.* Recent Advances in Grating Coupled Surface Plasmon Resonance Technology. *Adv. Opt. Mater.* **12**, 2401862 (2024).

37. Kretschmann, E. & Raether, H. Radiative Decay of Non Radiative Surface Plasmons Excited by Light. *Zeitschrift fur Naturforschung - Section A Journal of Physical Sciences* **23**, 2135–2136 (1968).

38. Otto, A. Excitation of nonradiative surface plasma waves in silver by the method of frustrated total reflection. *Zeitschrift für Physik* **216**, 398–410 (1968).

39. Lv, J. *et al.* Recent advances of optical fiber biosensors based on surface plasmon resonance: sensing principles, structures, and prospects. *Sensors & Diagnostics* **3**, 1369–1391 (2024).

40. Lichtenberg, J. Y., Ling, Y. & Kim, S. Non-Specific Adsorption Reduction Methods in Biosensing. *Sensors* **19**, 2488 (2019).

41. Silin, V., Weetall, H. & Vanderah, D. J. SPR Studies of the Nonspecific Adsorption Kinetics of Human IgG and BSA on Gold Surfaces Modified by Self-Assembled Monolayers (SAMs). *J. Colloid Interface Sci.* **185**, 94–103 (1997).

42. Stuart, D. D., Pike, C. D., Malinick, A. S. & Cheng, Q. Characterization of a Charged Biomimetic Lipid Membrane for Unique Antifouling Effects against Clinically Relevant Matrices in Biosensing. *ACS Appl. Mater. Interfaces* **16**, 56447 (2024).

43. Uchida, K., Otsuka, H., Kaneko, M., Kataoka, K. & Nagasaki, Y. A reactive poly(ethylene glycol) layer to achieve specific surface plasmon resonance sensing with a high S/N ratio: The substantial role of a short underbrushed PEG layer in minimizing nonspecific adsorption. *Anal. Chem.* **77**, 1075–1080 (2005).

44. Krage, C. *et al.* Three-Dimensional Polyglycerol-PEG-Based Hydrogels as a Universal High-Sensitivity Platform for SPR Analysis. *Anal. Chem.* **97**, 6329–6337 (2025).

45. Malinick, A. S. *et al.* Curvature-tuning membrane mimetics as novel sensing interface to probe affinity fluctuation of bridging integrator 1 protein by SPR. *Biosens. Bioelectron.* **287**, 117713 (2025).

46. Malinick, A. S. *et al.* Detection of Multiple Sclerosis Biomarkers in Serum by Ganglioside Microarrays and Surface Plasmon Resonance Imaging. *ACS Sens.* **5**, 3617–3626 (2020).

47. Peltomaa, R., Glahn-Martínez, B., Benito-Peña, E. & Moreno-Bondi, M. C. Optical Biosensors for Label-Free Detection of Small Molecules. *Sensors (Basel)* **18**, 4126 (2018).

48. Koyappayil, A. & Lee, M. H. Ultrasensitive Materials for Electrochemical Biosensor Labels. *Sensors (Basel)* **21**, 89 (2020).

49. Lu, H. & Tonge, P. J. Drug-Target Residence Time: Critical Information for Lead Optimization. *Curr. Opin. Chem. Biol.* **14**, 467 (2010).

50. O'Shannessy, D. J., Brigham-Burke, M., Karl Soneson, K., Hensley, P. & Brooks, I. Determination of rate and equilibrium binding constants for macromolecular interactions using surface plasmon resonance: Use of nonlinear least squares analysis methods. *Anal. Biochem.* **212**, 457–468 (1993).

51. Henseleit, A. *et al.* Kinetic Analyses of Data from a Human Serum Albumin Assay Using the liSPR System. *Biosensors (Basel).* **5**, 27 (2015).

52. Petryayeva, E. & Krull, U. J. Localized surface plasmon resonance: nanostructures, bioassays and biosensing--a review. *Anal. Chim. Acta* **706**, 8–24 (2011).

53. Bonyár, A. Maximizing the Surface Sensitivity of LSPR Biosensors through Plasmon Coupling—Interparticle Gap Optimization for Dimers Using Computational Simulations. *Biosensors (Basel).* **11**, 527 (2021).

54. Kim, D. M., Park, J. S., Jung, S. W., Yeom, J. & Yoo, S. M. Biosensing Applications Using Nanostructure-Based Localized Surface Plasmon Resonance Sensors. *Sensors* **21**, 3191 (2021).

55. Hong, X. & Hall, E. A. H. Contribution of gold nanoparticles to the signal amplification in surface plasmon resonance. *Analyst* **137**, 4712–4719 (2012).

56. Pilot, R. *et al.* A Review on Surface-Enhanced Raman Scattering. *Biosensors (Basel).* **9**, 57 (2019).

57. Luo, S., Ren, X., Lin, H., Song, H. & Ye, J. Plasmonic photothermal catalysis for solar-to-fuel conversion: current status and prospects. *Chem. Sci.* **12**, 5701 (2021).

58. Fu, L., Lin, C. Te, Karimi-Maleh, H., Chen, F. & Zhao, S. Plasmonic Nanoparticle-Enhanced Optical Techniques for Cancer Biomarker Sensing. *Biosensors* **13**, 977 (2023).

59. Naik, G. V *et al.* Alternative Plasmonic Materials: Beyond Gold and Silver. *Advanced Materials* **25**, 3264–3294 (2013).

60. Treebupachatsakul, T., Boosamalee, A., Chaithatwanitch, K. & Pechprasarn, S. Generalized figure of merit for plasmonic dip measurement-based surface plasmon resonance sensors. *Biomedical Optics Express* **13**, 1784–1800 (2022).

61. Lindquist, N. C., Nagpal, P., McPeak, K. M., Norris, D. J. & Oh, S. H. Engineering metallic nanostructures for plasmonics and nanophotonics. *Rep. Prog. Phys.* **75**, 036501 (2012).

62. West, P. R. *et al.* Searching for better plasmonic materials. *Laser Photon. Rev.* **4**, 795–808 (2010).

63. Tao, L. *et al.* Experimental Investigation of the Dielectric Constants of Thin Noble Metallic Films Using a Surface Plasmon Resonance Sensor. *Sensors (Basel)* **20**, 1505 (2020).

64. Chirco, A., Meacci, E. & Margheri, G. A Tutorial Review on Surface Plasmon Resonance Biosensors: Applications in Biomedicine. *ACS Bio and Med Chem Au* **5**, 922–946 (2025).

65. Lu, M. *et al.* Optimization of Surface Plasmon Resonance Biosensor with Ag/Au Multilayer Structure and Fiber-Optic Miniaturization. *Plasmonics* **12**, 663–673 (2017).

66. Wang, L. *et al.* Sensitivity enhancement of SPR biosensor with silver mirror reaction on the Ag/Au film. *Talanta* **78**, 265–269 (2009).

67. Das, C. M. *et al.* Improving the Sensitivity of SPR Sensors with Au–Ag alloys and 2D Materials — a Simulation-Based Approach. *Adv. Theory Simul.* **4**, 2100292 (2021).

68. Choi, S. H., Kim, Y. L. & Byun, K. M. Graphene-on-silver substrates for sensitive surface plasmon resonance imaging biosensors. *Optics Express* **19**, 458–466 (2011).

69. Gerard, D. & Gray, S. K. Aluminium plasmonics. *J. Phys. D Appl. Phys.* **48**, 184001 (2014).

70. González-Campuzano, R., Saniger, J. M. & Mendoza, D. Plasmonic resonances in hybrid systems of aluminum nanostructured arrays and few layer graphene within the UV–IR spectral range. *Nanotechnology* **28**, 465704 (2017).

71. Shukla, S. & Arora, P. Multiwavelength plasmonic activity in aluminum-based 2D nanostructures for biosensing applications. *J. Comput. Electron.* **21**, 618–624 (2022).

72. Nguyen, L. *et al.* Atomic-Scale Insights into the Oxidation of Aluminum. *ACS Appl. Mater. Interfaces* **10**, 2230–2235 (2018).

73. Detweiler, Z. M., Wulfsberg, S. M., Frith, M. G., Bocarsly, A. B. & Bernasek, S. L. The oxidation and surface speciation of indium and indium oxides exposed to atmospheric oxidants. *Surf. Sci.* **648**, 188–195 (2016).

74. Correa, G. C., Bao, B. & Strandwitz, N. C. Chemical stability of titania and alumina thin films formed by atomic layer deposition. *ACS Appl. Mater. Interfaces* **7**, 14816–14821 (2015).

75. Lambert, A. S., Valiulis, S. N., Malinick, A. S., Tanabe, I. & Cheng, Q. Plasmonic Biosensing with Aluminum Thin Films under the Kretschmann Configuration. *Anal. Chem.* **92**, 8654–8659 (2020).

76. El Biyari, N. Surface plasmon resonance biosensors: Advancements, applications, and future directions in molecular detection. *Biotechnology Notes* **7**, 22 (2026).

77. Foltýn, M., Patočka, M., Řepa, R., Šikola, T. & Horák, M. Influence of Deposition Parameters on the Plasmonic Properties of Gold Nanoantennas Fabricated by Focused Ion Beam Lithography. *ACS Omega* **9**, 37408 (2024).

78. Goldstein, J. I. *et al.* Scanning electron microscopy and x-ray microanalysis. *Scanning Electron Microscopy and X-ray Microanalysis* 1–550 (2017)

79. Treebupachatsakul, T., Shinnakerdchoke, S. & Pechprasarn, S. Analysis of Effects of Surface Roughness on Sensing Performance of Surface Plasmon Resonance Detection for Refractive Index Sensing Application. *Sensors (Basel)* **21**, 6164 (2021).

80. Jalili, N. & Laxminarayana, K. A review of atomic force microscopy imaging systems: application to molecular metrology and biological sciences. *Mechatronics* **14**, 907–945 (2004).

81. Schmidl, G. *et al.* Confocal sputtering of (111) orientated smooth gold films for surface plasmon resonance approaches. *Vacuum* **138**, 55–63 (2017).

82. Costa, D. *et al.* Tuning the Refractive Index Sensitivity of LSPR Transducers Based on Nanocomposite Thin Films Composed of Noble Metal Nanoparticles Dispersed in TiO2. *Materials* **16**, 7355 (2023).

83. Dinnebier E, R. & Billinge JL, S. Powder Diffraction: Theory and Practice. *Powder Diffr.*(2008)

84. Marra, W. C., Eisenberger, P. & Cho, A. Y. X-ray total-external-reflection–Bragg diffraction: A structural study of the GaAs-Al interface. *J. Appl. Phys.* **50**, 6927–6933 (1979).

85. Birkholz, M. Thin Film Analysis by X-Ray Scattering. *Thin Film Analysis by X-Ray Scattering* 1–356 (2006)

86. McPeak, K. M. *et al.* Plasmonic films can easily be better: Rules and recipes. *ACS Photonics* **2**, 326–333 (2015).

87. Abbas, R. R., Richardson, T. H., Hobson, A., Hassan, A. & Abbas, T. R. Effect of annealing on the surface plasmon resonance of dodecanethiol encapsulated gold nanoparticles Langmuir–Schafer thin films. *Colloids Surf. A Physicochem. Eng. Asp.* **444**, 95–103 (2014).

88. Oliveira, L. C., Moreira, C. S., Neff, H. & Lima, A. M. N. Optical Properties and Instrumental Performance of thin Noble Metal (Cu, Au, Ag) Films Near the Surface Plasmon Resonance. *Procedia Eng.* **168**, 834–837 (2016).

89. Seah, M. P. & Dench, W. A. Quantitative electron spectroscopy of surfaces: A standard data base for electron inelastic mean free paths in solids. *Surface and Interface Analysis* **1**, 2–11 (1979).

90. Thompson, M. W., Colligon, J. S., Smith, R. & Hofmann, S. Sputter-depth profiling for thin-film analysis. *Philosophical Transactions of the Royal Society A: Mathematical, Physical and Engineering Sciences* **362**, 55–75 (2004).

91. Tompkins, H. G. & Irene, E. A. Handbook of Ellipsometry. *Handbook of Ellipsometry* **15**, 1–870 (2005).

92. Synowicki, R. A. Spectroscopic ellipsometry characterization of indium tin oxide film microstructure and optical constants. *Thin Solid Films* **313–314**, 394–397 (1998).

93. Merrill Jr., A. H. Sphingolipid and glycosphingolipid metabolic pathways in the era of sphingolipidomics. *Chem Rev* **111**, 6387–6422 (2011).

94. Li, Q., Xie, Y., Wong, M. & Lebrilla, C. B. Characterization of Cell Glycocalyx with Mass Spectrometry Methods. *Cells* **8**, (2019).

95. O'Brien, J. P. & Brodbelt, J. S. Structural characterization of gangliosides and glycolipids via ultraviolet photodissociation mass spectrometry. *Anal Chem* **85**, 10399–10407 (2013).

96. Sipione, S., Monyror, J., Galleguillos, D., Steinberg, N. & Kadam, V. Gangliosides in the Brain: Physiology, Pathophysiology and Therapeutic Applications. *Front. Neurosci.* **14**, 572965 (2020).

97. Hedlund, M., Padler-Karavani, V., Varki, N. M. & Varki, A. Evidence for a human-specific mechanism for diet and antibody-mediated inflammation in carcinoma progression. *Proc. Natl. Acad. Sci. U. S. A.* **105**, 18936–18941 (2008).

98. Singh, R. D. *et al.* Gangliosides and β1-Integrin Are Required for Caveolae and Membrane Domains. *Traffic* **11**, 348–360 (2010).

99. Fantini, J. & Fantini, C. J. Lipid rafts and human diseases: why we need to target gangliosides. *FEBS Open Bio* **13**, 1636–1650 (2023).

100. Lopez, P. H. & Schnaar, R. L. Gangliosides in cell recognition and membrane protein regulation. *Curr. Opin. Struct. Biol.* **19**, 549–557 (2009).

101. Mlinac-Jerkovic, K., Heffer, M. & Schnaar, R. L. Gangliosides in molecular interactions and cell regulation. *Journal of Biological Chemistry* **302**, 111184 (2026).

102. Zuverink, M. & Barbieri, J. T. Protein Toxins That Utilize Gangliosides as Host Receptors. *Prog. Mol. Biol. Transl. Sci.* **156**, 325–354 (2018).

103. Palomo, A. G. *et al.* Frequent co-expression of EGFR and NeuGcGM3 ganglioside in cancer: it's potential therapeutic implications. *Clin. Exp. Metastasis* **33**, 717–725 (2016).

104. Raposo, C. D., Canelas, A. B. & Barros, M. T. Human Lectins, Their Carbohydrate Affinities and Where to Find Them. *Biomolecules* **11**, 188 (2021).

105. Crocker, P. R., Paulson, J. C. & Varki, A. Siglecs and their roles in the immune system. *Nature Reviews Immunology* **7**, 255–266 (2007).

106. Mehta, N. R., Nguyen, T., Bullen, J. W., Griffin, J. W. & Schnaar, R. L. Myelin-associated glycoprotein (MAG) protects neurons from acute toxicity using a ganglioside-dependent mechanism. *ACS Chem. Neurosci.* **1**, 215–222 (2010).

107. Suzuki, Y. Gangliosides as influenza virus receptors. Variation of influenza viruses and their recognition of the receptor sialo-sugar chains. *Prog. Lipid Res.* **33**, 429–457 (1994).

108. Jordan, C. *et al.* Probing the Origin of Affinity in the GM1-Cholera Toxin Complex through Site-Selective Editing with Fluorine. *ACS Cent. Sci.* **10**, 1481–1489 (2024).

109. Kabayama, K. *et al.* Dissociation of the insulin receptor and caveolin-1 complex by ganglioside GM3 in the state of insulin resistance. *Proc. Natl. Acad. Sci. U.S.A.* **104**, 13678–13683 (2007).

110. Jiang, L. *et al.* Effects of gangliosides on the activity of the plasma membrane Ca2 +-ATPase. *Biochimica et Biophysica Acta (BBA) - Biomembranes* **1838**, 1255–1265 (2014).

111. Ginzburg, L., Li, S. C., Li, Y. T. & Futerman, A. H. An exposed carboxyl group on sialic acid is essential for gangliosides to inhibit calcium uptake via the sarco/endoplasmic reticulum Ca2+-ATPase: relevance to gangliosidoses. *J. Neurochem.* **104**, 140–146 (2008).

112. Kaucic, K., Liu, Y. & Ladisch, S. Modulation of Growth Factor Signaling by Gangliosides: Positive Or Negative? *Methods Enzymol.* **417**, 168 (2006).

113. Roskoski, R. The ErbB/HER family of protein-tyrosine kinases and cancer. *Pharmacol. Res.* **79**, 34–74 (2014).

114. Meuillet, E. J., Mania-Farnell, B., George, D., Inokuchi, J. I. & Bremer, E. G. Modulation of EGF Receptor Activity by Changes in the GM3 Content in a Human Epidermoid Carcinoma Cell Line, A431. *Exp. Cell Res.* **256**, 74–82 (2000).

115. Kawashima, N., Yoon, S. J., Itoh, K. & Nakayama, K. I. Tyrosine Kinase Activity of Epidermal Growth Factor Receptor Is Regulated by GM3 Binding through Carbohydrate to Carbohydrate Interactions. *Journal of Biological Chemistry* **284**, 6147–6155 (2009).

116. Yoon, S. J., Nakayama, K. I., Hikita, T., Handa, K. & Hakomori, S. I. Epidermal growth factor receptor tyrosine kinase is modulated by GM3 interaction with N-linked GlcNAc termini of the receptor. *Proc. Natl. Acad. Sci. U. S. A.* **103**, 18987 (2006).

117. Shorthouse, D., Hedger, G., Koldsø, H. & Sansom, M. S. P. Molecular simulations of glycolipids: Towards mammalian cell membrane models. *Biochimie* **120**, 105–109 (2016).

118. Gu, R. X., Ingólfsson, H. I., De Vries, A. H., Marrink, S. J. & Tieleman, D. P. Ganglioside-Lipid and Ganglioside-Protein Interactions Revealed by Coarse-Grained and Atomistic Molecular Dynamics Simulations. *Journal of Physical Chemistry B* **121**, 3262–3275 (2017).

119. Cytiva. *Biacore Sensor Surface Handbook*. (Cytiva, Uppsala, Sweden, 2022).

120. Del Vecchio, K. & Stahelin, R. V. Using surface plasmon resonance to quantitatively assess lipid–protein interactions. *Methods in Molecular Biology* **1376**, 141–153 (2016).

121. Hinman, S. S., Ruiz, C. J., Drakakaki, G., Wilkop, T. E. & Cheng, Q. On-Demand Formation of Supported Lipid Membrane Arrays by Trehalose-Assisted Vesicle Delivery for SPR Imaging. *ACS Appl. Mater. Interfaces* **7**, 17122–17130 (2015).

122. Duan, J., Linman, M. & Cheng, Q. Ultrathin Calcinated Films on a Gold Surface for Highly Effective Laser Desorption/Ionization of Biomolecules. *Anal. Chem.* **82**, 5088–5094 (2010).

123. Malinick, A. S., Stuart, D. D., Lambert, A. S. & Cheng, Q. Curved Membrane Mimics for Quantitative Probing of Protein-Membrane Interactions by Surface Plasmon Resonance. *ACS Appl. Mater. Interfaces* **16**, 84–94 (2024).

124. Tamm, L. K. & McConnell, H. M. Supported phospholipid bilayers. *Biophys. J.* **47**, 105–113 (1985).

125. Holm, A. *et al.* Langmuir-Blodgett Deposition of Graphene Oxide - Identifying Marangoni Flow as a Process that Fundamentally Limits Deposition Control. *Langmuir* **34**, 9683–9691 (2018).

126. Tae, H., Yang, C. & Cho, N. J. Artificial Cell Membrane Platforms by Solvent-Assisted Lipid Bilayer (SALB) Formation. *Acc. Mater. Res.* **3**, 1272–1284 (2022).

127. Mennicke, U. & Salditt, T. Preparation of solid-supported lipid bilayers by spin-coating. *Langmuir* **18**, 8172–8177 (2002).

128. Bompard, J., Maniti, O., Aboukhachfe, R., Ausserre, D. & Girard-Egrot, A. BALM: Watching the Formation of Tethered Bilayer Lipid Membranes with Submicron Lateral Resolution. *Langmuir* **37**, 9457–9471 (2021).

129. Diamanti, E. *et al.* Gramicidin ion channels in a lipid bilayer supported on polyelectrolyte multilayer films: an electrochemical impedance study. *Soft Matter* **13**, 8922–8929 (2017).

130. Wilkop, T., Xu, D. & Cheng, Q. Characterization of pore formation by streptolysin O on supported lipid membranes by impedance spectroscopy and surface plasmon resonance spectroscopy. *Langmuir* **23**, 1403–1409 (2007).

131. Alfonta, L., Willner, I., Throckmorton, D. J. & Singh, A. K. Electrochemical and quartz crystal microbalance detection of the cholera toxin employing horseradish peroxidase and GM1-functionalized liposomes. *Anal. Chem.* **73**, 5287–5295 (2001).

132. Levental, I., Levental, K. R. & Heberle, F. A. Lipid Rafts: Controversies Resolved, Mysteries Remain. *Trends Cell Biol.* **30**, 341–353 (2020).

133. Hiroshima, M. *et al.* Transient Acceleration of Epidermal Growth Factor Receptor Dynamics Produces Higher-Order Signaling Clusters. *J Mol Biol* **430**, 1386–1401 (2018).

134. Lawrence, J. C., Saslowsky, D. E., Edwardson, J. M. & Henderson, R. M. Real-Time Analysis of the Effects of Cholesterol on Lipid Raft Behavior Using Atomic Force Microscopy. *Biophys. J.* **84**, 1827–1832 (2003).

135. Ziaunys, M. *et al.* Liquid–liquid phase separation of alpha-synuclein increases the structural variability of fibrils formed during amyloid aggregation. *FEBS J.* **291**, 4522–4538 (2024).

136. Ishikawa-Ankerhold, H., Ankerhold, R. & Drummen, G. Fluorescence Recovery After Photobleaching (FRAP). *Encyclopedia of Life Sciences* (2014)

137. Axelrod, D., Koppel, D. E., Schlessinger, J., Elson, E. & Webb, W. W. Mobility measurement by analysis of fluorescence photobleaching recovery kinetics. *Biophys. J.* **16**, 1055–1069 (1976).

138. Reits, E. A. J. & Neefjes, J. J. From fixed to FRAP: Measuring protein mobility and activity in living cells. *Nat. Cell Biol.* **3**, (2001).

Chapter 2: Indium Plasmonic Thin Films as Substrates for SPR Sensing and FDTD Analysis of Oxide-Enhanced UV-SERS

2.1 Introduction

The field of plasmonic surfaces utilized in applications such as surface plasmon resonance (SPR) spectroscopy and surface enhanced Raman spectroscopy (SERS) is currently dominated by gold and silver, with less frequent interest being directed towards other materials such as copper[1], aluminum[2], and indium.[3] Similar to aluminum, indium has higher conduction band electron density and resulting dielectric functions that have been indicated as favorable for plasmonic response across a larger range of wavelengths than seen with noble metal films.[4,5] Indium and its oxides have a long history of implementation across a range of scientific applications, in part due to its plasmonic activity. Some recent examples of indium-containing compound use include catalysis[6] and solar-energy conversion[7,8], as well as a range of gas, biological, and environmental sensors.[9,10] However, indium is very rarely explored in its pure metallic state, with most studies instead focusing on polyatomic indium-containing compounds such as indium tin oxide (ITO)[11–13] and indium nitrides.[14,15] Moreover, these materials are most often reported in complex configurations and/or morphologies meant to push the limits of sensitivity at the cost of accessibility and applicability to other systems. We have previously demonstrated the overlooked potential of comparatively simple aluminum thin films as highly sensitive and accessible substrates for plasmonic sensing.[16] These fundamental explorations of underrepresented materials can add more metallic films to the library of options for plasmonic sensing.

Indium, like aluminum, differs from the "noble" metals in its rapid oxidation upon exposure to air, forming a passivating oxide layer composed primarily of In_2O_3.[17] However, unlike aluminum's insulating Al_2O_3 oxide layer, In_2O_3 is a well-known semiconductive material with predominant usage in the form of doped films such as ITO.[18,19] The natural formation of In_2O_3 on indium films is of particular interest to the field of plasmonic sensing, which has seen a rise as conductive and semiconductive materials in recent years. Some applications explored the addition of graphene, black phosphorus, and MXenes as exterior layers on SPR substrates that serve to improve sensitivity, surface stability, and surface chemistry options.[20–23] However, studies exploring the plasmonic and photonic properties of indium metal and its natively forming oxide layer are limited. Our search of literature only returned one example of the application of In/In_2O_3 thin films for plasmon-related sensing[24], but they largely ignored the role of the native oxide layer. This is likely due to the absence of reliable optical parameters that are vital for computational models such as finite-difference time-domain[25] and Fresnel equation-based modeling.[26,27] It is clear that further characterization and consolidation of both the optical and morphological properties of indium and its oxides is necessary to advance their use in plasmonic applications.

In this work, we employed cleanroom nanofabrication techniques including electron beam physical vapor deposition (EBPVD) and RF magnetron sputtering to fabricate indium and indium oxide thin films with varied thicknesses for plasmonic property characterization. The refractive index responses of the indium films were examined using a series of sucrose solutions and compared to those obtained from the gold films. A suite of surface techniques was employed to obtain structural and optical

information on the metal and oxide layers. Finally, the collected data was utilized to study the effects of the oxide layer on SERS performance. Our results provide new insights that could enable more accurate modeling and optimization of indium substrates in plasmonic sensing applications.

2.2 Experimental Methods

Materials

Indium pellets with purity of 99.99% were purchased for EBPVD from Kurt J. Lesker Company (Jefferson Hills, P.A.). An indium oxide (In_2O_3) target with 99.99% purity and a size of 2.00" diameter x 0.125" thickness was also purchased from Kurt J. Lesker Company for sputtering. Standard 1mm thick glass microscope slides purchased from Fischer Scientific (Pittsburg, PA) were used as the substrate for EBPVD and some sputtering. Other sputtering was performed on <100> undoped silicon wafers purchased from University Wafer (South Boston, M.A.).

Fabrication of In/In_2O_3 and In_2O_3 Thin Films

Glass microscope slides were prepared by first being submerged in boiling piranha solution for 1 hour. They were then rinsed 5 times with large volumes of Milli-Q water before sequential rinsing with ethanol, water, and ethanol. The slides were then dried with nitrogen and stored under vacuum until deposition. Indium films were deposited by an Airco Temescal CV-8 EBPVD system at a voltage of 7.2 kV and current of ~0.015 A. Three different films were prepared using this method; 20 nm and 40 nm indium films deposited directly on glass, as well as 40 nm indium films prepared with a 2 nm chromium

adhesion layer. To heat the indium target and ensure that In_2O_3 was removed from the surface prior to deposition, the target was exposed to the electron beam for 3 minutes before the shutter was opened. To avoid excess oxidation, the slides were allowed to cool inside the chamber for 30 minutes after deposition was complete. The films were stored in air at room temperature (~25 ºC) to allow for the passivating oxide layer to form on the outermost layer of the films.

Sputtering of In_2O_3 films was performed on an AJA ORION 5 Sputtering System (Hingham, MA) using an RF source. Deposition was performed with a substrate temperature of 25 ºC, Ar as the process gas (flow = 10 sccm, pressure = 4.4 mTorr), and a power of 60 W with a 600 second ramp time. Deposition rate was roughly determined with a Veeco Dimension 3100 AFM (Plainview, NY) using a photopatterned Si chip.

Surface Characterization

Scanning electron microscope (SEM) images were collected using a TESCAN Vega3 SBH system (Kohoutovice, CZ) at 5 kV and 30 kx magnification. AFM images in In/In_2O_3 chips were collected with a Horiba LabRam/Aist-NT AFM system (Irvine, CA) and processed using Gwyddion 2.6.1 data analysis software. X-ray photoelectron spectroscopy was conducted by University of California Riverside XPS analytical facility using a Kratos Analytical AXIS ULTRA^{DLD} XPS system (Manchester, UK) with an Al Kα X-ray source. Depth profiles were acquired using an Ar ion beam at 4 keV on an area of 3 mm^2. GIXRD measurements were performed with a Rigaku (Tokyo, JP) Smartlab Automated Multipurpose X-ray Diffractometer. The incident angle (ω) was set to 0.3º for all

measurements, with a speed of 1 °/min, and a step height of 0.05°. Refractive index, extinction coefficient, and thicknesses of sputtered films were determined by spectroscopic ellipsometry using a J. A. Woollam (Lincoln, NE) Alpha-SE ellipsometer. Fitting of ellipsometry data was performed using the transparent Cauchy dispersion model and absorbing film data was collected with a B-spline model.

SPR Analysis

All SPR refractive index sensitivity measurements were performed using a NanoSPR6 (Chicago, I.L.) with a 650 nm GaAs semiconductor laser source. PBS (pH = 7.4) was used as the running buffer with a flow rate of 5 mL/h. The coupling component was a BK-7 prism with a refractive index of ~1.51 for 650 nm light. 100 µL of PBS solutions containing between 0.5% and 10% sucrose (w/v) were injected over the 2/50 nm Cr/Au and 2/40 nm Cr/In chip surfaces and the resonant angle shifts from baseline to peak were monitored and compared.

Computational Modelling of Plasmonic Response

Idealized SPR reflectivity curves were modelled using Winspall software (Resonant Technologies GmbH). All Winspall models were generated using a 650nm p-polarized source laser, coupled with a triangular BK-7 prism (n = 1.5145). Water (n = 1.33) was chosen as the dielectric material contacting the indium films. FDTD simulations were performed using Lumerical FDTD (Ansys, Inc.). To render the indium surface, high resolution AFM images were converted to grayscale, and imported to Blender 4.2 software (Blender Foundation). A 1x1 micron image was subdivided and extruded with UV

mapping. Next, a base was added and the object was converted to a solid body before being exported as an STL. The STL was then imported into the Lumerical FDTD software. The 4 nm oxide layer was added by simply reimporting the same object and shifting it up 4 nm vertically. Electric field strength was measured at different Z-planes under excitation from 532 nm and 382 nm monochromatic planewave sources.

2.3 Results and Discussion

Plasmonic Properties of the Indium Thin Films

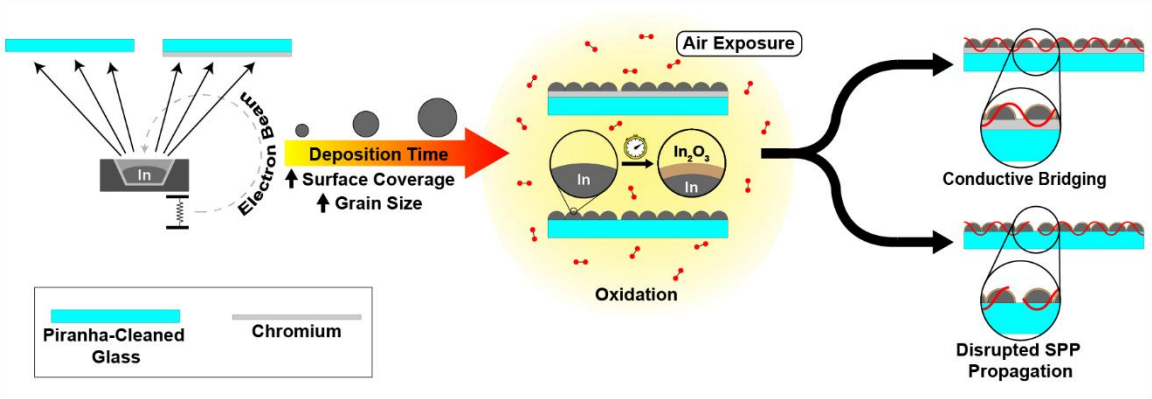

Figure 2.1. Schematic illustration of fabrication of plasmonically active indium thin films using e-beam physical vapor deposition (left). After deposition, a passivating oxide layer quickly forms upon exposure to air (middle). A conductive chromium adhesion layer between the glass and indium layers rescues propagating surface plasmon resonance response from interruptions caused by gaps between indium grains (right).

Preliminary SPR reflectivity modelling under the Kretschmann configuration suggested that an indium film thickness of 20 nm may be optimal for SPR sensing (Figure 2.2). Additionally, a 40 nm film was fabricated for morphological comparison and due to the higher electric field strength demonstrated under typical SPR source wavelengths.[28] EBPVD was selected for its throughput and uniform film deposition, whereas thermal evaporation was avoided due to the risk of residual indium oxide vaporizing in subsequent

runs, potentially contaminating future non-indium depositions.[29] Previous studies have shown that indium thin films deposited by thermal evaporation, electron beam, or sputtering tend to form non-continuous films at room temperature, regardless of vacuum pressure or deposition rate.[24,30] As expected, both the 20 nm and 40 nm films exhibited coalescence of distinct particles, with particle size dependent on the deposition thickness. Refractive index testing with a NanoSPR6 (NanoSPR, Chicago, IL) instrument revealed no response to the sucrose gradient, likely due to gaps between surface structures disrupting the propagation of surface plasmon polaritons. Additionally, high surface roughness creates a large range of matching conditions, which broadens the reflectivity curve dip, thereby complicating minimum angle tracking.[31]

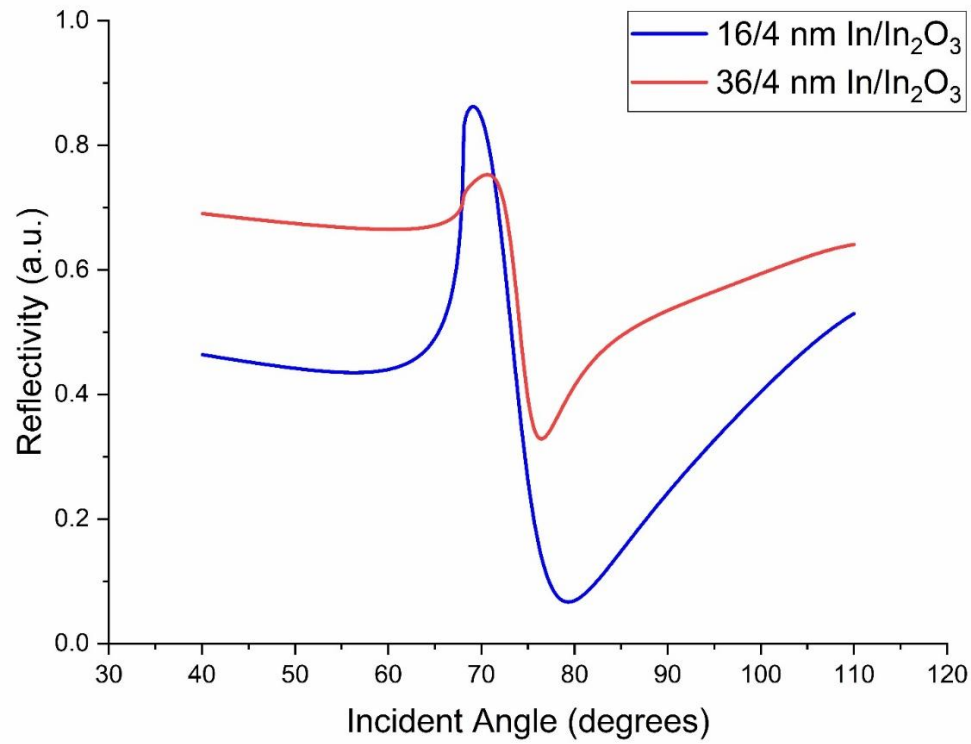

Figure 2.2. Calculated reflectivity curves of 20 nm and 40 nm indium films after oxidation. The 20 nm film was determined to be optimal for SPR and SPRi applications. The 40 nm film still promises a usable plasmonic response while achieving better surface coverage.

To enhance the plasmonic response, we hypothesized that reducing film discontinuities could be an effective strategy. Previous studies have demonstrated that depositing indium thin films on certain metals enhances nucleation and improves film uniformity.[32] Additionally, an underlying metallic layer may serve as a conductive bridge between isolated surface structures. Figure 2.3 shows an SEM image of a 40 nm indium film deposited directly on glass as well as one of a 40 nm film deposited onto a 2 nm chromium base layer. Although the size and spacing of the larger surface structures were similar to those of the film deposited directly on glass, a higher-resolution image of the film on the chromium layer was obtained under the same parameters, indicating improved overall conductivity. Grain size distribution was quantified through image thresholding and particle analysis using ImageJ[33] software (Figure 2.3C). Despite the loss of very small particles (<50 nm) during the thresholding process, the analysis clearly showed a reduction in average particle size with the addition of the chromium base layer. The 2/40 nm Cr/In film was then transferred to a homebuilt SPR imaging (SPRi) instrument[34], where the reflected light intensity from a red LED (~648 nm) was measured as a function of incident angle, revealing a dip attributable to the film's plasmonic activity. This reflectivity curve can then be compared to that of a typical gold film acquired on the same instrument (Figure 2.3D). While the steepness of the reflectivity dip indicates that the indium film will have poor sensitivity for fixed angle SPRi measurement when compared to gold, it appears to be sufficient for SPR instrumentation relying on minimum angle tracking.

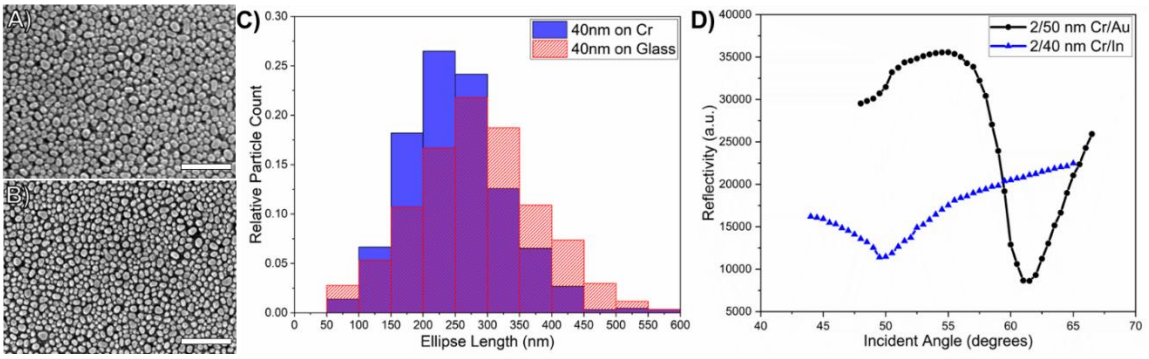

Figure 2.3. SEM images at 30 kx magnification (scale bars = 2 μm) of a 40 nm In film on glass (A) and 2 nm of chromium (B). C) Histogram showing the particle size distributions of the two films. D) Comparison of a 2/40 nm Cr/In film reflectivity spectrum with that of a typical gold SPR film. Curves were acquired on the same SPRi instrument with water (n = 1.33) in the flow cell.

To investigate the effect of film nonuniformity on plasmonic response, surface analysis using X-ray photoelectron spectroscopy (XPS) was performed (Figure 2.4). With a surface composition of approximately 5% Si, significant disruptions to conductivity, and consequently to the propagation of surface plasmon polaritons, was expected in the 20 nm film. Increasing the film thickness to 40 nm reduces the presentation of the sub-indium layer to only approximately 3%. However, these values are likely underestimated, as the presence of an adventitious carbon layer is known to obscure XPS results.[35] XPS depth profiling, involving layer-by-layer ablation of a film cross-section followed by elemental analysis, was also performed to better assess film continuity.[36] Both depth profiles exhibit an initial sharp decline in oxygen composition as the passivating oxide layer is removed, followed by a recovery corresponding to the exposure of underlying SiO_2 (Figure 2.5).

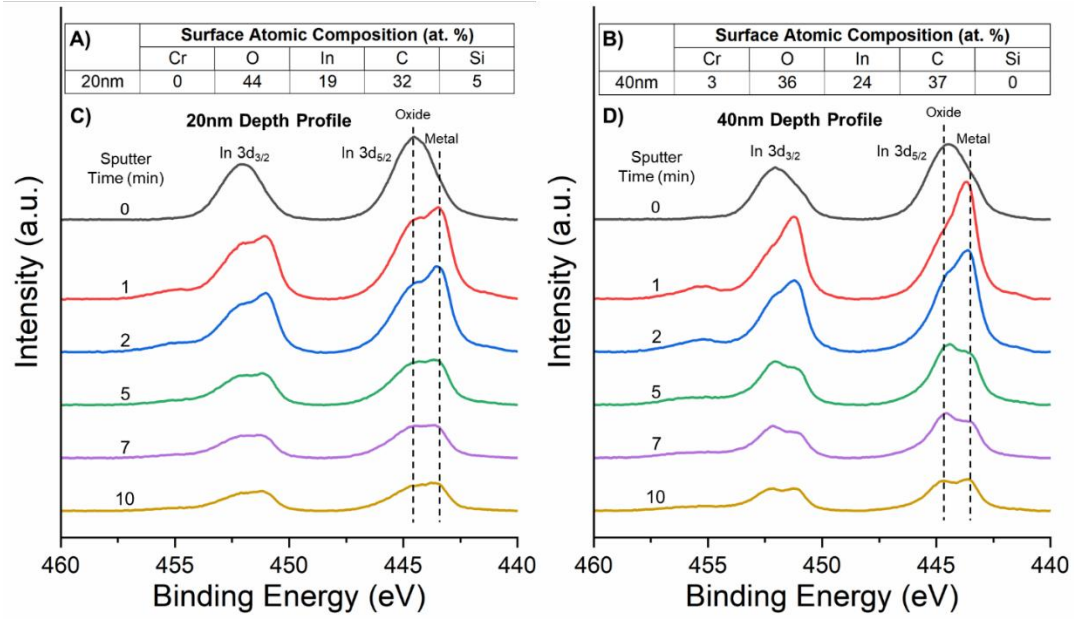

Figure 2.4. Surface XPS analysis comparison of the two films showing a reduction in gaps and complete coverage of non-conductive Si (A and B). The bottom curves show In 3d orbital XPS depth profiles of C) 20 nm In film on glass and D) 2/40 nm Cr/In film.

This trend is inversely correlated with indium content in both films; however, the 40 nm film displays a significantly higher maximum indium atomic percentage, further indicating improved surface coverage. Given the confounding effects of adventitious carbon and differing substrates (Cr vs. SiO_2), a more reliable approach is to compare the intensities of the In 3d peaks (Figures 2.4C & 2.4D). During XPS analysis, the In $3d_{3/2}$ and $3d_{5/2}$ orbitals exhibit binding energy shifts that depend on the chemical state, with an approximate 1 eV difference between metallic indium and In_2O_3.[37] As the surface is etched, differing proportions of the In 3d peaks are observed between the two films. After approximately one minute of etching, by which time the surface In_2O_3 layer is expected to be largely removed, residual In_2O_3 remains due to the core-shell-like morphology of the surface structures. At this point, the metallic indium signal is proportionally stronger in the 40 nm film, indicating greater metallic indium coverage despite the apparent coalescence

observed in SEM images. While 20 nm films were determined as more optimal for sensing applications by simulation, the additional indium coverage and the presence of a chromium base layer appear to be critical for achieving a plasmonic response.

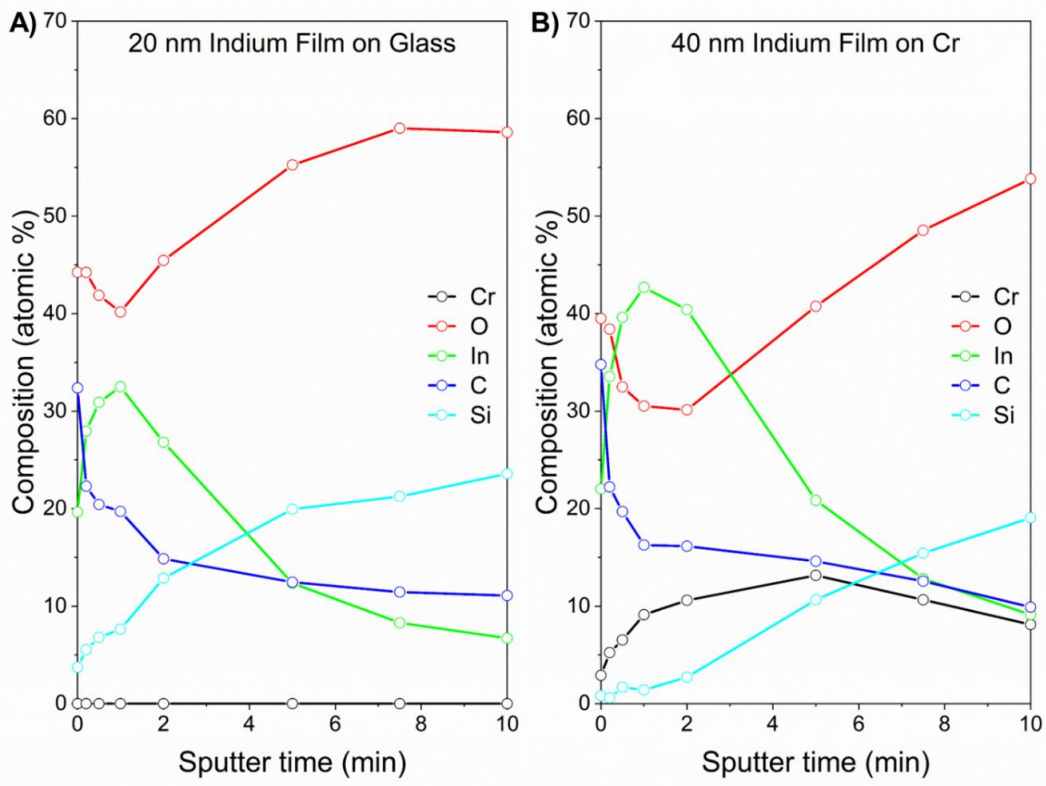

Figure 2.5. Compositional analysis of A) 20 nm In film and B) 2/40 nm Cr/In films during XPS depth profiling.

With the reflectivity curve established for minimum angle tracking, the refractive index response of the indium thin film was evaluated. Sucrose solutions ranging from 0.5–10.0% w/v in water were flowed over the surfaces of the 2/40 nm Cr/In film (Figure 2.6A) and the 2/50 nm Cr/Au film (Figure 2.6B), while shifts in the angle of minimum reflectivity were monitored. To the best of our knowledge, this represents the first demonstration of SPR sensing using an indium thin film, although it does not exhibit any clear advantage over a standard gold film. Plotting the angle shift against the refractive index (Figure 2.6C)

reveals a sensitivity of 44.95°/RIU for the indium film, which is only 77% of that observed for the gold film (58.65°/RIU) (Figure 2.6D) using the same optical setup. Additionally, the indium film exhibits a noisier baseline and a negative shift at low sucrose concentrations. This behavior may be attributed to the hydrophilicity of the oxide layer, which promotes the formation of an ordered hydration layer that can be easily disrupted. General flow-through could introduce slight variations in the local refractive index, contributing to baseline noise. Furthermore, the negative shifts observed at low sucrose concentrations are likely due to pressure fluctuations, which become most apparent when injecting solutions with refractive index differences near or below the limit of detection.

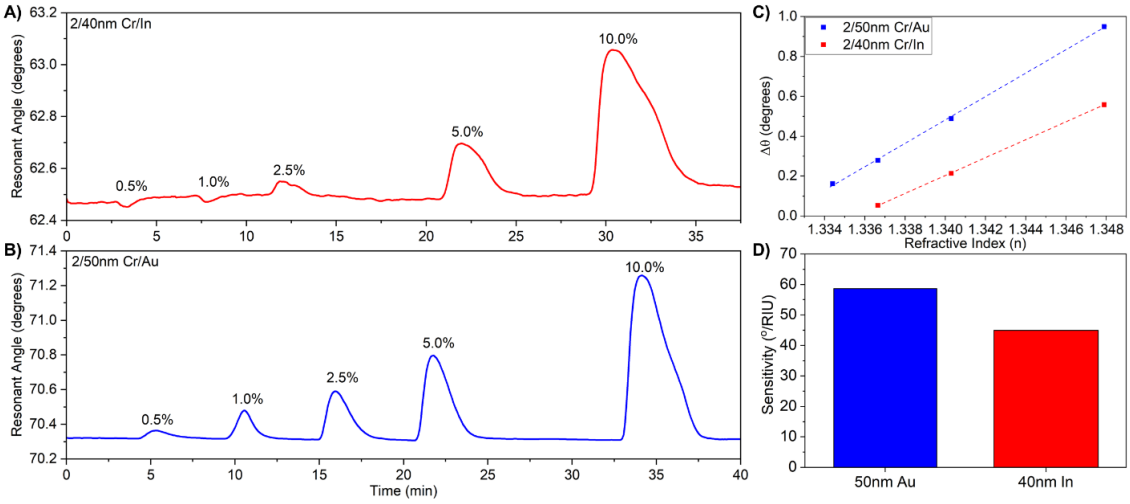

Figure 2.6. A) Refractive index response of 2/40 nm Cr/In film using sucrose solutions (0.5-10.0% w/v). B) Refractive index response of 2/50 nm Cr/Au film using sucrose solutions (0.5-10.0% w/v). C) Comparison of the angle shift response to refractive index change for 2/40 nm Cr/In and 2/50 nm Au. D) Comparison of sensitivity between the two films represented as °/RIU.

Sputtered Films for Determining Oxide Layer Refractive Indices and Informing Film Optimization

While simulating theoretical reflectivity curves to determine the optimal film thicknesses, it became evident that certain characteristics of the passivating oxide layer are inadequately represented in the literature. The thickness of the oxide layer is well established to depend on the temperature and composition of the local atmosphere during formation, typically reaching approximately 4 nm at 25°C in air.[38] The electrical and optical properties of In_2O_3 thin films deposited directly from In_2O_3 sources are highly dependent on their crystallinity, which in turn is influenced by the deposition temperature.[39,40] However, as a naturally forming oxide layer, comprehensive optical constant data across a broad spectral range remains unavailable. The combination of multilayered, rough film morphology and the thin native oxide layer makes it, to our knowledge, impractical to obtain this information directly from the films. Alternatively, we have previously demonstrated that optical constants from amorphous oxide films exhibiting bulk-like properties[41] (e.g., >40 nm for Al_2O_3) can be reliably used to simulate the plasmonic dip of oxidizing metal films.[16]

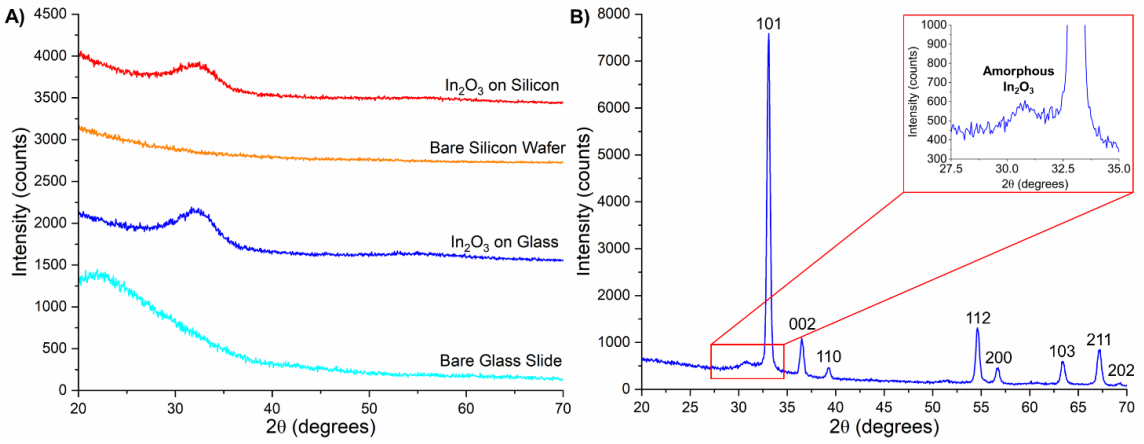

Figure 2.7. A) GIXRD scans of ~26 nm In_2O_3 films sputtered on silicon wafers and glass slides compared to the bare substrates. B) GIXRD scan of 40 nm In film deposited on a glass slide. All ordered crystalline peaks correspond to metallic indium, but a broad amorphous peak corresponding to those observed on the sputtered films is also observed (top right).

To obtain this information, In_2O_3 films were deposited by RF magnetron sputtering with a 99.99% purity In_2O_3 source at estimated thicknesses of 4 nm, 30 nm, 50 nm, and 200 nm. These films were deposited on <100> silicon wafers and amorphous glass slides to determine the effects of substrate crystallinity and composition on the formed films. To verify the suitability of the sputtered films as analogues for the native oxide layer, glancing incident X-ray diffraction (GIXRD) was performed on both 30 nm sputtered films (Figure 2.7A) and a 40 nm In/In_2O_3 film (Figure 2.7B). The sputtered films exhibited completely amorphous crystallinity, regardless of the substrate, with a broad peak observed between 28-36°. A similarly positioned amorphous peak is also observed on the 40 nm In/In_2O_3 film, though it is less pronounced due to the comparatively thin oxide layer. This peak is absent in unoxidized indium films,[42] and all other visible peaks correspond to metallic indium, indicating that the observed peak is representative of amorphous In_2O_3.

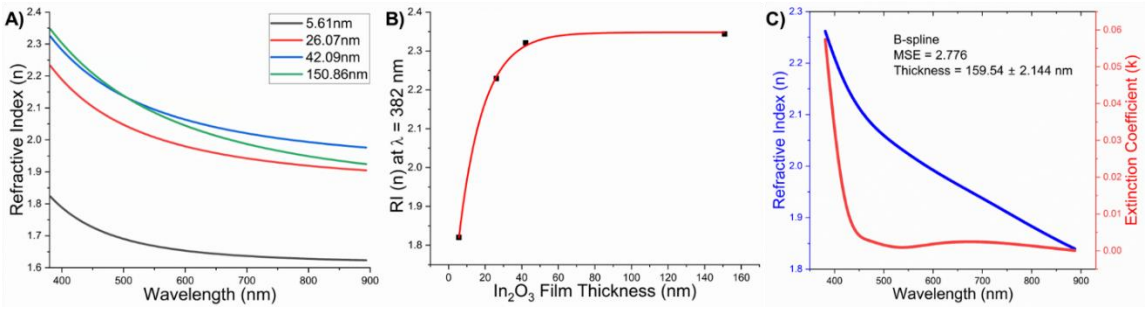

Figure 2.8. A) Refractive index vs. wavelength for sputtered In_2O_3 films at varying thicknesses and SE-calculated thicknesses. The data was collected by spectroscopic ellipsometry with a transparent film model ($k = 0$). B) Refractive index at $\lambda = 382$ nm vs. film thickness plot showing the transition from bulk to thin film properties around 40 nm. C) Real (n) and imaginary (k) refractive index vs. wavelength for the ~150 nm In_2O_3 film collected by ellipsometry with an absorbing film model.

Given that both the sputtered and natively formed In_2O_3 exhibit similar crystallinity, the sputtered films were deemed acceptable analogues for optical analysis. To determine the thickness at which bulk-like optical properties emerge, spectroscopic ellipsometry (SE) measurements of the refractive index (n) of the sputtered In_2O_3 films were collected over the 382–900 nm spectral range. Due to the low absorbance of light in this wavelength range, extinction coefficients (k) could not be determined for any film except the thickest one. For this reason, the ellipsometry data was processed and compared using a Cauchy transparent film model in which $k = 0$ (Figure 2.8A). For the thicker film (~151 nm), the absorption becomes significant enough that the mean squared error (MSE) becomes substantial, causing the curve to deviate from the trend (Table 2.1). Nevertheless, when the refractive index at a particular wavelength for each film is plotted against film thickness, a plateau representing the transition to bulk optical properties can be observed beginning around 40 nm (Figure 2.8B). The transition occurs as the number of voids approaches zero and the film becomes continuous.[43]

Estimated Thickness @ Deposition	Tabulated Thickness	A	B	C	MSE
4 nm	5.61 ± 0.023 nm	1.612 ± 0.0143	0.00420 ± 0.005552	0.00384 ± 0.0006297	0.814
30 nm	26.07± 0.020 nm	1.850 ± 0.0173	0.04077 ± 0.007859	0.00214 ± 0.0008455	3.87
50 nm	42.09 ± 0.131 nm	1.908 ± 0.0513	0.05297 ± 0.021138	0.00108 ± 0.002100	35.187
200 nm	150.86 ± 0.676 nm	1.822 ± 0.0107	0.08319 ± 0.006599	-0.00100 ± 0.00077780	46.651

Table 2.1. Fit variables and mean squared errors for ellipsometry on sputtered In_2O_3 films using a transparent Cauchy model.

Though the native oxide layer of indium is only ~4 nm in thickness, the void percentage is determined by the continuity of the underlying metal, making the bulk refractive index values appropriate for computational modelling and optimization of In/In_2O_3 films. As extinction is a highly relevant parameter for these models, the use of an SE absorbing model of the bulk material becomes necessary. An absorbing B-spline model SE of the ~150 nm In_2O_3 film (Figure 2.8C) revealed a very low extinction coefficient across all but the lowest wavelengths of the visible range. Given the low extinction and the thinness of the oxide layer, its effect on the SPR response at typical wavelengths (~650 nm) is expected to be minimal (Figure 2.9). However, in other types of plasmonic applications such as UV-SPR, the presence of the oxide is likely to have a more significant impact and cannot be as simply neglected.

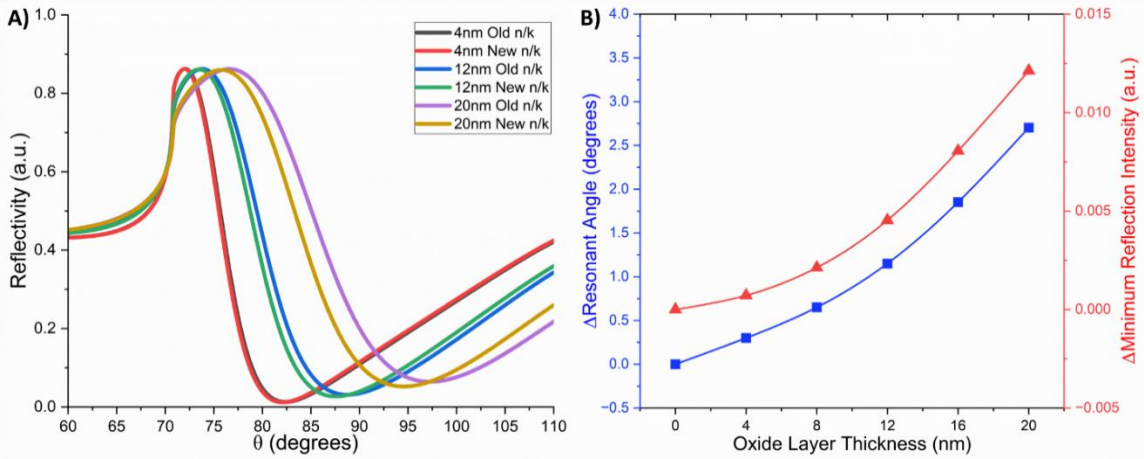

Figure 2.9. Comparison of SPR reflectivity curve models utilizing best available refractive index values from literature[44] at 650 nm (n = ~2.10, k = ~0.009) and values we acquired experimentally (n = 1.964, k = 0.0024). The model uses an optimized metallic indium thickness at 16 nm, with varying oxide thicknesses to illustrate the increasing importance of accurate optical constants as film thickness increases.

Theoretical Assessment of In/In_2O_3 Films as SERS-Active Substrates

Though not as commonly utilized for plasmonic sensing as noble metals, so-called "poor" metals such as indium and aluminum carry qualities that make them attractive alternative substrates. Arising from their high plasma frequencies (ω_p) and resulting quasi-static surface plasmon frequency (ω_s), both indium and aluminum are able to achieve plasmonic coupling with higher-frequency radiation.[4] This provides access to an expanded spectral range of plasmonic response, leading to widespread use in plasmonic techniques utilizing UV illumination. Between the two metals, aluminum is more widely reported, likely owing to its better understood optical and chemical properties. With further investigation of these properties, such as has been provided in this work, indium implementation may begin to rival aluminum more closely.

Following the characterization of the In_2O_3 films and the determination that the surface was not ideal for SPR in its current state, we sought to apply this information to investigate other plasmonic sensing modalities. The most apparent alternative is SERS, which relies on sub-excitation-wavelength sized nanostructures that produce localized SPR. While gold and silver nanostructures are the prototypical SERS substrates, an immense variety of shapes, sizes, and materials have also been successfully employed for SERS sensing.[45] In/In_2O_3 films may prove to be effective for Raman enhancement, particularly in the UV-range.[46–48] Beyond the optical qualities, the highly hydrophilic nature of the exterior oxide layer may also promote distinct analyte packing compared to hydrophobic substrates such as gold, potentially giving rise to unique chemical enhancement mechanisms.[49] While aluminum carries the same qualities outlined above, indium may show some unique effects, owing primarily its differing oxide layer and surface morphology. The oxide layer of indium is thicker (~4 nm vs ~3 nm), conductive, and less prone to corrosion.[50,51] Additionally, while most SERS substrates rely on complex lithography or chemical methods to create nanostructures, In/In_2O_3 films can be fabricated rapidly and reproducibly through single-step deposition.

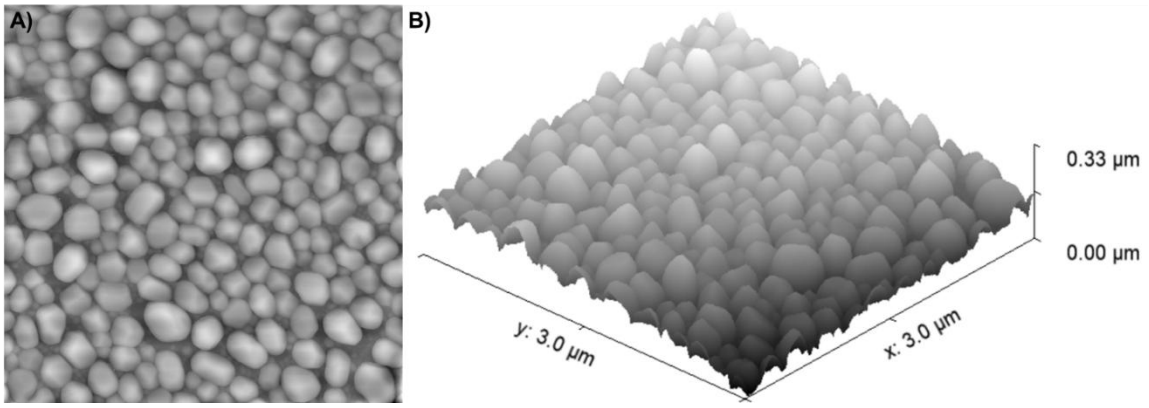

Figure 2.10. A) 2D AFM and B) 3D image of a 3x3 µm section of a 40 nm indium film on glass with a resolution of 1024x1024 pixels. A 1x1 µm section of this image was used for FDTD simulations.

SERS enhancement of adenine on 25nm indium thin films was previously explored with FDTD computational methods by Kumamoto et al.[24] However, the modeled surface was simplified by excluding the oxide layer, flattening surface structures, and assigning a single height to all features. To more accurately represent our surface, a 3D model was generated by converting an atomic force microscopy (AFM) image (Figure 2.10) into a stereolithography (STL) file (Figure 2.11A). This file was then imported into Lumerical FDTD (Ansys, Inc) software and placed on a 1x1x1 µm glass base (Figure 2.11B) and was then used to determine the electromagnetic field strength under illumination from a monochromatic plane wave sources at various wavelengths. Figure 2.11C shows an example of the electromagnetic field enhancement at a particular Z-plane under 382nm excitation, with the hotspots visible along the surface of the structures. The outputted heatmap reports as *E*, which is equivalent to $\frac{E_{\text{local}}}{E_{\text{incident}}}$, or the electromagnetic field amplitude at a point divided by the field amplitude of the incident light.

The enhancement factor (EF) can be roughly determined using the following:

$$\mathrm{EF} = |E(\omega)|^2 |E(\omega')|^2 \tag{2.1}$$

With ω equal to the frequency of incident light and ω' equal to the Stokes-shifted frequency, the equation can be simplified by equation 2.2:

$$|E(\omega)| \approx |E(\omega')| \tag{2.2}$$

This assumption then provides the following:

$$\mathrm{EF} \approx |E|^4 \tag{2.3}$$

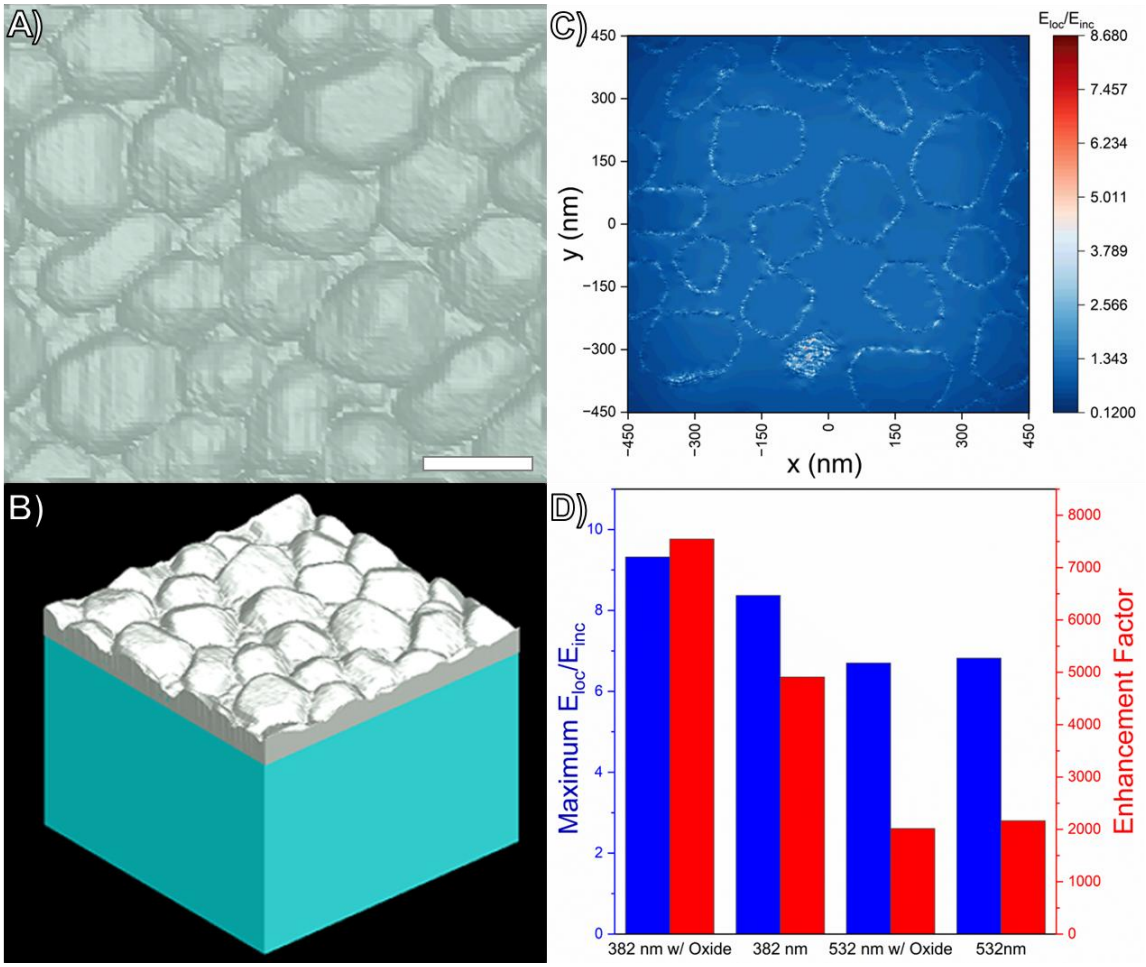

Figure 2.11. A) Top down image of 40 nm In/In_2O_3 films obtained by AFM (scale bar = 200 nm) that was converted to an STL. B) Film model imported to FDTD software and placed on a 1x1x1 µm glass cube. C) Example of a frequency-domain field profile of a Z-plane on the oxidized film under 382 nm excitation. D) Maximum E_{loc}/E_{inc} for oxidized and unoxidized films under 382 nm and 532 nm excitement and the corresponding EF determined by the EF ≈ $|E|^4$ law. The oxide positively effects the enhancement under near-UV excitation, but not at 532 nm.

The EF ≈ $|E|^4$ "law" is a well-established method for estimating and comparing the enhancement of SERS substrates.[52] This method was used to evaluate the role of the oxide layer in the SERS effect by simulating the film at two excitation wavelengths (532 nm and 382 nm), both with and without a 4 nm oxide layer. The 532 nm source was chosen due to its ubiquitous availability in Raman spectroscopy instruments, while the 382 nm source was chosen as it was the smallest wavelength (deepest into the UV) that In_2O_3 optical constants had been obtained in our SE data set. The maximum observed $\frac{E_{\text{local}}}{E_{\text{incident}}}$ value for each film under the different excitation conditions was obtained by manually searching through each Z-plane of the film (Figure 2.12), and these values were plotted along with their corresponding EF (Figure 2.11D). As expected, substantially higher EF was observed under the 382 nm incident light regardless of oxide presence. However, the oxide layer only significantly affected the EF under 382 nm illumination, with a >50% increase from 4.9 x10^3 to 7.5 x 10^3 observed.

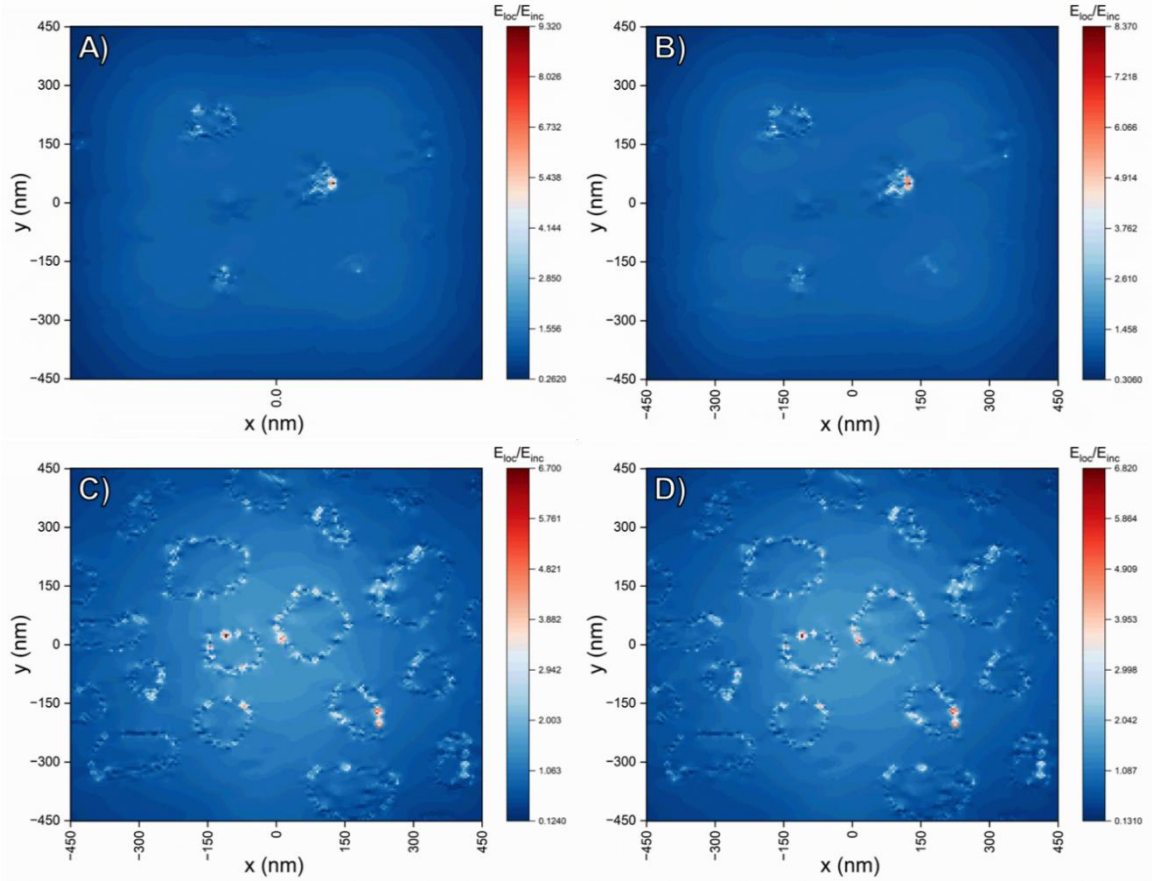

Figure 2.12. Heatmaps of the z-planes where the highest observed $\frac{E_{\text{local}}}{E_{\text{incident}}}$ was found for each simulated film. A) 382 nm excitation with oxide. B) 382 nm excitation without oxide. C) 532 nm excitation with oxide. D) 532 nm excitation without oxide.

2.4 Conclusion

In this work, an experimental and theoretical investigation of the plasmonic properties and applications of indium thin films is presented. Films deposited on glass at thicknesses of 20 nm and 40 nm produced by EBPVD do not show a propagating SPR response under 650 nm illumination despite theoretical backing. SEM and XPS analyses suggest this incongruity stems from the rough, discontinuous film morphology caused by droplet coalescence during deposition. The addition of a conductive chromium base layer to the 40 nm indium film partially restored the plasmonic response, but it did not demonstrate any clear advantage over conventional gold SPR films. To fabricate indium thin films more suitable for spectroscopic SPR applications, these challenges must be addressed through specialized deposition techniques or equipment. In future work, film uniformity may be improved during thermal or electron beam evaporation by depositing under very low vacuum and high deposition rates.[53] Alternatively, employing low-temperature deposition on a liquid nitrogen cooled sample stage could yield some improvement in film uniformity, though subsequent high temperature annealing while sandwiched between carbon layers is required to achieve a more highly uniform film.[30] While these methods could theoretically generate a film more appropriate for SPR analysis, increased sample handling and switching to sputter deposition present downsides in the areas of potential contamination as well as fabrication throughput and consistency.

During our investigation of indium thin films as SPR substrates, it became apparent that the crystallinity and optical properties of In_2O_3 as a passivating oxide layer were neither well-understood nor readily accessible. The oxide layer was subsequently investigated due to its potential impact on the performance of both indium films and nanoparticles. The crystallinity of sputtered and passivating In_2O_3 films was examined and compared using GIXRD, which confirmed their amorphous morphology. With the sputtered films verified as structural analogues to the passivating oxide, optical constants were obtained and incorporated into computational FDTD simulations to assess the In/In_2O_3 system for SERS applications. Results from this investigation revealed that the oxide layer plays a significant role in the enhancement effect, particularly at lower wavelengths, where a greater than 50% increase in enhancement was observed under 382 nm illumination. Due to the limitation of SE-derived optical constants to the near-UV range, assessment of potential enhancement from the oxide layer in the deep-UV was not possible. However, we speculate that the effect could be significantly greater at these shorter wavelengths. While further investigation is needed to obtain accurate optical constants in this wavelength range, these results have provided clear evidence for the importance of oxide layer inclusion for accurate simulation-based determination of UV-SERS signal enhancement for both thin film and nanoparticle substrates.

2.5 References

1. Stebunov, Y. V, Yakubovsky, D. I., Fedyanin, D. Y., Arsenin, A. V & Volkov, V. S. Superior Sensitivity of Copper-Based Plasmonic Biosensors. *Langmuir* **34**, 4681–4687 (2018).

2. Gérard, D. & Gray, S. K. Aluminium plasmonics. *J. Phys. D:Appl Phys.* **48**, 184001 (2015).

3. Valenti, M. *et al.* Optical Characterization of Plasmonic Indium Lattices Fabricated via Electrochemical Deposition. *ACS Appl. Opt. Mater.* **1**, 753–758 (2023).

4. Zeman, E. J. & Schatz, G. C. An accurate electromagnetic theory study of surface enhancement factors for silver, gold, copper, lithium, sodium, aluminum, gallium, indium, zinc, and cadmium. *J. Phys. Chem.* **91**, 634–643 (1987).

5. McMahon, J. M., Schatz, G. C. & Gray, S. K. Plasmonics in the ultraviolet with the poor metals Al, Ga, In, Sn, Tl, Pb, and Bi. *Phys. Chem. Chem. Phys.* **15**, 5415–5423 (2013).

6. Li, J., Zhu, M. & Han, Y. Recent Advances in Electrochemical CO Reduction on Indium-Based Catalysts. *ChemCatChem* **13**, 514–531 (2020).

7. Biswas, P. K. & Das, N. Soft chemistry based sponge-like indium tin oxide (ITO) — a prospective component of photoanode for solar cell application. *Front. Mater. Sci* **9**, 126–131 (2015).

8. Ramanujam, J. & Singh, U. P. Copper indium gallium selenide based solar cells – a review. *Energy Environ. Sci.* **10**, 1306–1319 (2017).

9. Ali, M. *et al.* NOx sensing properties of In2O3 thin films grown by MOCVD. *Sens. Actuators, B* **129**, 467–472 (2008).

10. Silah, H., Erkmen, C., Demir, E. & Uslu, B. Modified indium tin oxide electrodes: Electrochemical applications in pharmaceutical, biological, environmental and food analysis. *TrAC, Trends Anal. Chem.* **141**, 116289 (2021).

11. D'apuzzo, F. *et al.* Mid-Infrared Plasmonic Excitation in Indium Tin Oxide Microhole Arrays. *ACS Photonics* **5**, 2431–2436 (2018).

12. Xi, M. & Reinhard, B. M. Localized Surface Plasmon Coupling between Mid-IR-Resonant ITO Nanocrystals. *J. Phys. Chem. C* **122**, 5698–5704 (2018).

13. Liu, C. *et al.* Surface plasmon resonance (SPR) infrared sensor based on D-shape photonic crystal fibers with ITO coatings. *Opt. Commun.* **464**, 125496 (2020).

14. Palomaki, P. K., Miller, E. M. & Neale, N. R. Control of plasmonic and interband transitions in colloidal indium nitride nanocrystals. *J. Am. Chem. Soc.* **135**, 14142–14150 (2013).

15. Poliani, E. *et al.* Strong Near-Field Light–Matter Interaction in Plasmon-Resonant Tip-Enhanced Raman Scattering in Indium Nitride. *J. Phys. Chem. C* **124**, 28178–28185 (2020).

16. Lambert, A. S., Valiulis, S. N., Malinick, A. S., Tanabe, I. & Cheng, Q. Plasmonic Biosensing with Aluminum Thin Films under the Kretschmann Configuration. *Anal. Chem.* **92**, 8654–8659 (2020).

17. Eldridge, J. M., Van Der Meulen, Y. J. & Dong, D. W. Analysis of Ultrathin Oxide Growth on Indium. *Thin Solid Films* **12**, 447–451 (1972).

18. Choi, C.-H. *et al.* Fabrication of high-performance, low-temperature solution processed amorphous indium oxide thin-film transistors using a volatile nitrate precursor. *J. Mater. Chem. C* **3**, 854–860 (2015).

19. Bierwagen, O. Indium oxide—a transparent, wide-band gap semiconductor for (opto)electronic applications. *Semicond. Sci. Technol.* **30**, 24001 (2015).

20. Singh, S. *et al.* 2D Nanomaterial-Based Surface Plasmon Resonance Sensors for Biosensing Applications. *Micromachines (Basel)* **11**, 779 (2020).

21. Wu, L. *et al.* Sensitivity enhancement by using few-layer black phosphorus-graphene/TMDCs heterostructure in surface plasmon resonance biochemical sensor. *Sens. Actuators, B* **249**, 542–548 (2017).

22. Pandey, A. K. Graphene–Ti3C2Tx MXene hybrid nanostructure: a promising material for sensitivity enhancement in plasmonic sensor. *Appl. Phys. A:Mater. Sci. Processs.* **127**, 78 (2021).

23. Kumar, R., Pal, S., Verma, A., Prajapati, Y. K. & Saini, J. P. Effect of silicon on sensitivity of SPR biosensor using hybrid nanostructure of black phosphorus and MXene. *Superlattices Microstruct.* **145**, 106591 (2020).

24. Kumamoto, Y. *et al.* Indium for Deep-Ultraviolet Surface-Enhanced Resonance Raman Scattering. *ACS Photonics* **1**, 598–603 (2014).

25. Zeng, Z., Liu, Y. & Wei, J. Recent advances in surface-enhanced raman spectroscopy (SERS): Finite-difference time-domain (FDTD) method for SERS and sensing applications. *TrAC, Trends Anal. Chem.* **75**, 162–173 (2016).

26. Gomes, J. C. M. & Oliveira, L. C. A novel simulador for agile and graphical modeling of surface plasmon resonance based sensors. *Sci. Rep.* **13**, 18920 (2023).

27. Ji, L., Chen, Y. & Yuan, Y. J. Investigation of surface plasmon resonance phenomena by finite element analysis and Fresnel calculation. *Sens. Actuators, B* **198**, 82–86 (2014).

28. Ross, M. B. & Schatz, G. C. Aluminum and Indium Plasmonic Nanoantennas in the Ultraviolet. *J. Phys. Chem. C* **118**, 12506–12514 (2014).

29. Company, K. J. L. Indium In Evaporation Process Notes. vol. 2024 https://www.lesker.com/newweb/deposition_materials/deposition-materials-notes.cfm?pgid=in1 (2015).

30. Boulesteix, C., Devant, G., Marraud, A. & Rateau, R. Structure and Recrystallization of Indium Thin Film. *J. Vac. Sci. Technol.* **6**, 780–783 (1969).

31. Treebupachatsakul, T., Shinnakerdchoke, S. & Pechprasarn, S. Analysis of Effects of Surface Roughness on Sensing Performance of Surface Plasmon Resonance Detection for Refractive Index Sensing Application. *Sensors* **21**, 6164 (2021).

32. Bertran, E., Morenza, J. L., Esteve, J. & Varela, M. Indium Thin Films on Metal-Coated Substrates. *Thin Solid Films* **129**, 103–109 (1985).

33. Schneider, C. A., Rasband, W. S. & Eliceiri, K. W. NIH Image to ImageJ: 25 years of image analysis. *Nat. Methods* **9**, 671–675 (2012).

34. Wilkop, T., Wang, Z. & Cheng, Q. Analysis of μ-Contact Printed Protein Patterns by SPR Imaging with a LED Light Source. *Langmuir* **20**, 11141–11148 (2004).

35. Grey, L. H., Nie, H.-Y. & Biesinger, M. C. Defining the nature of adventitious carbon and improving its merit as a charge correction reference for XPS. *Appl. Surf. Sci.* **653**, 159319 (2024).

36. Oswald, S. & Reiche, R. Binding state information from XPS depth profiling: capabilities and limits. *Appl. Surf. Sci.* **179**, 307–315 (2001).

37. Zatsepin, D. A. *et al.* Bulk In2O3 crystals grown by chemical vapour transport: a combination of XPS and DFT studies. *J. Mater. Sci.:Mater. Electron.* **30**, 18753–18758 (2019).

38. Schoeller, H. & Cho, J. Oxidation and reduction behavior of pure indium. *J. Mater. Res.* **24**, 386–393 (2011).

39. Buchholz, D. B. *et al.* The Structure and Properties of Amorphous Indium Oxide. *Chem. Mater.* **26**, 5401–5411 (2014).

40. Buchholz, D. B., Zeng, L., Bedzyk, M. J. & Chang, R. P. H. Differences between amorphous indium oxide thin films. *Prog. Nat. Sci.:Mater Int.* **23**, 475–480 (2013).

41. Boidin, R., Halenkovič, T., Nazabal, V., Beneš, L. & Němec, P. Pulsed laser deposited alumina thin films. *Ceram. Int.* **42**, 1177–1182 (2016).

42. Bartlett, P. N. *et al.* Non-aqueous electrodeposition of p-block metals and metalloids from halometallate salts. *RSC Adv.* **3**, 15645 (2013).

43. Nakahara, S. Microporosity in thin films. *Thin Solid Films* **64**, 149–161 (1979).

44. Szczyrbowski, J., Dietrich, A. & Hoffmann, H. Optical Properties of RF-Sputtered Indium Oxide Films. *physica status solidi (a)* **69**, 217–226 (1982).

45. Sharma, B., Frontiera, R. R., Henry, A.-I., Ringe, E. & Van Duyne, R. P. SERS: Materials, applications, and the future. *Mater. Today* **15**, 16–25 (2012).

46. Zhang, J., Yan, Y., Miao, P. & Cai, J. Fabrication of gold-coated PDMS surfaces with arrayed triangular micro/nanopyramids for use as SERS substrates. *Beilstein J. Nanotechnol.* **8**, 2271–2282 (2017).

47. Yang, Y. *et al.* Controlled fabrication of silver nanoneedles array for SERS and their application in rapid detection of narcotics. *Nanoscale* **4**, 2663–2669 (2012).

48. Ji, W., Zhao, B. & Ozaki, Y. Semiconductor materials in analytical applications of surface-enhanced Raman scattering. *J. Raman Spectrosc.* **47**, 51–58 (2016).

49. Bell, S. E. J. *et al.* Towards Reliable and Quantitative Surface-Enhanced Raman Scattering (SERS): From Key Parameters to Good Analytical Practice. *Angew. Chem., Int. Ed. Engl.* **59**, 5454–5462 (2020).

50. Jeurgens, L. P. H., Sloof, W. G., Tichelaar, F. D. & Mittemeijer, E. J. Thermodynamic stability of amorphous oxide films on metals: Application to aluminum oxide films on aluminum substrates. *Phys. Rev. B.* **62**, 4707–4719 (2000).

51. Folcher, G. H., Cachet, H., Froment, M. & Bruneaux, J. Anodic corrosion of indium tin oxide films induced by the electrochemical oxidation of chlorides. *Thin Solid Films* **301**, 242–248 (1997).

52. Le Ru, E. C. & Etchegoin, P. G. Rigorous justification of the |E|4 enhancement factor in Surface Enhanced Raman Spectroscopy. *Chem. Phys. Lett.* **423**, 63–66 (2006).

53. He, C. *et al.* Sensitive Aluminum SPR Sensors Prepared by Thermal Evaporation Deposition. *ACS Omega* **8**, 43188–43196 (2023).

Chapter 3: Methodological Considerations and Optimizations for Surface Plasmon Resonance Analysis of Monovalent, Bivalent, and Covalent Binding Interactions

3.1 Introduction

Over the past three and a half decades, surface plasmon resonance has established itself as a critical technology for characterization of biomolecular interactions.[1,2] The substantial adoption and importance of SPR in drug development can be accounted to its label-free, real-time, and multiplexable measurements of both binding kinetics and affinity, thereby making it the gold standard in the field. Despite its widespread adoption and the many advantages it holds over alternative methods such as isothermal titration calorimetry (ITC),[3] reliable collection and interpretation of SPR data can prove more challenging as they are highly dependent on proper experimental design, material quality, and choice of analytical model.[4] Furthermore, as the field of drug development continues to advance, new drugs demonstrating more complex binding behaviors have necessitated similar advancements in SPR methodology, both experimentally and computationally.

Biomolecular interactions are frequently more complex than the traditional 1:1 Langmuir binding model would reflect, with from vastly different behaviors and drug effectiveness resulting from multivalency, avidity effects, analyte rebinding, and irreversible covalent binding.[5,6] While the kinetics of monovalent interactions can be easily identified with traditional biosensing techniques and models, higher-order interactions can obscure kinetic rate constants by introducing coupling between binding events.[7] Furthermore, as covalent inhibitors are being increasingly recognized as an important and powerful class of drugs, there has been increasing need for systems that can quickly and

accurately quantify and characterize the rate of covalent binding events.[8] Because these covalent binding events are typically secondary events that occur after induced proximity by a primary affinity between drug and protein, identifying the intrinsic rate constants can prove challenging to identify, particular in a manner that is high-throughput.[9–11]

The focus of this chapter is on both the experimental and analytical considerations of performing robust SPR analysis, and how those considerations change along with the valency of the analyte. Particular emphasis is placed on the choice of immobilization method, but the influence of many other factors including flow-rate, analyte contact times, immobilization levels, flow-cell temperature, buffer composition, and data analysis on SPR data quality are reported. Through systematic improvements, systems of increasing complexity are explored, with important pitfalls and data analysis choices identified. Through this process, the goal of this chapter is to identify the unique challenges of each binding modality and provide guidance in the development and interpretation of SPR assays that are both reliable and biologically relevant.

3.2 Experimental Methods

Materials and Reagents

A 6x hist-tagged protein (ligand) and all but one analyte for testing were synthesized and/or provided by the Pellecchia research group in the Biomedical Sciences Department at UC Riverside. In total, five of the provided analytes were synthesized by the Pellecchia group and one (monovalent analyte #3, MA3) was purchased. The ligand stock was provided at 207 μM in 1x TBS. All analyte stocks were provided at millimolar concentrations in

DMSO. All SPR measurements were conducted using a Biacore 1K SPR system (Cytiva, Uppsala, SE) with Biacore Insight Control Software Version 6.0.7.1750. Data fitting and analysis was performed using Biacore Insight Evaluation Software Version 6.0.7.1750. Sensor chip NTA, NTA reagent kits, and a Biacore Cap-Tag Capture Kit were purchased from Cytiva.

Multicycle Kinetics on Sensor Chip NTA

All measurements were conducted on a Series S Sensor Chip NTA (Cytiva) with a data collection rate of 10 Hz and a flow cell temperature of 25 ^{o}C. Ligand was diluted from the stock to 100 nM in the running buffer composed of 1x PBS (pH = 7.4) with 0.5% DMSO and 0.05% tween-20, freshly prepared and filtered through a 0.22 µm aPES vacuum filter. Analytes were diluted in running buffer down to 125 nM before working concentrations were prepared by serial dilution (1:5) in running buffer down to the lowest concentration of 0.2 nM.

Multicycle kinetic measurements were conducted at a flow rate of 50 µL/min, with a contact time of 120 seconds and a dissociation time of 180 seconds. Ligand capture levels were targeted to achieve a maximal response (R_{max}) of approximately 20 RUs at steady state. Prior to an experiment the surface was prepared with three 30 second injections of 350 mM EDTA at a flow rate of 30 µL/min. Nickel was captured on the NTA groups with a 60 second injection of 0.5 mM $NiCl_2$ at a flow rate of 10 µL/min. After washing the flow system with 3.5 mM EDTA in running buffer, the ligand was captured the appropriate level at a flow rate of 10 µL/min. Immediately after capture, the analyte would be injected

followed by regeneration with 350 mM EDTA as outlined above. This process was repeated for each analyte concentration as well as with buffer blanks for use in double-reference subtraction. Data was fitted to determine kinetic constants using a 1:1 (Langmuir) binding model.

Covalent Capture and Single cycle Kinetics on Sensor Chip NTA

To capture the ligand covalently on a Series S Sensor Chip NTA (Cytiva), the surface was first prepared with 350 mM EDTA followed by capture of nickel as outlined above. However, before injection of the 100 nM ligand solution, the surface was activated with a 7-minute injection of a 1:1 mixture of 0.1 M N-hydroxysuccinimide (NHS) and 0.4 M 1-ethyl-3-(3-dimethylaminopropyl)carbodiimide (EDC). Ligand was captured to target an analyte injection R_{max} of approximately 20 RUs. Single cycle kinetics were then conducted with a 120 second contact time and 1800 second dissociation time at a flow rate of 50 µL/min and a flow cell temperature of 25 ºC. The running buffer was 1x HEPES-buffered saline (HBS) with 0.5% DMSO, 0.05% tween-20, and 50 µM EDTA. The analytes tested using this method include bivalent analytes 1 and 2. Data was collected at a sampling rate of 10 Hz and was double reference subtracted before being fitted using a bivalent analyte model.

Protein Functionalization, Capture, and Kinetics with Cap-Tag Capture Kit

The ligand was conjugated to the cap-tag oligomers using standard procedures recommended by Cytiva, starting with a ligand solution at a concentration of 1 mg/mL. Due to the lower-than-recommended molecular weight of the protein, bicinchoninic acid

(BCA) assays were conducted using a Pierce™ BCA Protein Assay Kit to determine protein yield after each column purification step. Ligand activator and cap-tag solution volumes were adjusted to account for lost protein. After cap-tagging and capture scouting, a 1:160 dilution in running buffer was selected for use with bivalent analytes and a 1:80 dilution was selected for the covalent analyte. Regenerations between cycles were performed as recommended with a 3:1 mixture of 8M guanidine HCl and 1M NaOH for 120 seconds at 10 µL/min

The single cycle kinetic experiments were carried out with a data collection rate of 10 Hz, double reference subtraction, and a running buffer of 1x HBS with 1% DMSO, 0.05% tween, and 3 mM EDTA. For the bivalent analytes, concentration ranges of 0.2 – 125 nM and 0.04 – 25 nM (1:5 dilutions) were used with analyte injection flow rates of 30 µL/min. For the 0.2 – 125 nM range, a contact time of 60 seconds and dissociation time of 1800 seconds were selected. For the 0.04 – 25 nM range, a contact time of 180 seconds and a dissociation time of 1800 seconds were selected. For the covalent analyte, a 1:1 dilution series were used, with a concentration range of 15.625 – 1000 nM. For these kinetic experiments a contact time of 180 seconds and dissociation time of 1800 was used with a flow rate of 50 µL/min. The flow cell temperatures of either 25ºC or 37ºC depending on the experiment. Bivalent analytes were fitted using a bivalent analyte binding model and the covalent analytes were fitted using a two-state binding model with the second rate of dissociation (k_{d2}) manually set to 0.

3.3 Results and Discussion

Sensor Chip NTA for Monovalent Analytes

Monovalent analytes were first chosen for analysis first due to their comparatively simple experimental and analytical requirements. Due to the presence of the 6x histidine tag on the ligand, an NTA capture motif was selected for initial testing. We often prefer this as a default capture method for compatible ligands due to the high degree of surface regenerability permitting extensive reuse of the chip with low-cost surface preparation solutions.[12,13] However, NTA capture does carry some limitations that serve to reduce the popularity of the capture method amongst many industrial and academic users. First and foremost, NTA capture is predictably less stable than the more popular covalent or biotin-streptavidin based capture motifs. This results in a steady reduction in captured protein that is itself dependent on the total amount of captured material, as well as the accessibility and length of the histidine tag.[14–16] However, this ligand was found to attach with sufficient consistency, regenerability, and stability (Figure 3.1) to attempt analysis of analyte binding kinetics.

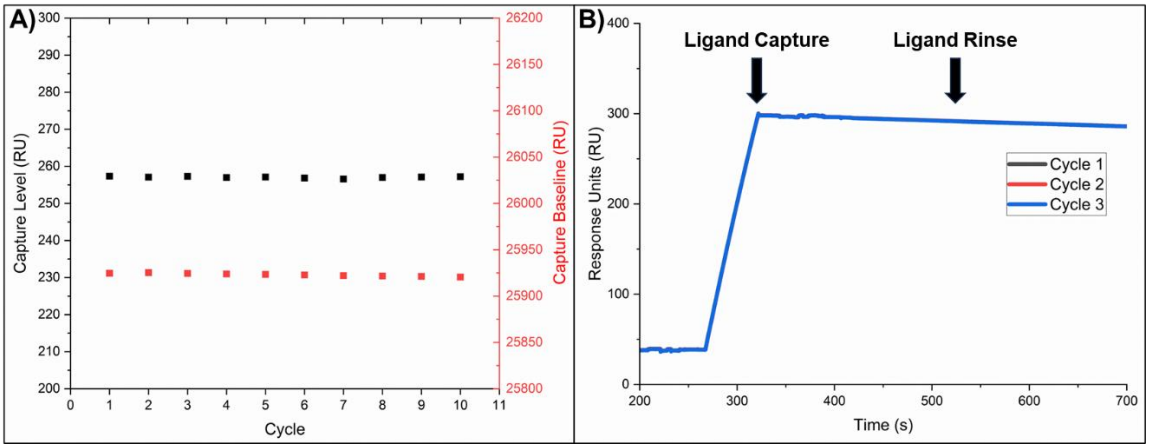

Figure 3.1. Demonstration of NTA capture and regeneration consistency for the ligand used in this work. A) Left axis shows ligand capture is extremely consistent across the all cycles of the experiment. Right axis shows the raw SPR response before ligand capture across each cycle, with no drift up indicating complete regeneration. B) Overlayed sensorgrams showing cycle to cycle consistency for ligand capture and rinse, indicating highly accurate blank subtraction.

The two monovalent analytes were first tested for their kinetic and affinity values using NTA capture (Figures 3.2A & 3.2B). Because both analytes contained the same warhead, similar affinity (K_D) values were observed as expected, but sensorgram quality control parameters, particularly the uniqueness value (U-value) were less ideal for monovalent analyte 1 (MA1) compared to monovalent analyte 2 (MA2) (Table 3.1). This high measure indicates poor reliability of kinetic parameters for this analyte, although the overall affinity value (ratio between the kinetic values) is likely reliable. There are two potential explanations for this result, with the first being that it is caused by the noticeable downward drift observed at steady state. This is an artifact that commonly arises with NTA-capture, where inconsistent ligand capture or rinse-off rates lead to inaccurate blank subtraction. Alternatively, this issue can arise from mass transport limitations. Though a theoretical maximal response (R_{max}) of 20 RUs is a common starting point for what ligand

attachment level (R_L) to target, analytes with particularly fast rates of association (k_a) maybe require less ligand attachment or faster flow rates to accurately gauge kinetic values. However, the similar molecular weights, warheads, and SPR method parameters indicate that mass transport effects were likely not the primary cause of the discrepancy in the measured kinetic constants between the two analytes.

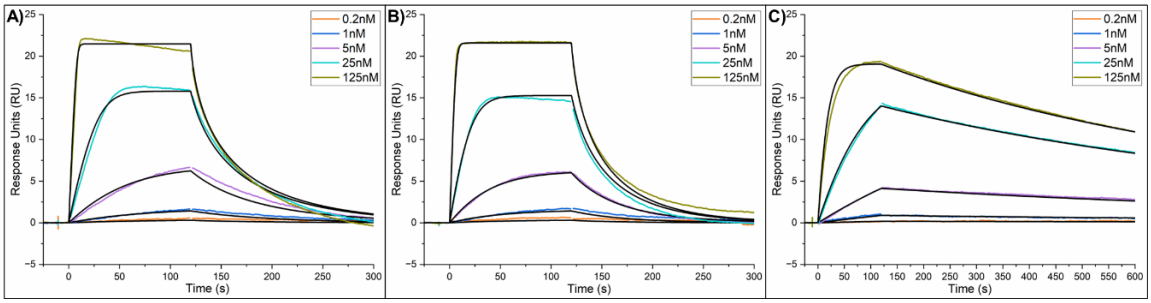

Figure 3.2. Kinetic SPR plots for the MA1 (A), MA2 (B), and MA3 (C) acquired under the same conditions on sensor chip NTA. Strong overlap between the experimental data and the kinetic fits can be observed along with distinct kinetic profile differences between the novel analytes in this work (MA1 & MA2) and the literature analyte (MA3).

Moving forward with the NTA capture motif, binding kinetics of a previously reported monovalent analyte was collected for comparison to the analytes novel to this work (Figure 3.2C). Compared to the other monovalent analytes, substantially different kinetics were observed, with slower rates of association and dissociation. Despite this, the K_D value of 2.19 nM was comparable to monovalent analytes 1 and 2 (MA1 & MA2), with values of 12.3 nM and 14.4 nM respectively. Overall, the NTA capture motif proved to be acceptable for acquiring quality kinetic and affinity data for this ligand and class of analyte.

Analyte	k_a (1/Ms)	k_d (1/s)	K_D (nM)	Chi^2 (RU^2)	tc	U-Value
MA1	1.41×10^7	1.74×10^{-1}	12.3	2.22×10^{-1}	6.86×10^6	95
MA2	7.07×10^6	1.02×10^{-1}	14.4	1.16×10^{-1}	1.01×10^7	7
MA3	5.83×10^5	1.28×10^{-3}	2.19	4.64×10^{-2}	7.30×10^6	1

Table 3.1. Table of kinetic, affinity, and quality control values for the three monovalent analytes. Chi^2 is a measure of the closeness of the fit to the experimental data with <1 RU^2 being ideal. The transport coefficient (tc) is a measure of the mass transport to the surface. The uniqueness value (U-Value) indicates if kinetic values can be determined consistently from independent injections with an ideal value < 15.

Challenges and Limitations of NTA Capture for Bivalent and Covalent Analytes

Next moving to acquisition of kinetics and affinity parameters for the bivalent analytes, it was immediately clear that the system was not performing optimally. Initially obtained kinetic curves obtained for bivalent analyte 1 (BA1) showed unusual shapes, with linear increases during the association phase, and upward drift during dissociation (Figure 3.3A). This issue can be visualized through comparison of the unsubtracted analyte injection curves to those of the buffer blanks (Figure 3.3B). The buffer injection showed no change or a slight acceleration of the downward drift that is expected from ligand dissociation on sensor chip NTA, whereas the bivalent analyte injections instead showed a reduction in the slope of this dissociation. Hence, blank subtraction will result in the lack of a visible dissociation phase in the final sensorgrams.

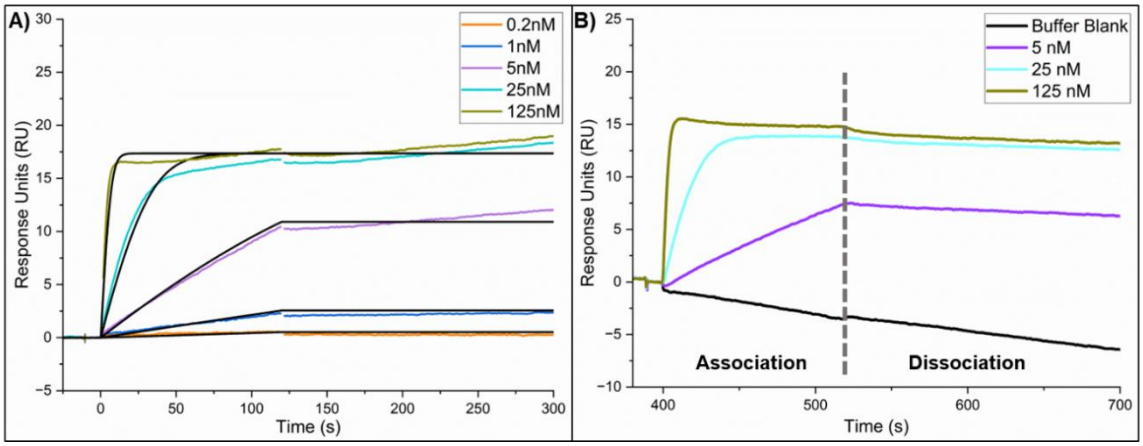

Figure 3.3. A) Double reference subtracted sensorgrams for BA1 on sensor chip NTA. B) Sensorgram without blank subtraction, showing clearly that injections of the bivalent analyte reduce ligand rinse off compared to a buffer blank, explaining the lack of dissociation observed after blank subtraction.

The best explanation for this behavior is that the analytes are reducing the dissociation of the ligand. The most likely mechanism is that by having two high affinity binding sites for the ligand, the bivalent analytes can reduce rinse off of the ligand from the flow cell. If the analyte is doubly-bound, it may keep detaching ligand molecules in proximity to NTA groups for long enough to enable rebinding (Figure 3.4A). Additionally, it is reasonable to assume that singly-bound analytes could pull down detached ligand molecules from solution, thus further reducing the observed rinse off rate (Figure 3.4B). However, due to the limited insights that can be drawn from SPR data alone, it is impossible to conclude which of these mechanisms is playing the larger role. Furthermore, if this could be identified, there is not a practical method to correct it. Instead, the most feasible method for improving data quality is to switch capture motif entirely.

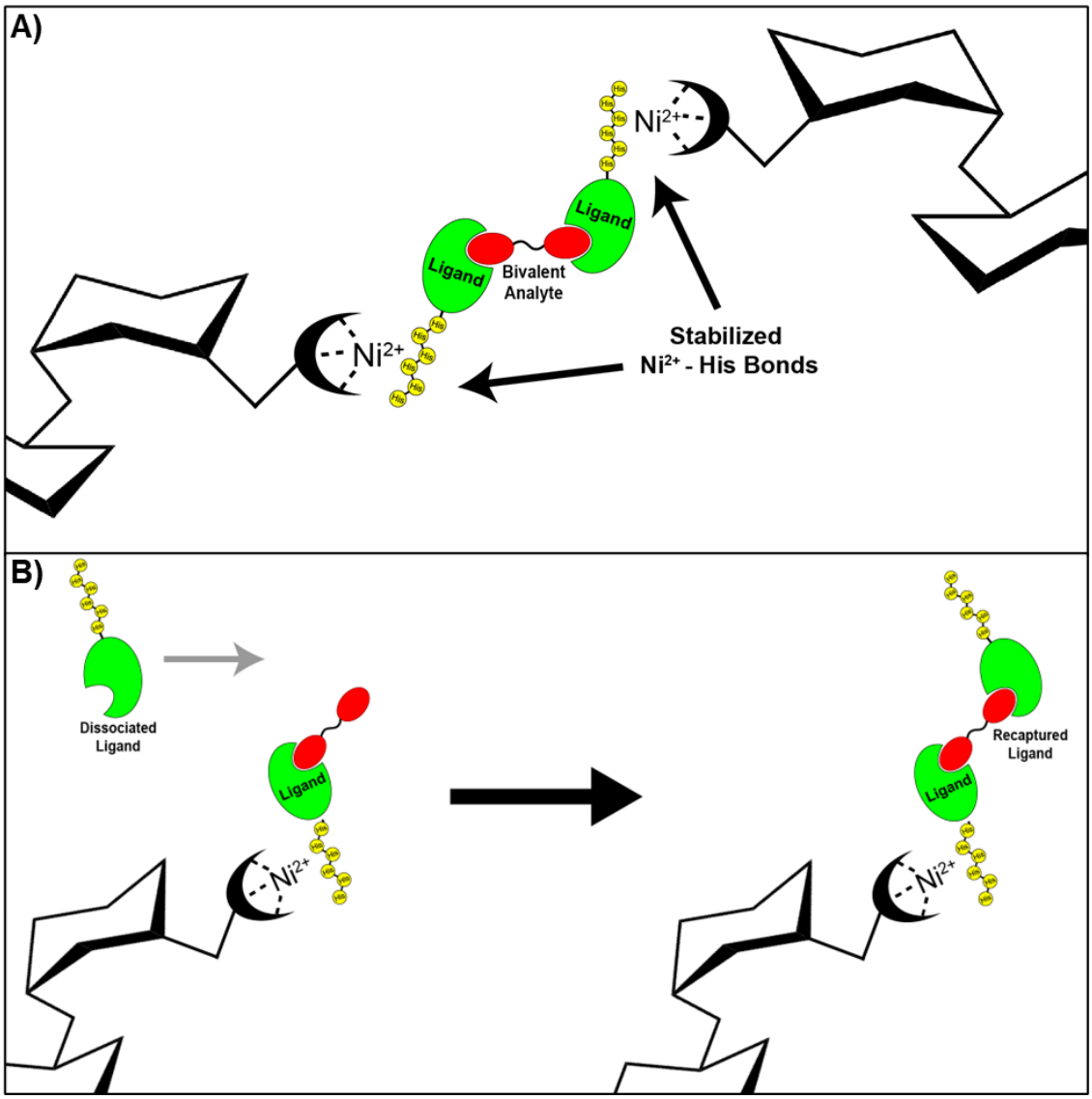

Figure 3.4. Potential mechanisms for reduced ligand dissociation from sensor chip NTA when using bivalent analytes. A) Illustrates a doubly bound analyte decreasing the likelihood of ligand dissociation by keeping it in proximity to the surface. B) Free-floating dissociated ligand may be recaptured by free warheads on the singly bound bivalent analytes.

If the previously outlined theories are correct, more stable capture of the ligand should entirely resolve the issue. We first attempted to remove ligand rinse off by covalently capturing the ligand on an NTA sensor chip using EDC-NHS linkage (Figure 3.5A). However, initial results were not promising, with upward drift occurring during dissociation (Figure 3.5B). Due to the need for troubleshooting and the high cost associated with covalent capture, it was decided to use an entirely different method offering stable capture with higher regenerability of the surface for future bivalent analyte experiments.

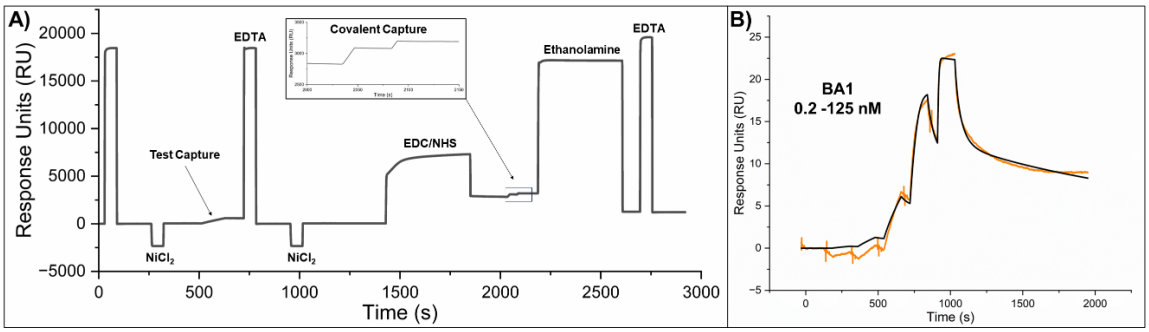

Figure 3.5. A) Labelled full sensorgram of the process for covalent capture on sensor chip NTA. The use of an NTA chip allows for preconcentration of ligand near the surface without needing to induce negative charge through the use of low pH buffers. B) Initial testing of BA1 on the covalently linked NTA surface showed artifacts such as negative shifts at low concentrations and upward drift during dissociation, making kinetic insights unreliable.

To conclude our investigation of the feasibility of NTA capture for this system, we next tested an analyte modified with a warhead allowing for covalent attachment to the ligand after extended contact within the binding pocket. Theoretically NTA capture is a practical and cost-effective option for covalent drugs because, unlike typical carboxymethyl dextran sensor surfaces that rely on covalent attachment of the ligand, the ligand can be easily stripped between analyte injections. Therefore, kinetics for multiple concentrations of the covalent analyte (CA) can be collected rapidly without previously

captured analyte interfering with the following injection. This allows for rapid multicycle kinetic characterization of both transient and permanent binding that would not be possible with more traditional capture motifs.

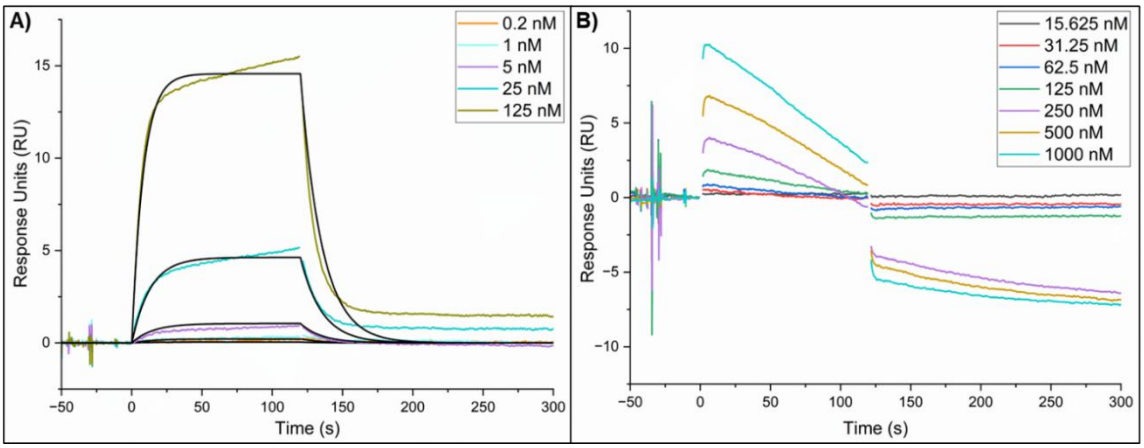

Figure 3.6. Results of initial testing of CA1 on sensor chip NTA. At 25 ºC (A), clear covalent binding shifts are apparent, particularly at higher concentration. At 37 ºC (B), the experiment completely fails due to accelerated ligand rinse off.

Initial testing was moderately successful with some covalent binding apparently visible after higher concentration injections (Figure 3.6A). However, NTA capture still shows some limitations when it comes to collecting and reliably interpreting the results. Firstly, it difficult to say with certainty that the observed change is a result of real covalent binding, as opposed to the drug causing a reduction in the rinse off rate of the ligand. If, for example, some conformation change to the protein reduces rinse-off, and this effect ceases upon dissociation, it would give the appearance of covalent binding. A secondary issue is that NTA capture does not perform well at physiological temperatures, with substantially increased dissociation of the ligand observed at 37 ºC, resulting in poor blank subtraction (Figure 3.6B). Some experiments conducted at 25 ºC may underestimate the rate of covalent bond formation relative to physiological temperature, necessitating

methods that are compatible with quantifying covalent binding at a range of temperatures.[17] Clearly a more stable capture method is needed to reliably characterize the binding behavior of covalent analytes as well as bivalent analytes.

Cap-Tag Capture Kit and Considerations for Calculating Bivalent Analyte Kinetics

To resolve the aforementioned limitations, we selected a new method recently developed and commercialized by Cytiva named cap-tag. By functionalizing their traditional carboxymethyl dextran sensor chips with DNA oligomers, a ligand conjugated the complementary strand can be immobilized with high stability. Furthermore, the complementary strands can be easily cleaved with a mixture of guanidinium chloride and sodium hydroxide, thereby allowing for regeneration of the surface. Their ready-made cap-tag conjugation kit was used to add the DNA oligomer to our ligand non-specifically at either lysine or cysteine residues that are solvent exposed. While the exact mechanism is proprietary, the attachment is likely achieved through nucleophilic attack of a maleimide conjugated to the oligomer by free thiols on the protein.[18] Traut's reagent is included in the formulation, where it is likely used to convert free primary amines on the lysines to thiols in cases where there is no pre-existing thiol available.[19,20] Despite the ligand having a molecular weight below what is recommended for the provided spin columns, it was able to be tagged and purified from the free oligomer, though with some loss of yield.

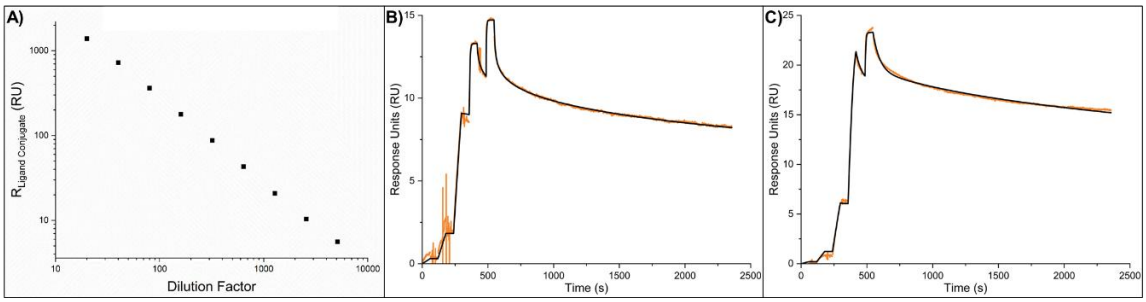

Figure 3.7. A) Ligand capture shift plotted vs the dilution factor of the cap-tagged ligand stock. Single cycle kinetic sensorgrams of BA1 (B) and BA2 (C) at concentrations of 0.2 - 125 nM in 5-fold dilutions.

With the cap-tagged ligand prepared, we first scouted the capture level of the protein at a set injection time with a range of dilutions as recommended. By plotting capture level vs. dilution factor (Figure 3.7A), it was determined that a 1:160 dilution was ideal for testing the bivalent analytes. Next, kinetic experiments were conducted for BA1 and BA2 with concentrations ranging from 0.2-125 nM in 5-fold dilution steps (Figure 3.7B & 3.7C). The results were significantly improved when compared to NTA, owing to the enhanced stability of the capture allowing for clear observation of analyte dissociation without interference from ligand dissociation changes. Compared to the monovalent analytes, substantially slower dissociation was observed, heavily indicating improved drug efficacy. However, a measure that acts as a point of comparison between analytes is necessary to quantitatively compare them and estimate their effectiveness in real systems.

The overall binding affinity (K_D) is the most commonly reported value for comparing drug effectiveness, calculated in simple monovalent systems by dividing the k_d by the k_a. In bivalent systems, however, affinity must be decomposed into two distinct components that reflect different binding states: K_{D1}, which represents the initial binding event between the analyte and a single ligand, and K_{D2} which instead quantifies the

secondary binding event of the unbound analyte warhead to a nearby unoccupied ligand. This system can be more clearly represented by the following equation:

$$2L + A \underset{k_{d1}}{\overset{k_{a1}}{\rightleftarrows}} LA + L \underset{k_{d2}}{\overset{k_{a2}}{\rightleftarrows}} LAL \quad (3.1)$$

Because the secondary association (k_{a2}) is not driven by analyte concentration, it cannot be reported in the traditional units of $M^{-1}s^{-1}$, and is reported as units of $RU^{-1}s^{-1}$.[21,22]

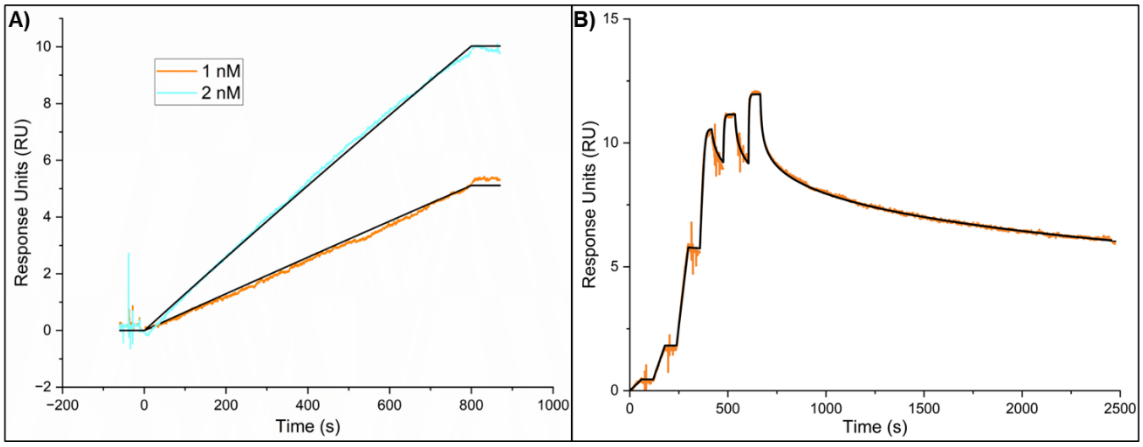

Figure 3.8. A) 800 second injections of BA1 at different concentrations demonstrating how it may be impossible to reach steady state below R_{max} for analytes with very slow dissociation. B) Single cycle kinetic sensorgram of BA1 from 0.33 – 81 nM in 3-fold dilution steps. Three distinct R_{max} values can be observed as higher concentrations favor the bivalent analyte being singly bound to the ligands.

Though there have been attempts to convert the units of k_{d2} from RUs to molarity, there is no widely accepted method that would allow for meaningful comparison across different experiments or publications.[23] A simple potential method is to determine the shift at a steady state below the R_{max} for an analyte concentration, and to simply divide that shift by the injected concentration, yielding a conversion factor in terms of RU/M that can be multiplied by the k_{a2}. There are a few limitations to this approach, with the first being that

for interactions with particularly slow dissociation, it may not be possible to reach a steady state below the R_{max}, even with a maximal injection time (800 seconds for Biacore™ systems at a flow rate of 30 µL/min), and a low concentration of analyte (Figure 3.8A).[24] The second major limitation is that standard steady state assumptions do not hold beyond monovalent systems, with the shift at steady state being heavily dependent on analyte concentration.[25] Figure 3.8B helps to illustrate how it is difficult to assign a true R_{max} value when higher analyte concentrations can begin to favor the formation of singly-bound ligands, thus gradually pushing the R_{max} higher. Thus, to find a true R_{max}, a very high concentration of analyte, far beyond the ligand-analyte affinity, would need to be injected to reach near to 100% formation of the singly bound state, likely leading to inaccurate assessment of kinetic values in the process.

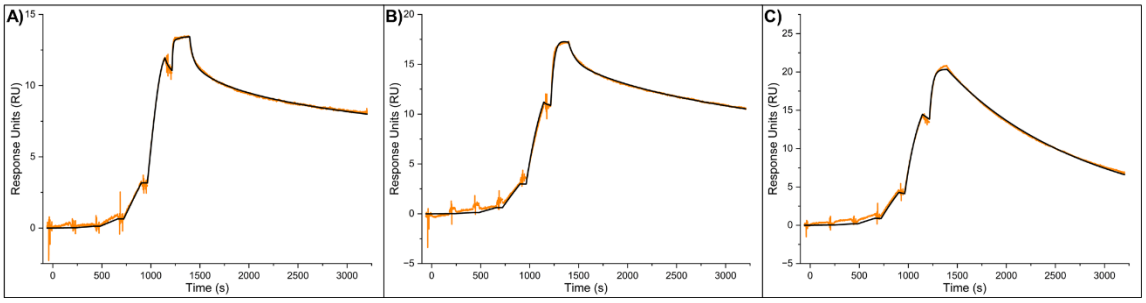

Figure 3.9. Single cycle kinetic sensorgrams of BA1 (A), BA2 (B), and MA1 (C) with concentration ranges of 8 pM to 25 nM in 5-fold dilution steps. Fitted line (black) was generated using a bivalent binding model for BA1 and BA2, and a 1:1 fitting model for MA1.

The second, and more common method for finding the RU to M conversion factor relies on the relationship between mass on the sensor surface and the response in terms of RUs, which has been assessed experimentally as approximately 1 RU for a surface mass concentration of 1 pg/mm^2 (or 10^{-6} g/m^2).[26] From this value, the concentration of analyte

(in molarity) at the surface can be determined based on the shift and the molecular weight of the ligand. Unfortunately, this method relies on many assumptions that, when taken in their totality, cast much doubt on its ability to allow for accurate comparison of K_{D2} values between different systems, sensor surfaces, and instruments. First, the calculated value for the relationship between RUs and surface mass was determined on a single type of sensor chip (CM5), which does not have a widely agreed upon thickness of its dextran layer, with that value having substantial implications on the concentration of analyte at the surface. With estimates between 100-200 nanometers, the concentration of analyte within the dextran could vary by a factor of 2, depending on what thickness was selected for calculations.[27,28] These concerns taken with others such instrument to instrument variations in sensitivity, as well as ligand immobilization and the sensor chip surface affecting ligand proximity, further reinforces the idea that comparison between K_{D2} values in different systems is not accurate or feasible.[29] Instead the drop in shift during a set dissociation time, normalized to the R_{max} is likely a somewhat acceptable but imperfect method for comparing bivalent analyte dissociations, while the k_{a2} and K_{D2} values are best treated as a qualitative measure of avidity. With these considerations in mind, final measurements were collected for BA1 and BA2 (Figure 3.9A & 3.9B) and compared to those taken for the aforementioned literature monovalent analyte (MA1) under the same experimental conditions (Figure 3.9C). The collected kinetic values after fitting, with k_{a2} in units of $RU^{-1}{}_{s}$-1, and K_{D2} in RU, as well as the quality of the fits are reported in Table 3.2.

Analyte	k_{a1} (1/Ms)	k_{d1} (1/s)	K_{D1} (nM)	k_{a2} (1/RUs)	k_{d2} (1/s)	K_{D2} (RU)	Chi^2 (RU^2)
BA1	3.38×10^{6}	2.62×10^{-2}	7.77	8.34×10^{-3}	6.94×10^{-4}	8.32×10^{-2}	1.25×10^{-2}
BA2	4.34×10^{5}	1.04×10^{-2}	23.9	2.45×10^{-3}	3.33×10^{-4}	1.36×10^{-1}	6.15×10^{-3}
MA1	1.39×10^{6}	6.92×10^{-4}	0.498	N/A	N/A	N/A	6.35×10^{-2}

Table 3.2. Kinetic and affinity values obtained from fits of single cycle kinetic data of BA1, BA2, and MA1 with concentrations ranging from 8 pM to 25 nM. Chi^2 denotes the closeness of the fit to the experimental data with a value <1 considered ideal.

Determination of Covalent Analyte Kinetics and Rate of Inactivation

With the cap-tag capture approach showing positive results for the bivalent system, we next reattempted characterizing the binding kinetics of the covalent analyte. The improved capture stability should allow for accurate and measurement of covalent binding with no concern about ligand dissociation obfuscating results. Two experiments were conducted with the same parameters except for temperature, with the first set at the standard 25 ^{o}C (Figure 3.10A), and the second at the physiological temperature of 37 ^{o}C (Figure 3.10B). Some distinct differences between the two sensorgrams are immediately noticeable. The height of the shift is lower at 37 ^{o}C, indicating lowered overall binding affinity, and despite this difference, the degree of covalent binding is significantly higher. The difference is particularly stark when considering that the height of the shift is indicative of the total amount of ligand in contact with the analyte at steady state. Thus, even with less contact between ligand and analyte, the rate of covalent binding is higher, establishing clearly that SPR measurements taken at 25 ^{o}C would substantially underestimate the effectiveness of CA1 in living systems.

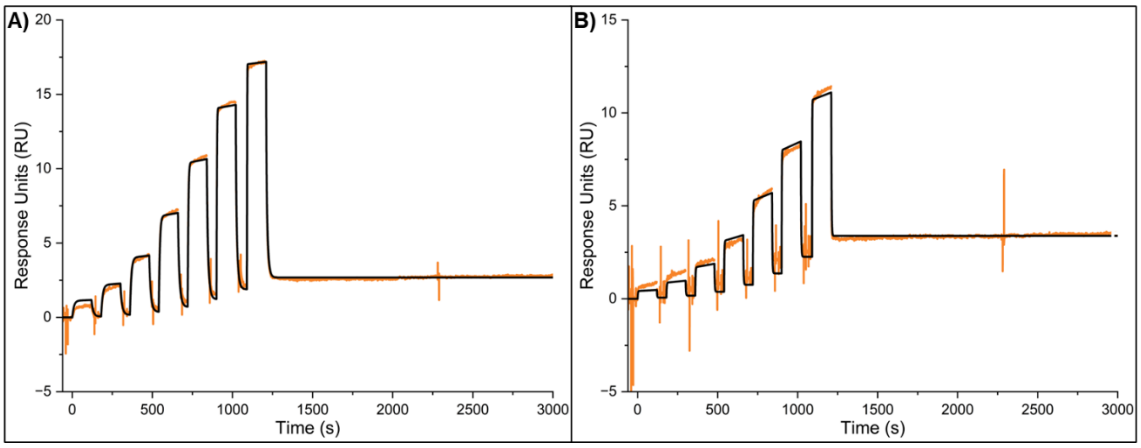

Figure 3.10. Single cycle kinetic sensorgrams of CA1 at 25 °C (A) and 37 °C (B) with concentrations between 15.625-1000 nM in 2-fold dilutions, showing clear covalent binding. Higher temperatures seem to drive higher rates of covalent binding despite less affinity for the initial reversible interaction.

While these observations are useful for qualitative comparisons, accurately quantifying binding interactions is essential for comparing the effectiveness of different covalent analytes and evaluating how experimental conditions influence their performance. The recent explosion of interest in the development of covalent drug modalities has drawn much attention towards achieving this in a reproducible and high throughput manner. While the effectiveness of covalent inhibition has traditionally been reported as a half-maximal inhibitory concentration (IC50), due to the time-dependent nature of the reaction, the second-order inactivation efficiency rate constant (k_{inact}/K_I, inactivation efficiency) is now considered a better metric.[10,30] Breaking the inactivation efficiency into its components, k_{inact} is simply the rate of covalent binding with units of s^{-1}. The inactivation constant (K_I) is an equilibrium constant, with units of molarity, that can be determined using the following equation:

$$K_I = \frac{k_{off} + k_{inact}}{k_{on}} = \frac{k_{d1} + k_{a2}}{k_{a1}} \quad (3.2)$$

With SPR, the values for k_{d1}, k_{a1}, and k_{a2} are determined from a two-state reaction model fit of the experimental data, where k_{a1} and k_{d1} denote the non-covalent association of the analyte to the ligand, and k_{a2} denotes the rate of covalent binding.[9,11] Because the secondary rate of dissociation (k_{d2}) is approximately equal to zero in a covalent system, it is often manually set to that value prior to fitting and is not a factor in determination of inactivation efficiency.[30]

Before the more recent adoption of SPR as a method for determining k_{inact}/K_I, there existed many established methods for assessing covalent binding, each with some notable limitations. Enzymatic activity assays, such as the Kitz-Wilson method, which was first reported over 60 years ago, determine k_{inact}/K_I by monitoring the loss of enzymatic activity over time with various inhibitor concentrations.[31] However, they are inherently limited to enzymes with well-established substrates.[32] ITC can also be used to determine these parameters, but with clear limitations in terms of throughput (particularly with non-enzymatic systems), sample usage, and reliability of obtained kinetic data.[33,34] Intact protein mass spectrometry (IP-MS), which operates by quantifying the ratios of covalently bound and unbound ligand at different time points, is a highly robust and label-free method of determining inactivation efficiency, but it lacks in both throughput and accessibility. Additionally, it has poor time resolution and lacks measurement of the non-covalent binding kinetics (k_{a1} and k_{d1}).[30,32] Finally, endpoint competition assays offer improved throughput, but require fluorescent labels, well characterized competitive probes, and are unable to determine K_I and k_{inact} individually.[35]

With SPR-based analysis of inactivation efficiency first reported in 2017, it has quickly become a premier method for characterizing covalent drug interactions.[36] As a label-free, direct binding technique, SPR doesn't require any enzymatic activity or substrate for the ligand, thus making is compatible with a broad range of targets. Additionally, real-time measurement of binding allows for both reversible and irreversible binding rates to be determined independently, thereby providing K_I and k_{inact} individually instead of only their ratio. This can serve to guide optimization of drug design by identifying which step in the process is rate-limiting. k_{inact}/K_I values obtained with SPR have also been compared to, and shown good agreement with, those obtained from alternative methods such as IPMS and enzyme assays.[30] Finally, the recent developments of highly stable and regenerable SPR surfaces, such as cap-tag, have served to further improved the viability of SPR as a method for assessing covalent inhibitors.

Returning to the our acquired SPR data for the covalent analyte more quantitatively, we're able to better compare and understand the differences between the two different temperatures (Table 3.3). First looking at K_I/k_{inact}, there was an ~34% increase when changing the flow cell temperature from 25 ºC to 37 ºC, which while significant, does not indicate a large change in the analyte's overall effectiveness at different temperatures. However, as mentioned earlier, because SPR is able to resolve K_I and k_{inact} individually, the changes in their individual contributions to the overall inactivation efficiency are able to be determined. First looking at K_I, which can be most simply explained as the general binding affinity before a covalent bond is formed, it can be seen that the analyte binds approximately twice as effectively at 25 ºC. However, at 37 ºC, there is an ~2.5-fold

increase in the k_{inact}, or more simply put, the rate at which covalent binding occurs after the initial interaction takes place. Hence, by breaking the inactivation efficiency into its components, we're able to identify that, while the k_{inact} may be quite sufficient at physiological temperature, the comparatively poor affinity of the analyte for the ligand (~561 nM), may prevent the analyte from remaining in the necessary proximity to efficiently catalyze the reaction.

Analyte	Temp (C)	k_{a1} (1/Ms)	k_{d1} (1/s)	K_{D1} (nM)	k_{inact} (1/Ms)	k_{d2} (1/s)	K_I (M)	k_{inact}/K_I (1/Ms)
CA1	25	3.59×10^{9}	1.01×10^{3}	280	4.29×10^{-4}	0	2.81×10^{-7}	1524.9
CA1	37	9.09×10^{5}	5.09×10^{-1}	560	1.15×10^{-3}	0	5.61×10^{-7}	2049.1

Table 3.3. Kinetic and affinity values acquired from fitting experimental data with a two-state binding model with k_{d2} manually set to 0. K_I and k_{inact} were calculated from the obtained kinetic values.

3.4 Conclusion

High quality kinetic characterizations of a broad range of analyte binding modalities were successfully obtained. Through careful consideration and comparison of different surface immobilization strategies, optimal methodology was identified for each ligand class. The simple monovalent analytes utilized here could be reliably characterized with a range of capture techniques, making the most time and cost effective approach (NTA), the obvious choice. With this approach we determined that both monovalent analytes showed fast association and moderate dissociation rate, still leading to overall high affinities for the ligand between 12-15 nM. These were compared to an existing analyte targeting this ligand under identical conditions which was found to have slower association and dissociation, leading to a slightly better K_D of approximately 2 nM.

Bivalent analytes, with their more complex binding modes proved more difficult to characterize. We determined that NTA capture was unsuitable for monitoring their dissociation due to the second warhead recapturing dissociated ligand resulting in poor blank subtraction. Additionally, it was determined that NTA capture, while seeming acceptable for covalent analytes, is not reliable with higher temperatures in particular. Switching to the cap-tag capture approach resolved all of the issues with both the bivalent and covalent systems without compromising regenerability of the surface, thus allowing for efficient collection of high-quality kinetic data. With this system, it was first found that bivalent analytes showed substantially reduced dissociation when compared to the monovalent analytes, potentially indicating substantial improvements to inhibition in living systems. Finally, characterization the individual K_I and k_{inact} values of a covalent analyte was achieved for the first time, to our knowledge, with the cap-tag system revealing that while the analyte had relatively quick rate of inactivation at 37 ^oC, a low reversible affinity limited the overall inactivation efficiency.

3.5 References

1. Huber, W. & Mueller, F. Biomolecular Interaction Analysis in Drug Discovery Using Surface Plasmon Resonance Technology. *Curr. Pharm. Des.* **12**, 3999–4021 (2007).

2. Das, S., Singh, S., Chawla, V., Chawla, P. A. & Bhatia, R. Surface plasmon resonance as a fascinating approach in target-based drug discovery and development. *TrAC Trends in Analytical Chemistry* **171**, 117501 (2024).

3. Upadhyay, V., Lucas, A., Patrick, C. & Mallela, K. M. G. Isothermal titration calorimetry and surface plasmon resonance methods to probe protein–protein interactions. *Methods* **225**, 52–61 (2024).

4. Hojjat Jodaylami, M., Masson, J. F. & Badia, A. Surface plasmon resonance sensing. *Nature Reviews Methods Primers* **5**, 47 (2025).

5. Gutgsell, A. R. *et al.* Biosensor-Enabled Deconvolution of the Avidity-Induced Affinity Enhancement for the SARS-CoV-2 Spike Protein and ACE2 Interaction. *Anal. Chem.* **94**, 1187–1194 (2022).

6. Bruncsics, B., Errington, W. J. & Sarkar, C. A. MVsim is a toolset for quantifying and designing multivalent interactions. *Nat. Commun.* **13**, 5029 (2022).

7. Erlendsson, S. & Teilum, K. Binding Revisited—Avidity in Cellular Function and Signaling. *Front. Mol. Biosci.* **7**, 615565 (2021).

8. Raouf, Y. S. Covalent Inhibitors: To Infinity and Beyond. *J. Med. Chem.* **67**, 10513–10516 (2024).

9. Heppner, D. E. *et al.* Demystifying Functional Parameters for Irreversible Enzyme Inhibitors. *J. Med. Chem.* **67**, 14693–14696 (2024).

10. Strelow, J. M. A Perspective on the Kinetics of Covalent and Irreversible Inhibition. *SLAS Discovery* **22**, 3–20 (2017).

11. Mader, L. K. & Keillor, J. W. Fitting of kinact and KI Values from Endpoint Pre-incubation IC50 Data. *ACS Med. Chem. Lett.* **15**, 731–738 (2024).

12. Gunnarsson, A. *et al.* Regenerable Biosensors for Small-Molecule Kinetic Characterization Using SPR. *SLAS Discovery* **26**, 730–739 (2021).

13. Nieba, L. *et al.* BIACORE Analysis of Histidine-Tagged Proteins Using a Chelating NTA Sensor Chip. *Anal. Biochem.* **252**, 217–228 (1997).

14. Knecht, S., Ricklin, D., Eberle, A. N. & Ernst, B. Oligohis-tags: mechanisms of binding to Ni2+-NTA surfaces. *J. Mol. Recognit.* **22**, 270–279 (2009).

15. Fischer, M., Leech, A. P. & Hubbard, R. E. Comparative assessment of different histidine-tags for immobilization of protein onto surface plasmon resonance sensorchips. *Anal. Chem.* **83**, 1800–1807 (2011).

16. Kimple, A. J., Muller, R. E., Siderovski, D. P. & Willard, F. S. A capture coupling method for the covalent immobilization of hexahistidine tagged proteins for surface plasmon resonance. *Methods Mol. Biol.* **627**, 91 (2010).

17. Copeland, R. A. *Evaluation of Enzyme Inhibitors in Drug Discovery: A Guide for Medicinal Chemists and Pharmacologists: Second Edition*. (John Wiley and Sons, 2013).

18. Renault, K., Fredy, J. W., Renard, P. Y. & Sabot, C. Covalent Modification of Biomolecules through Maleimide-Based Labeling Strategies. *Bioconjug. Chem.* **29**, 2497–2513 (2018).

19. Traut, R. R. *et al.* Methyl 4-Mercaptobutyrimidate as a Cleavable Gross-Linking Reagent and Its Application to the Escherichia coli 30S Ribosome. *Biochemistry* **12**, 3266–3273 (1973).

20. Jue, R., Lambert, J. M., Leland, P. L., Pierce, R. & Traut, R. R. Addition of Sulfhydryl Groups to Escherichia coli Ribosomes by Protein Modification with 2-Iminothiolane (Methyl 4-Mercaptobutyrimidate). *Biochemistry* **17**, 5399–5406 (1978).

21. Cytiva Life Sciences. *Biacore: Principles of Kinetics and Affinity Analysis*. https://cdn.cytivalifesciences.com/api/public/content/digi-33042-pdf (2023).

22. Henseleit, A. *et al.* Kinetic Analyses of Data from a Human Serum Albumin Assay Using the liSPR System. *Biosensors* **5**, 27–36 (2015).

23. Tiwari, P. B., Üren, A., He, J., Darici, Y. & Wang, X. Note: Model identification and analysis of bivalent analyte surface plasmon resonance data. *Rev. Sci. Instrum.* **86**, 106107 (2015).

24. Nguyen, K. *et al.* Parameter estimation and identifiability analysis for a bivalent analyte model of monoclonal antibody-antigen binding. *Anal. Biochem.* **679**, 115263 (2023).

25. Reusch, J., Andersen, J. T., Rant, U. & Schlothauer, T. Insight into the avidity–affinity relationship of the bivalent, pH-dependent interaction between IgG and FcRn. *MAbs* **16**, 2361585 (2024).

26. Stenberg, E., Persson, B., Roos, H. & Urbaniczky, C. Quantitative determination of surface concentration of protein with surface plasmon resonance using radiolabeled proteins. *J. Colloid Interface Sci.* **143**, 513–526 (1991).

27. Topor, C. V., Puiu, M. & Bala, C. Strategies for Surface Design in Surface Plasmon Resonance (SPR) Sensing. *Biosensors* **13**, 465 (2023).

28. Karlsson, R. Biosensor binding data and its applicability to the determination of active concentration. *Biophys. Rev.* **8**, 347–358 (2016).

29. Boltovets, P. M. & Snopok, B. A. Measurement uncertainty in analytical studies based on surface plasmon resonance. *Talanta* **80**, 466–472 (2009).

30. Zhou, W., Ye, X., Pandey, S. & Du, X. Application and Cross-Validation of a High-Throughput SPR Method for Characterizing Covalent Binding Ligands. *ACS Omega* **10**, 29637–29646 (2025).

31. KITZ, R. & WILSON, I. B. Esters of Methanesulfonic Acid as Irreversible Inhibitors of Acetylcholinesterase. *Journal of Biological Chemistry* **237**, 3245–3249 (1962).

32. Mader, L. K., Borean, J. E. & Keillor, J. W. A practical guide for the assay-dependent characterisation of irreversible inhibitors. *RSC Med. Chem.* **16**, 63 (2024).

33. Di Trani, J. M. *et al.* Rapid measurement of inhibitor binding kinetics by isothermal titration calorimetry. *Nat. Commun.* **9**, 893 (2018).

34. Wang, Y., Wang, G., Moitessier, N. & Mittermaier, A. K. Enzyme Kinetics by Isothermal Titration Calorimetry: Allostery, Inhibition, and Dynamics. *Front. Mol. Biosci.* **7**, 583826 (2020).

35. Miyahisa, I., Sameshima, T. & Hixon, M. S. Rapid Determination of the Specificity Constant of Irreversible Inhibitors (kinact/KI) by Means of an Endpoint Competition Assay. *Angew. Chem. Int. Ed Engl.* **54**, 14099–14102 (2015).

36. Willemsen-Seegers, N. *et al.* Compound Selectivity and Target Residence Time of Kinase Inhibitors Studied with Surface Plasmon Resonance. *J. Mol. Biol.* **429**, 574–586 (2017).

Chapter 4: Ganglioside-Mediate Membrane Diffusion and Effects on EGFR Regulation in Highly Controlled Biomimetic Systems Enabled by Chemoenzymatic Synthesis

4.1 Introduction

The dense layer of glycoproteins and glycolipids that coat cell membranes, known as the glycocalyx, plays an important role in numerous biological processes. Disruption or damage to cell surface glycans has been implicated in health impairments ranging from cardiovascular disease to sepsis.[1,2] The incredible diversity of glycan structures found on cell endothelia[3] makes the contributions of specific glycans exceptionally difficult to elucidate. Exploration of the effects of a glycan structure on a specific biological process is often predicated on their acquisition in a purified form. However, identification and isolation from biological sources is complicated by the number of highly similar molecules often differing by only a single monosaccharide, or in the case of glycolipids, slight changes in tail length or saturation.[4,5] Beyond those difficulties, the development of the platforms and techniques necessary to elucidate the roles of specific glycans also presents a significant challenge that needs to be addressed.

One subset of glycoconjugates with well-established relevance to a range of biological activities are glycosphingolipids (GSLs). GSLs are glycolipids composed of a glycan headgroup glycosidically linked to a ceramide consisting of a sphingosine and fatty acyl chain. They are primarily found in the outer leaflet of cell membranes where they participate in extracellular interactions as well as lateral interactions with neighboring

lipids and membrane proteins.[6] Gangliosides are a subset of GSLs that contain at least one sialic acid moiety on their glycan headgroup. They are found nearly ubiquitously throughout the human body with the more complex gangliosides containing multiple sialic acids being particularly abundant in brain tissue.[7] Gangliosides participate in numerous cellular processes such as protein activity modulation,[8] viral docking,[9] immune response,[10] and cell-cell adhesion and signaling.[11] Among structurally diverse glycolipids, monosialogangliosides GM1 and GM3 are the most well studied due to their high prevalence in neuronal and non-neuronal tissues respectively.

Within the ganglioside component of the glycocalyx, there exists a great deal of diversity with significant variations to the length and the degree of unsaturation of the fatty acyl chain being reported.[12] Developments in chemoenzymatic synthetic methods have enabled structurally-controlled production of gangliosides with desired molecular structures.[13,14] We have recently demonstrated efficient chemoenzymatic methods for the synthesis of gangliosides ranging from monosialosides such as GM3 to highly sialylated brain gangliosides.[15] Additionally, we have shown that this method can be applied for the production of low abundance gangliosides including those containing *N*-glycolylneuraminic acid (Neu5Gc), a sialic acid form produced by non-human animals,[16,17] which have been associated with cancer progression and inflammation.[18,19] Using these synthetic methods, investigations into biological mechanisms and potential therapeutic benefits of gangliosides can be realized.

Numerous studies have demonstrated the neuroprotective effects of gangliosides, with exogenously administered gangliosides arising as potential treatments for neurodegenerative disorders such as Huntington's Disease and Parkinson's Disease.[20–22] However, ganglioside treatments have shown inconsistent results, in part due to the limited availability of structurally defined gangliosides. Beyond neurodegenerative diseases, there is strong evidence for their use as therapeutics or immunotherapy targets for certain forms of cancer.[23] In particular, certain forms of cancer with proliferation dependent on overactivation of membrane receptor proteins such as epidermal growth factor receptor (EGFR) seen as candidates for ganglioside treatments. EGFR mutations or overexpression are found in a variety of cancers, where they drive abnormal cell growth and division. Ganglioside GM3 has a well-established inhibitory effect on EGFR,[24] and aberrant expression of GM3 has observed in the majority of certain EGFR-positive cancers,[25] though the exact mechanisms of this relationship debated and not fully understood.

EGFR, along with many other transmembrane receptors, has often been found to be sequestered in low-diffusion lipid microdomains, also commonly referred to as lipid rafts. Related to this, EGFR dimerization and phosphorylation have been shown to be highly dependent on their lateral diffusion out of low-mobility membrane regions after exposure to epidermal growth factor (EGF).[26] Gangliosides, along with cholesterol and sphingomyelin,[27] are core components of lipid rafts, with diffusion studies demonstrating substantially reduced overall lipid mobility in both living cells and artificial membranes.[28,29] Computational studies have demonstrated the importance of membrane composition and structure on the electrostatic interactions that stabilize inactive EGFR

dimers.[30] The electrostatic interactions between negatively charged GM3 and the positively charged lysine 618 residue located in the juxtamembrane domain may be critical to the sequestration of resulting inhibition of EGFR in lipid rafts.[31] Further complicating the picture, direct interactions between EGFR's N-glycans and GM3 have been observed experimentally, indicating possible relevance of extracellular glycosylation in this inhibition mechanism.[24,32]

To our knowledge, no studies have comprehensively compared individual GM3 structures for their effects on their clustering, conformation, interactions with EGFR components, and inhibition of kinase activity. Here we report integration of synthetically produced gangliosides with artificial membrane mimics to help elucidate the mechanisms of EGFR modulation by GM3. This biomimetic platform enables precise control over membrane composition and experimental conditions while minimizing confounding variables that is not possible otherwise due to the heterogeneity of both cell membranes and biologically derived gangliosides. Figure 4.1 illustrates the ganglioside library and the biomimetic system employed to investigate how structural variations in gangliosides affect membrane properties relevant to EGFR activation, including lateral lipid diffusion and direct electrostatic interactions. Additionally, we demonstrate a surface plasmon resonance (SPR)-based platform and methodology for examining the effects of membrane composition on ligand-analyte interaction kinetics.

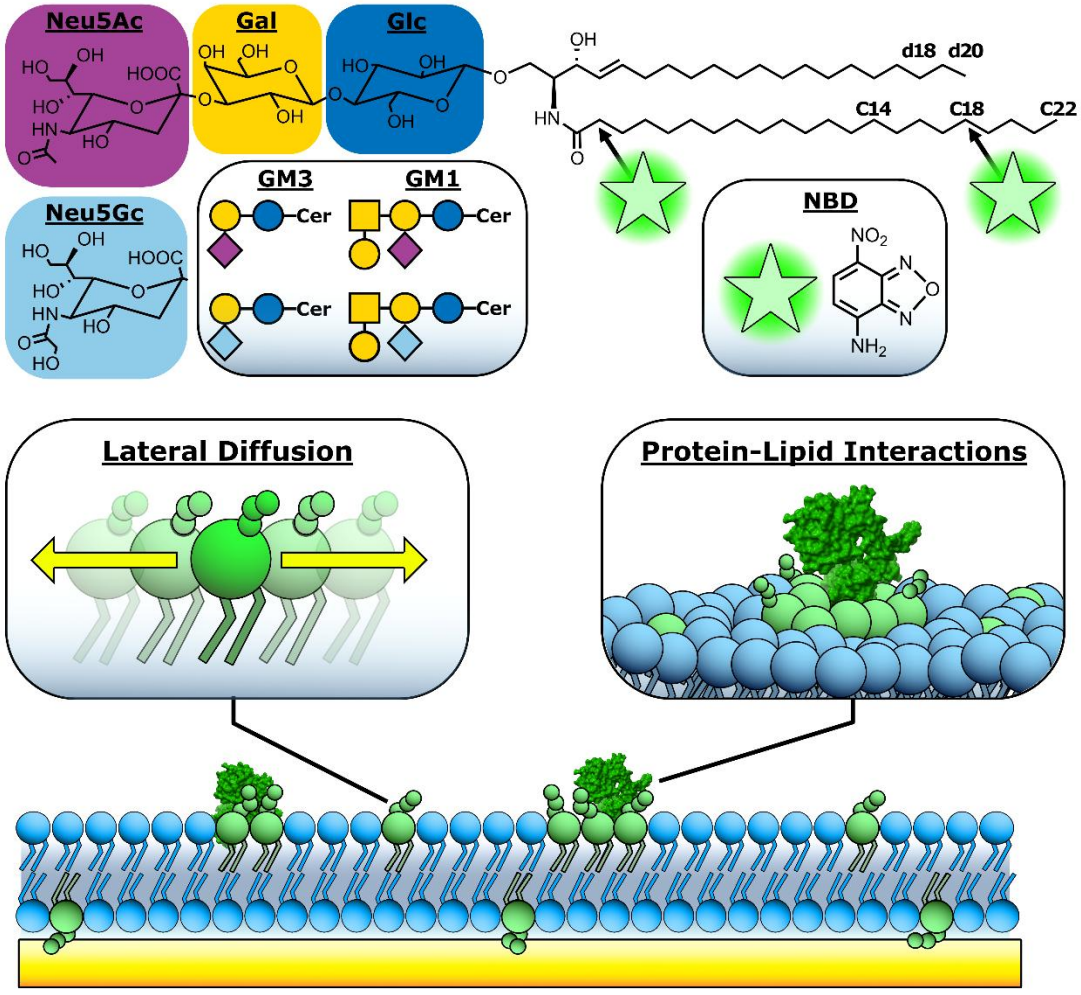

Figure 4.1. Illustration of the structural modifications incorporated into the diverse ganglioside library utilized in this study. Key variations include glycan headgroup composition, sialic acid structure, ceramide chain length, and the position of fluorescent tags. These synthetic gangliosides are incorporated into biomimetic lipid bilayers for the investigation of their effects on the diffusion properties of membrane lipids and the binding affinity of membrane-associated proteins.

4.2 Experimental Methods

Materials and Reagents

1-Palmitoyl-2-oleoyl-glycero-3-phosphocholine (POPC), 1,2-dioleoyl-sn-glycero-3-[(*N*-(5-amino-1-carboxypentyl)iminodiacetic acid) succinyl] (nickel salt) (DGS-Ni-NTA), octadecanoyl sphingomyelin *N*-octadecanoyl-D-erythro-sphingosylphosphorylcholine *N*-(octadecanoyl)-sphing-4-enine-1-phosphocholine (18:0 sphingomyelin), cholest-5-en-3ß-ol (cholesterol), monosialoganglioside GM1 (Ovine Brain), monosialoganglioside GM3 (Bovine Milk), 1,2-dipalmitoyl-sn-glycero-3-phosphoethanolamine-*N*-(7-nitro-2-1,3-benzoxadiazol-4-yl) (ammonium salt) (NBD-PE), mini stainless steel extruder kit, and 100 nm polycarbonate thin film membranes were purchased from Avanti Polar Lipids (Alabaster, Al). Premium plain BK-7 glass microscope slides were purchased from Fisher Scientific (Pittsburgh, PA). Micro cover glass slides were purchased from VWR international (Radnor, PA). Polydimethylsiloxane (PDMS) films were made using a SYLGARD^{TM} 184 Silicone Elastomer Kit purchased from Dow Chemical Company (Midland, MI). Recombinant human EGFR protein (ECD, His Tag) was purchased from Sino Biological US Inc. (Paoli, PA). Recombinant animal-free human EGF was purchased from PeproTech (Cranbury, NJ). Sensor chip L1, sensor chip NTA, and NTA capture reagents (350 mM EDTA & 0.5 mM $NiCl_2$) were purchased from Cytiva (Uppsala, SE). Fatty acid free bovine serum albumin (BSA) was purchased from Fisher Bioreagents (Waltham, MA). Low retention 1.5 mL microfuge tubes were purchased from Fisher Scientific (Waltham, MA). Chemicals for ganglioside synthesis were obtained from commercial suppliers were used without further purification.

Purification and Characterization of Ganglioside Library

^{1}H NMR spectra were recorded on a Bruker 600 MHz Spectrometer at the University of California, Davis NMR Facility. High-resolution electrospray ionization (ESI-Orbitrap) mass spectra were obtained from a Thermo Scientific Q Exactive HF Orbitrap Mass Spectrometer at the Mass Spectrometry Facilities in the University of California, Davis. Silica gel 60 Å (230–400 mesh, Sorbent Technologies) was used for flash column chromatography. Thin-layer chromatography (TLC, Sorbent Technologies) was performed on silica gel plates using anisaldehyde sugar staining or 5% sulfuric acid in ethanol staining for detection. GM3 (d18:1; 18:0) containing different sialic acids[1] and GM1 (d18:1; 18:0)[3] were synthesized as described previously. Other gangliosides were synthesized as described in the Supporting Information.

Lipid Vesicle Preparation

Lipid vesicle suspensions of various compositions were prepared as reported in prior work.[33,34] Lipid stock solutions of POPC, sphingomyelin (SP), cholesterol (CH), DGS-Ni-NTA, and the various natural and synthetic gangliosides were made by diluting the powders in 9:1 chloroform methanol at concentrations between 5 mg/mL and 40 mg/mL. These solutions were stored at -80 °C and removed briefly to mix at appropriate volumes in glass vials before drying under nitrogen. After drying, all solutions were stored loosely capped in a vacuum desiccator for at least 24 hours to ensure complete removal of the organic solvents. On the day of use, the lipids were resuspended in 1 mL of a 1× running buffer to a total lipid concentration of 1 mg/mL. To ensure full resuspension and mixing,

the solutions were vigorously vortexed before being sonicated at 50 °C for 1 hour. Finally, to clean up the solutions and ensure uniform size of lipid vesicles, they were extruded (15 passes) through 100 nm polycarbonate thin film filters.

SPR Methodology:

All SPR experiments were performed on a Biacore 1K SPR System (Cytiva, Marlborough, MA) with Biacore Insight Control Software Version 6.0.7.1750 using a Series S Sensor Chip L1. Data fitting and analysis was performed with Biacore Insight Evaluation Software Version 6.0.7.1750. HEPES-buffered saline (HBS) containing 10 mM HEPES and 150 mM NaCl (pH = 7.4) was used as the running buffer with a flow rate of 30 µL/min. For all experiments the sample compartment and flow cell temperatures were 25 °C. The chip surface was first prepared for lipid capture with three 30 second injections of a 2:3 mixture of isopropyl alcohol and 50 mM sodium hydroxide. The flow cell and injection system were then washed twice with running buffer before the lipid suspensions were injected for 1 hour at a flow rate of 2 µL/min. After lipid capture, the flow system was washed twice with running buffer again to remove additional material and stabilize the baseline. This was followed by a 20-minute injection of 0.01% BSA in HBS-N at 10 µL/min to passivate the surface, and two additional washes.

Next a custom single cycle kinetic analysis method was run using the following steps and parameters. First a 70 mM solution of EDTA in HBS was injected for 240 seconds at 30 µL/min to strip any metals chelated to the NTA groups in the membrane. The flow

system was then washed twice before 0.5 mM $NiCl_2$ was injected on the active channel for 60 seconds at a flow rate of 10 µL/min to load the NTA groups for capture of the His-tagged EGFR extracellular domain. After two additional washes, the EGFR was captured for 150 seconds at a flow rate of 2 µL/min and a concentration of 2.5 µg/mL. Next, single cycle kinetic injections of EGF in running buffer containing 0.01% BSA were performed for with concentration ranges of 0.33–81 nM. The contact time was 120 seconds for each concentration, and the dissociation time was 300 seconds. Regeneration between cycles was performed with another 240 second injection of 70 mM EDTA in running buffer. Data was collected at a sampling rate of 10 Hz and was double reference subtracted with 0.01% BSA buffer blanks. Three startup cycles were performed prior to analysis to normalize the channel responses to BSA injections. Experimental data was fitted to extract kinetic constants using a 1:1 (Langmuir) binding model. Sensor chip NTA control experiments were conducted under similar conditions, with the exceptions that no lipids were captured, the running buffer was HBS with 0.0025% Tween 20, and the regenerations between cycles were conducted with 60 second injections of 350 mM EDTA. Additionally, EGFR was instead captured for 200 seconds at a flow rate of 10 µL/min.

Fluorescence Recovery After Photobleaching:

Glass cover slips were cleaned by boiling in piranha solution for 1 hour followed by rinsing with water and ethanol before being dried under a stream of nitrogen. PDMS films were prepared by mixing the elastomer base and initiator mixed at a 9:1 ratio before pouring into petri dishes, degassing in a vacuum desiccator, and baking at 140 °C for at

least 1 hour. With polymerization complete, films were cut out to the size of the cleaned cover slips and three small squares were cut out of the films. The films were then adhered to the cover slips, creating three wells for sample volumes to be added.

FRAP measurements were carried out similarly as was reported in our previous work.[35] In brief, lipid mixtures were prepared as described above, with 1% NBD-PE or 1% NBD-labelled ganglioside added as the fluorescent reporter molecule. After extrusion, 100 µL of the lipid suspensions were added to each well and incubated for 1 hour in the dark. After incubation, the wells were thoroughly rinsed with 1x PBS to remove excess material before sealing them with a glass slide. Experiments were performed using an LSM 880 inverted confocal microscope (Zeiss, Oberkochen, DE). The fluorophores were excited by a 488 nm laser and imaged through a 20× dry objective. Bleaching of a 20 × 20 µm circular area was achieved by ~ 2 second focusing of the 488nm laser at 100% power. After bleaching, a 256-by-256-pixel image was acquired every 300 milliseconds for 2 minutes. This was performed in 12 different positions for each membrane composition, with 4 runs in each of the 3 wells.

Intensities within bleach and reference regions were measured using the Fiji package for ImageJ. The data was exported to excel for processing, where the intensity of the bleach region as percentage of the intensity of the reference region was plotted vs. time. The plots were exported to Origin 2024 (OriginLab, Northampton, MA) where exponential fits were performed using the Speed Fit application (Function = BoxLucas1, Iteration Algorithm =

Levenburg Marquardt). The output variables a (mobile fraction) and b were recorded. The variable b is used to determine the half-time recovery value ($t_{1/2}$) using the following:

$$t_{1/2} = \frac{\ln(2)}{b} \tag{4.1}$$

The recorded $t_{1/2}$ values are then used to determine the diffusion coefficient (D) using:

$$D = \frac{\omega^2}{4t_{1/2}} \tag{4.2}$$

Here ω is equal to the radius of the bleach spot (~10 μm), and the diffusion coefficient is reported in units of $\mu m^2 s^{-1}$. Statistical significance of differences in determined diffusions for membrane conditions were compared with analysis of variance (ANOVA) and Tukey as the mean comparison method.

Zeta Potential Measurements:

All zeta potential measurements were conducted using a Zetasizer Nano ZS90 (Malvern Panalytical, Malvern, United Kingdom). Lipid vesicle suspensions at a concentration of 1 mg/mL in 1× PBS were prepared as previously described. Lipid solutions were then diluted 1:9 in nanopure water and transferred to a DTS1070 folded capillary cell for measurement. Measurements were performed in triplicate using phospholipid material parameters (n = 1.45, k = 0.001) with a 120 s equilibration time and automatic duration, attenuation, and voltage selection.

4.3 Results and Discussion

Synthesis of 2-NBD-GM3 and 2-NBD-GM1

The dynamics of membrane lipid components can often be difficult to observe experimentally. Fluorescence microscopy studies using lipids tagged with a reporter is an effective approach but is challenged by the limitation in accessing structurally defined well-designed fluorophore-tagged gangliosides. To overcome this challenge, we have developed efficient chemoenzymatic total synthetic strategies to access structurally defined gangliosides containing diverse glycan headgroups, different sialic acid forms, various sphingosine structures, and numerous fatty acyl chains.[15,36,37] We demonstrate here that the method can be used to synthesize well-designed gangliosides and analogs with a fluorophore strategically placed at different locations of the fatty acyl chains. Nitrobenzoxadiazole (NBD) is chosen as a fluorescent lipid tag due to its small size assisting its integration into membranes while minimizing its effects on the membrane system. Tagging gangliosides with NBD at the end of the acyl chain distal to the glycan headgroup (omega position) or at the fatty acyl chain close to the glycan headgroup (alpha position) allows the investigation of molecules that interact with gangliosides at different components while minimizing the effects caused by the structural modification.[38] Previous reported preparation of fluorescently tagged gangliosides often relied on the isolation of gangliosides from animal organs followed by chemical derivatization.[39,40] The preparations could cause concerns for potential contamination of molecules from animal viruses[41] and may lead to impurities (e.g. lyso-gangliosides containing different sphingosine lengths)

that complicate results interpretation. In comparison, using a chemoenzymatic total synthesis strategy, we obtained structurally defined lyso-GM3 (d18:1) and lyso-GM1 (d18:1) with high purity without the concerns for the naturally resourced lyso-gangliosides.[15]

To install the NBD at the terminal fatty acyl group distal from the glycan head group (omega position), *N*-hydroxysuccinimide (NHS)-activated 9-fluorenylmethoxycarbonyl (Fmoc)-protected amino octadecanoate was prepared from 18-bromooctadecanoic acid via the formation of an Fmoc-protected *tert*-butyl 18-aminooctadecanoate intermediate similar to that reported previously.[15,42] Briefly, the carboxyl group of 18-bromooctadecanoic acid was protected with a *tert*-butyl group by reacting with *tert*-butanol (*t*BuOH) in THF with trifluoroacetic anhydride activation. S_N2 substitution of the bromine of the resulting compound with an azido group, followed by the reduction of the azido group and protection of the amino group with Fmoc formed the Fmoc-protected *tert*-butyl 18-aminooctadecanoate. Removal of its *tert*-butyl group under an acidic condition using trifluoroacetic acid (TFA) in triethylsilane (Et_3SiH) followed by reacting the resulting carboxyl group with di(*N*′-succinimidyl) carbonate (DSC) formed NHS-activated Fmoc-protected 18-aminooctadecanoate (Figure 4.2A). 18-NBD-GM3 (d18:1; 18:0) and 18-NBD-GM1 (d18:1; 18:0) were readily obtained by acylation of the corresponding lyso-gangliosides with NHS-activated Fmoc-protected 18-aminooctadecanoate, followed by removing the Fmoc using 20% piperidine and the installation of the NBD using NBD-fluoride in the presence of Hünig's base *N*,*N*-diisopropylethylamine (DIPEA) in DMF (Figure 4.2C).

To install NBD at the fatty acyl chain close to the glycan headgroup, a method similar to that reported previously was used.[38] Briefly, 2-azido-octadecanoic acid was additionally prepared by S_N2 substitution of the bromine in the commercially available 2-bromooctadecanoic acid with an azido group (Figure 4.2B). 2-NBD-GM3 (d18:1; 18:0) and 2-NBD-GM1 (d18:1; 18:0) were obtained by acylation of the corresponding lyso-gangliosides with 2-azido-octadecanoic acid in the presence of EDC and HOBt in DMF, followed by reducing the azide to an amino group, and then installing the NBD using NBD-fluoride in the presence of Hünig's base *N*,*N*-diisopropylethylamine (DIPEA) in DMF (Figure 4.2D).

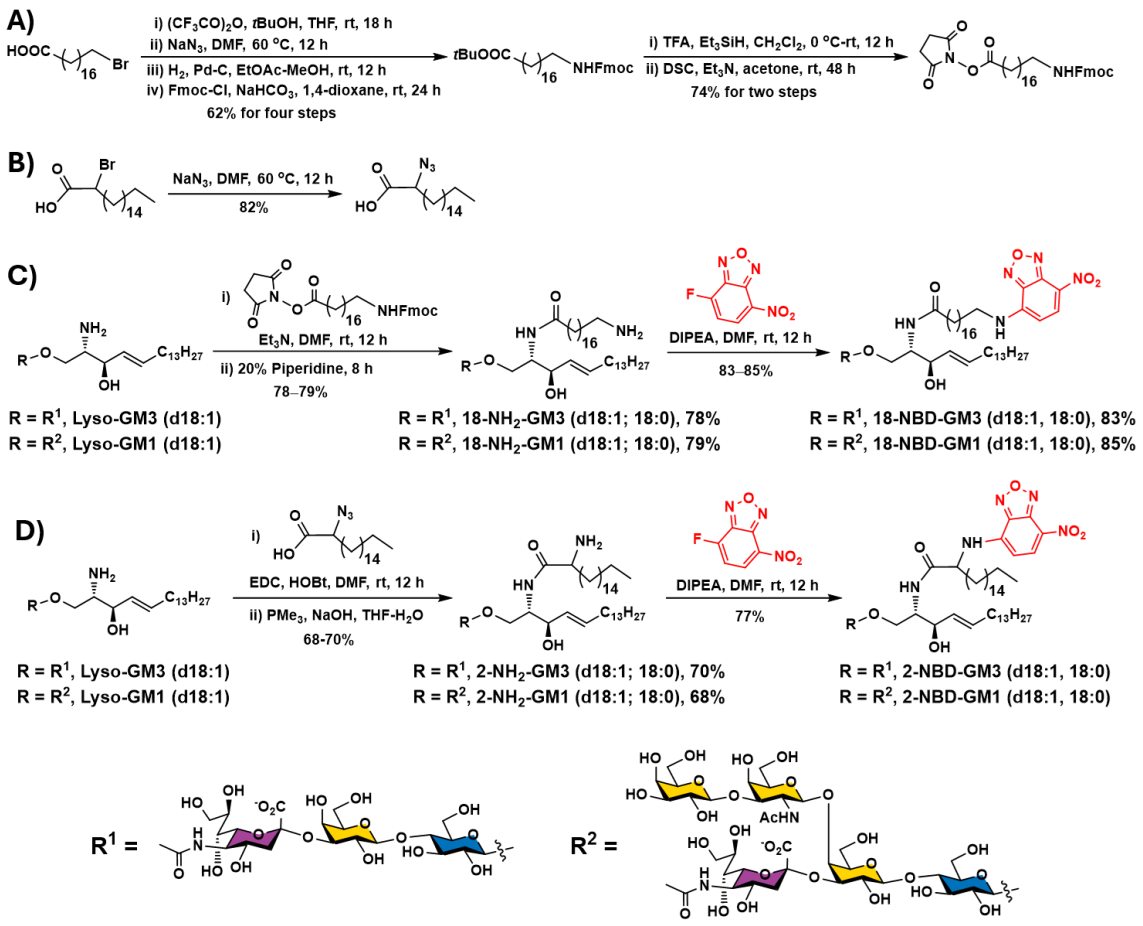

Figure 4.2. Synthesis of (A) *N*-hydroxysuccinimidyl 18-[(9-fluorenylmethoxycarbonyl)amino]octadecanoate, (B) 2-azido-octadecanoic acid, and their use in the preparation of ganglioside derivatives (C) 18-NBD-GM3 (d18:1; 18:0) and 18-NBD-GM1 (d18:1; 18:0), as well as (D) 2-NBD-GM3 (d18:1; 18:0) and 2-NBD-GM1 (d18:1; 18:0).

Diffusion and EGFR-interactions of tagged gangliosides in lipid membranes

With ganglioside (d18:1; 18:0) derivatives 18-NBD-GM3 and 18-NBD-GM1, as well as 2-NBD-GM3 and 2-NBD-GM1 successfully synthesized, an investigation of the effect of tag location on their membrane properties was carried out. By comparing the lateral diffusion between the two tags, the effect of the tag itself on gangliosides clustering and formation of membrane subdomains may be inferred. FRAP is a powerful method for observing the diffusion of membrane-bound lipids and protein.[43] The technique involves the irreversible bleaching of a small region of a fluorophore-containing artificial or cellular membranes with a high intensity laser. Recovery of fluorescence within the region of interest (ROI) can then be monitored as bleached molecules diffuse out and are replaced by unbleached molecules. The rate of recovery correlates to the diffusion speed of the tagged molecule and is mostly commonly expressed in units of $\mu m^2/s$.

The diffusion of two tagged gangliosides (2-NBD-GM3 and 18-NBD-GM3) were compared against each other and NBD-PE, a common lipid reporter (Figure 4.3). The membrane mimic vesicles composed of POPC, cholesterol (CH), sphingomyelin (SP), DGS-Ni-NTA, and the fluorescent reporter were made at molar ratios of 58:30:10:1:1. POPC is a high abundance phospholipid in eukaryotic membranes and commonly utilized in artificial membrane mimics, while cholesterol and sphingomyelin along with gangliosides play important roles in the formation of lipid rafts.[44,45] Analysis of the FRAP data showed that 18-NBD GM3 had significantly lower diffusion than 2-NBD-GM3 (0.61 ± 0.04 vs. 1.20 ± 0.08 $\mu m^2/s$). The location of the NBD moiety closer to the headgroup in

the 2-NBD-GM3 may sterically hinder the hydrophobic interactions between the ceramides of neighboring GM3, thereby reducing clustering and increasing membrane diffusion.[46] The location at the end of the ceramide on the 18-NBD-GM3 likely allows for comparatively better lipid packing. Furthermore, the terminal hydrophobic NBD on the 18-NBD-gangliosides like is able to interdigit with the distal leaflet, further lowering its diffusion.

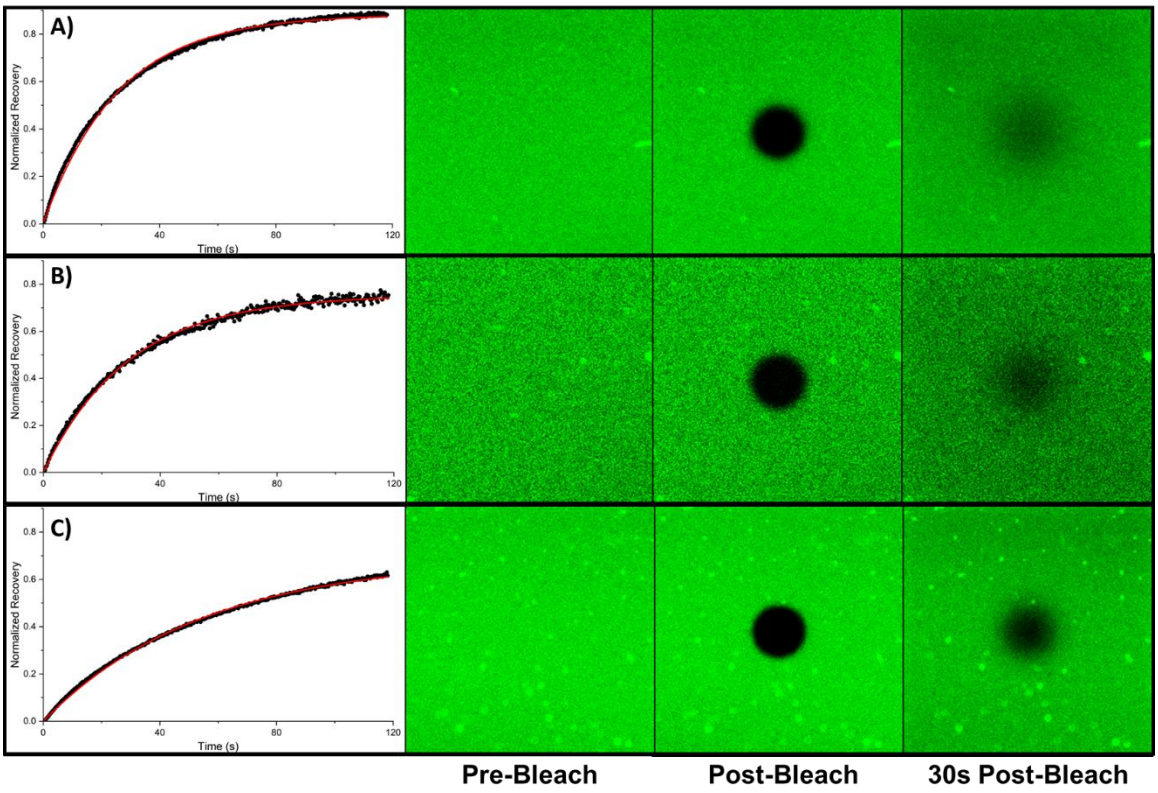

Figure 4.3. FRAP recovery curves (left) and fluorescence images (right) of POPC:CH:SP:DGS-NTA membranes containing 1% A) NBD-PE, B) 2-NBD-GM3, and C) 18-NBD-GM3.

Next, we examined the effects of EGFR recruitment on membrane diffusion properties using the NBD-tagged gangliosides (Figure 4.4). The previously described membrane compositions were compared to the same conditions after incubation of EGFR extracellular domain (EGFR-ECD). The protein was captured in the proper orientation through DGS-Ni-NTA capture of the 6×His-tag located at the C-terminus of the EGFR. Slightly higher diffusion was observed in the membranes containing 2-NBD gangliosides, for both GM1 and GM3, while the opposite effect was observed for the 18-NBD ganglioside containing membranes, though the difference is small. Past studies have indicated that ganglioside phase separation may serve as domains for EGFR concentration and clustering.[26] No clear trend in ganglioside diffusion change being observed after addition of EGFR indicates that while gangliosides may lower the diffusion of EGFR molecules by isolating them in lipid rafts, EGFR may not have a diffusion-lowering effect on the gangliosides in return. However, NBD-PE lipids were observed to have a substantial reduction in diffusion after EGFR immobilization. This effect is not unexpected, as computational studies have observed that proteins act as barriers to the lateral diffusion of membrane lipids.[47] Little observed change for the gangliosides, however, strongly indicates phase separation of gangliosides without high incorporation of the DGS-Ni-NTA, thereby minimizing EGFR-ganglioside interactions and their resulting effects on diffusion.

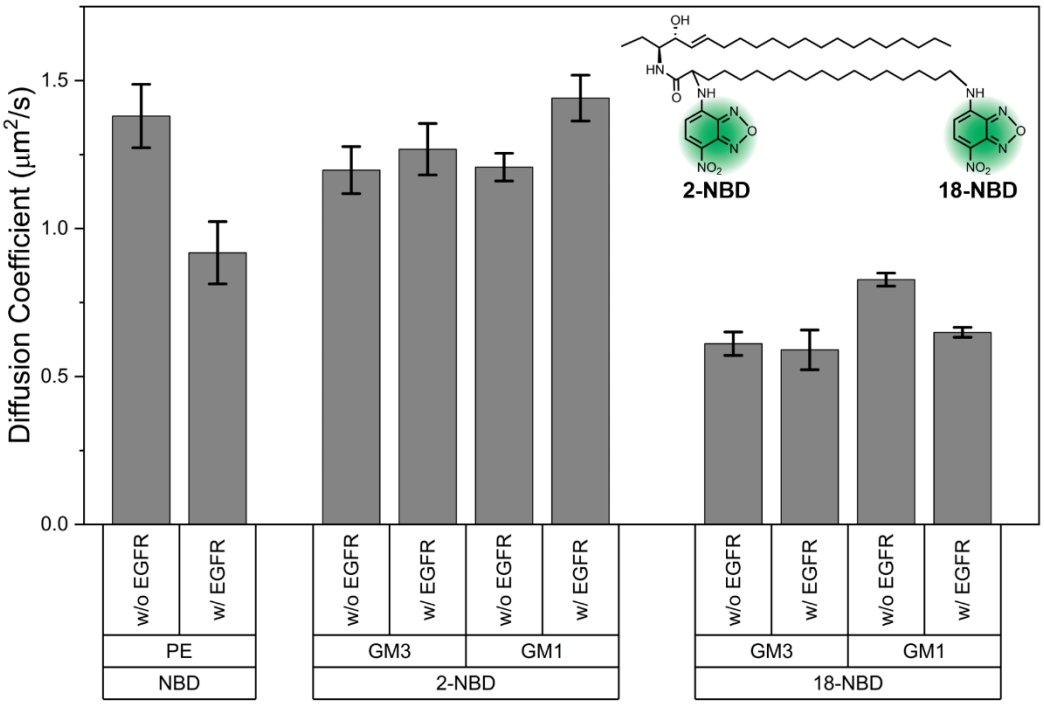

Figure 4.4. Comparison of diffusion coefficients of NBD-PE, 2-NBD-gangliosides, and 18-NBD-gangliosides on 58:30:10:1:1 POPC:CH:SP:DGS-NTA:NBD SLBs before and after incubation with EGFR-ECD.

Ganglioside ceramide structural effects on membrane diffusion

The ceramide moiety of gangliosides, composed of a sphingoid base and a fatty acyl chain, is expressed heterogeneously. In mammals, gangliosides with a fatty acyl chain between 16 and 24 carbons in length are most common, though they have been observed outside of this range.[12,48,49] The sphingosine structure can also vary, but a length of 18 or 20 carbons is the most abundant.[50] We have previously demonstrated a chemoenzymatic total synthesis method for the production of a library of GM3 molecules with different sialic acid forms, varied sphingosine lengths, and various fatty acyl chains.[15,18] Here we expand the library to include addition of GM3 and GM1 gangliosides with variations on

the sphingosine lengths (d18:1 and d20:1) and fatty acyl chains. The comprehensive libraries of GM3 and GM1 gangliosides are then used in membrane mimics to explore the influences of their structural variations on their functions.

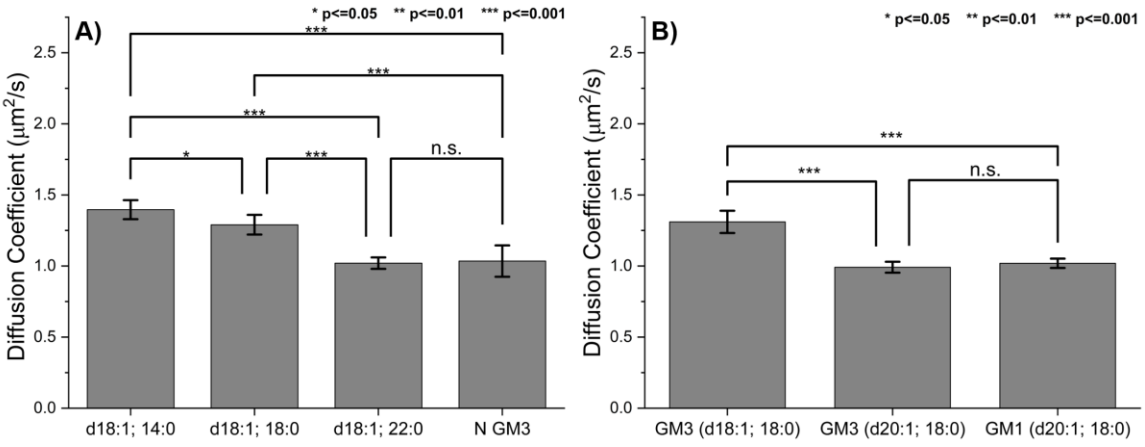

Figure 4.5. Tail group effects on NBD-PE lateral diffusion in POPC:CH:SP SLBs. A) Synthetic GM3s with fatty acyl chain lengths between 14 and 22 carbons show an inverse relationship between length and diffusion. The 22:0 GM3 containing membrane has similar diffusion to a membrane containing bovine milk derived GM3. B) Increasing the length of the sphingosine from 18 to 20 carbons results in a substantial reduction in membrane diffusion.

To test the membrane effects of varied GM3 fatty acyl chain lengths, the diffusion of NBD-PE in 58:30:10:1:1 POPC:CH:SP:NBD-PE:GM3 membranes was characterized (Figure 4.5A). An inverse relationship between chain length and NBD-PE diffusion was observed, with the largest change seen between 18C and 22C. There are two potential explanations for the observed change. First, longer tails may promote ganglioside clusters that can act as barriers to the free diffusion of other membrane components.[51] Alternatively, they can result in interdigitation with the inner leaflet,[52] as well as enhanced intermolecular Van der Waals interactions with neighboring lipids rather than predominantly with other gangliosides, thereby promoting a more ordered and tightly packed membrane

environment.[53] To further explore this question, diffusion behavior was also compared with membranes containing naturally sourced GM3 (N GM3) purified from bovine milk. N GM3 contains a heterogeneous distribution of fatty acyl tail lengths, with C22 and C23 species identified as the most abundant (Figure 4.6). The diffusion behavior observed for this condition closely matched that of the 22C membrane, indicating that the average fatty acyl chain length is likely the primary determinant of membrane diffusion, regardless of the distribution of chain lengths. This supports the hypothesis that increased lipid packing and enhanced membrane rigidity are responsible for the observed differences. To determine whether the observed effects of fatty acyl chain elongation also extend to the sphingosine backbone, diffusion of GM3 (d18:1; 18:0) and GM3 (d20:1; 18:0) containing membranes were compared under the same conditions (Figure 4.5B). Interestingly, the reduction in diffusion from this two-carbon extension was approximately equivalent to that observed for the four-carbon increase in the fatty acyl chain from C18 to C22, suggesting that sphingosine elongation exerts a greater effect on membrane diffusion on a per-carbon basis.

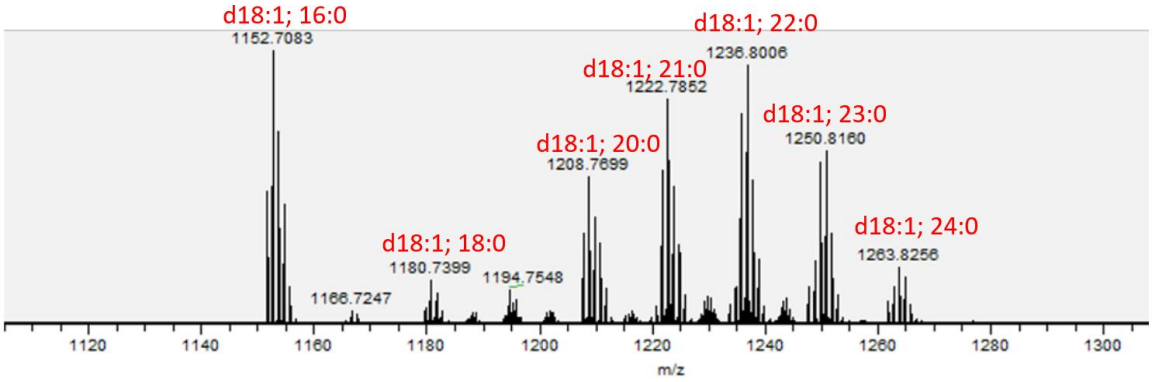

Figure 4.6. High-resolution mass spectrum (HRMS) of bovine milk ganglioside GM3 purchased from Avanti Polar Lipids (Cat. # 860058). The labelled peaks correspond to GM3 (d18:1) with varying fatty acyl chain lengths.

Modified sialic acids affecting membrane diffusion and charge

The effects of GM3 on EGFR activation are thought to arise from both direct interactions with the glycan headgroup and the formation of lipid domains that limit EGFR diffusion.[24,54] The formation of these domains is also partially a result of hydrogen bonding between the neighboring ganglioside headgroups.[55] The presence of sialic acid is the one of the defining features of gangliosides, and the relatively small modification from the human form Neu5Ac to the non-human form Neu5Gc has been associated with a range of cancers.[56] Considering these factors, it is important to better understand the effects of headgroup modifications, particularly those involving sialic acid, given its central biological significance. Synthetically produced GM3 (d18:1; 18:0) molecules with Neu5Ac and Neu5Gc sialic acids were selected for comparison, along with a fluorine-substituted sialic acid variant, as the high electronegativity of fluorine may promote unique intermolecular interactions. These molecules were synthesized as previously described.[18]

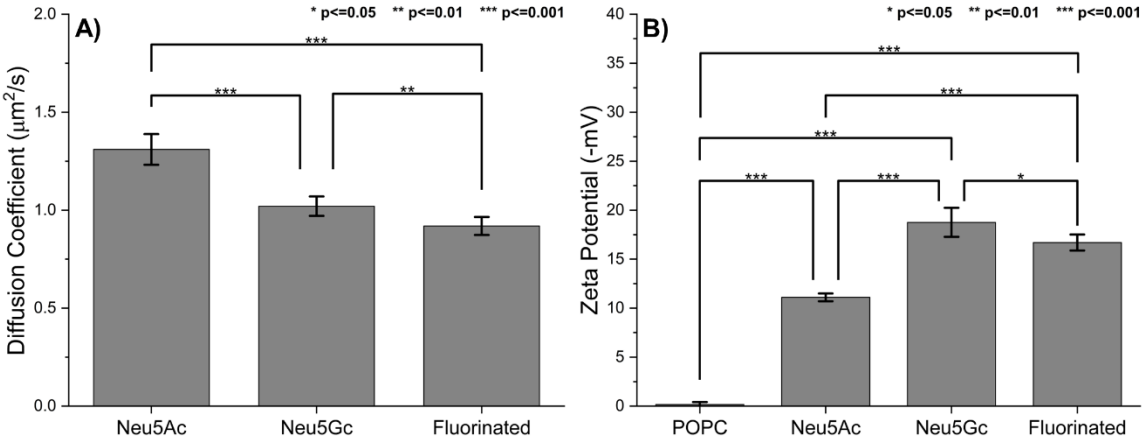

Figure 4.7. Membrane effects of GM3 sialic acid modifications. A) Differences in diffusion of NBD-PE in 58:30:10:1:1 POPC:CH:SP:NBD-PE:GM3 SLBs containing 1% GM3 (d18:1; 18:0) with different sialic acids. B) Comparison of the zeta potentials of 95:5 POPC:GM3 vesicles and plain zwitterionic POPC vesicles.

The modified GM3 molecules were first evaluated for their effects on NBD-PE diffusion in 58:30:10:1:1 POPC:CH:SP:NBD-PE:GM3 membranes (Figure 4.7). Unlike with ceramide modifications, changes in NBD-PE mobility in this case are likely to arise primarily from altered interactions involving the sialic acid or from changes in ganglioside clustering within the membrane. Lipid diffusion was found to vary significantly among the different modifications, with the largest change observed between Neu5Ac-GM3 and Neu5Gc-GM3 membranes. Although the relationship between Neu5Gc-GM3 and cancer remains incompletely understood, the effects of GM3 modification on EGFR activation has been well established. One study reported a reduced inhibitory effect from Neu5Gc supplemented EGFR overexpressing A431 cells when compared to those treated with

Neu5Ac.[57] The mechanisms underlying these observations remain difficult to elucidate, but the most likely explanations involve changes in direct interactions between the sialic acid and EGFR and/or alterations in EGFR diffusion that affect receptor dimerization. Comparison of the diffusion and charge effects (Figure 4.7B**)** of Neu5Gc and fluorinated-GM3 revealed that these parameters are not perfectly correlated (Figure 4.8). This distinction may provide an opportunity for future studies to determine whether altered EGFR activation is driven more strongly by changes in membrane diffusion or by electrostatic interactions.

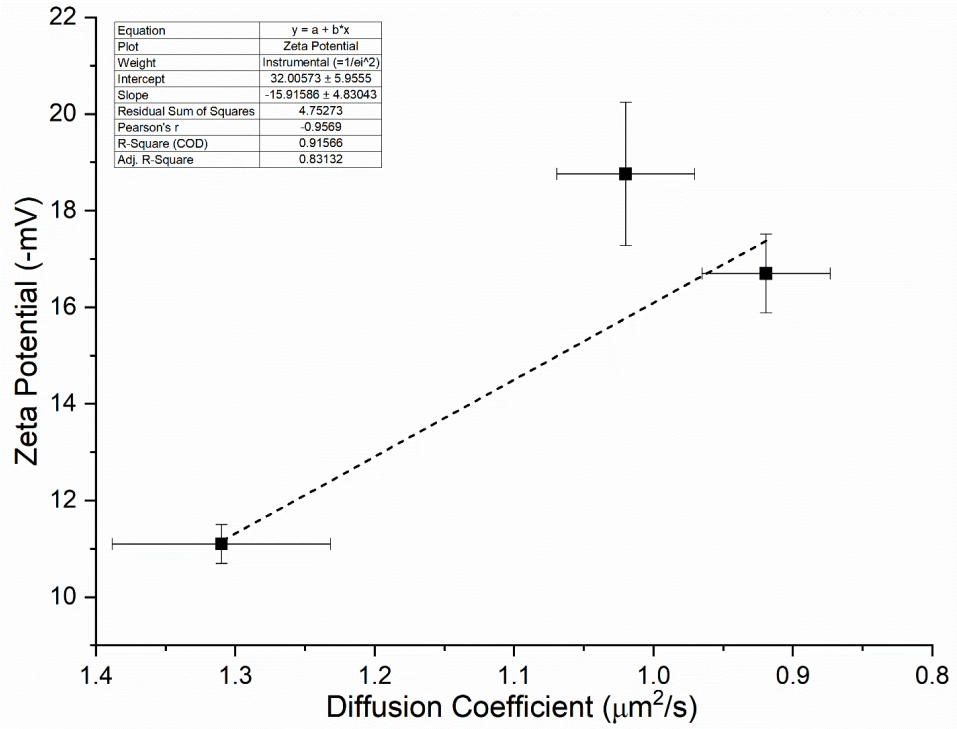

Figure 4.8. Diffusion coefficients of NBD-PE in 59:30:10:1 POPC:CH:SP:GM3 membranes containing 1% Neu5Ac, Neu5Gc, and fluorinated GM3 plotted versus the zeta potentials of vesicles composed of 95:5 POPC:respective GM3. Larger zeta potentials appear to be correlated with lower membrane diffusion, but the trend is not perfectly linear, indicating other factors other than charge may be affecting ganglioside cluster formation.

SPR platform for assessment of protein-ligand interactions in a controlled membrane environment

Investigating the specific mechanisms underlying ganglioside modulation of EGFR activity requires new approaches that allow precise control over membrane compositions. Surface plasmon resonance (SPR) is a highly sensitive, label-free technique for measuring ligand-analyte interactions. However, conventional SPR experiments are most commonly performed with ligands immobilized in random orientations through EDC–NHS coupling to a dextran matrix. To investigate the binding characteristics of membrane components and the effects of the membrane environment on protein interactions, alternative surface coatings are required. We have previously reported methods for formation of supported lipid bilayers (SLBs) on gold sensor surfaces coated with thin silica layers prepared through PECVD[58] and calcination processes.[59] The composition of these SLBs can be readily tuned to incorporate membrane components including phospholipids, cholesterol, and gangliosides, at defined ratios. In addition, incorporation of DGS-Ni-NTA lipids allows for capture of histidine-tagged ligands with defined orientations based on the position of the histidine tag. Commercial platforms for lipid bilayer capture are also available, including the Sensor Chip L1, which features alkyl-functionalized carboxymethyl dextran and has been widely used for decades. This surface was selected for our SPR analysis because its reliability and compatibility with the Biacore 1K system were essential for resolving subtle differences in kinetic profiles between membrane compositions.

This approach, combined with synthetically pure gangliosides, has strong potential for systematically investigating how individual ganglioside structures influence the affinity of EGFR and other membrane receptor proteins for ligands such as EGF. One previous study proposed that GM3 inhibits EGFR activation not through modulation of EGF ligand binding, but rather by suppressing EGFR dimerization following ligand engagement.[60] However, this conclusion was based on 4-hour incubations of radiolabeled EGF with living cells, thereby lacking real time measurement of the kinetics of the interaction. Accordingly, we believe that reexamining these interactions using modern instrumentation and real-time analytical methods is warranted.

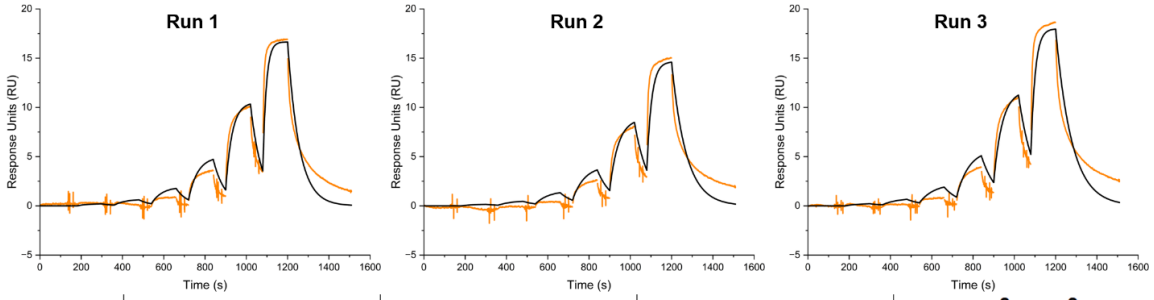

Run	k_a (1/Ms)	k_d (1/s)	K_D (nM)	Chi^2 (RU^2)
1	5.36 x 10^5	1.79 x 10^{-2}	33.3	1.21
2	3.66 x 10^5	1.42 x 10^{-2}	38.8	1.23
3	4.37 x 10^5	1.28 x 10^{-2}	29.4	1.65
Avg	**4.46 ± 0.697 x 10^5**	**1.50 ± 0.215 x 10^{-2}**	**33.8 ± 3.86**	**1.36**

Figure 4.9. Single cycle kinetic SPR data for the EGFR-EGF interaction on an NTA sensor chip. The injected EGF concentrations were 0.33–81 nM in generated through 3-fold serial dilutions.

We began our SPR analysis of the EGFR-EGF interaction by establishing a baseline affinity for the non-membrane associated EGFR extracellular domain using an NTA functionalized carboxymethyl dextran sensor chip (Figure 4.9). Across replicates (n = 3), highly reproducible affinity measurements averaging 33.8 ± 3.9 nM were obtained. This value is notably higher than literature reported affinities, which generally fall in the range of ~0.1–10 nM, depending on the binding environment and measurement method.[61,62] However, one SPR measurement performed on a similar surface reported a substantially higher K_D of ~177 nM.[63] The relatively low affinity measured on conventional carboxymethyl dextran SPR surfaces, together with the poor fit of the experimental data to a 1:1 binding model, suggest that a heterogeneous ligand population likely exists on these surfaces, with differences in EGFR conformation and/or analyte accessibility. Given the well-known interactions between the EGFR ectodomain and membrane lipids, it is possible that the protein adopts an unfavorable conformation in this non-native environment, thereby reducing accessibility of the binding pocket. Alternatively, because the protein is captured at relatively low surface densities, some EGFR molecules may exist in sufficiently close proximity to dimerize while others remain isolated, resulting in two distinct binding populations. However, the measured K_D was substantially higher than reported affinities for either the monomeric or dimeric states, suggesting that this explanation is unlikely.[64]

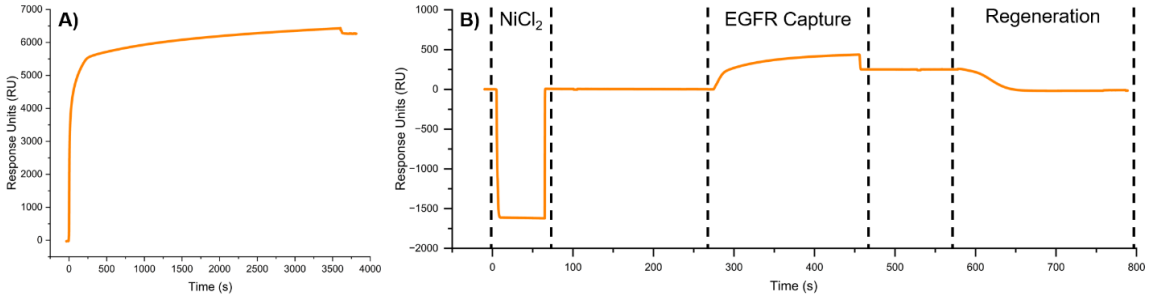

Figure 4.10. A) Sensorgram showing the capture of 55:30:10:5 POPC:CH:SP:DGS-NTA vesicles on sensor chip L1. B) Reference subtracted sensorgram showing each step in the cycles of EGFR capture and regeneration. $NiCl_2$ in water is loaded on the active channel followed by EGFR, with extremely stable capture observed afterwards. Injection of EDTA fully removes the captured EGFR, restoring the surface for the next kinetic cycle.

To determine the EGFR-EGF binding affinity within a membrane system, we first captured a lipid mixture composed of POPC, cholesterol, sphingomyelin, and DGS-Ni-NTA at a 55:30:10:5 molar ratio. Under these conditions, a capture level of approximately 6200 RU was obtained. (Figure 4.10A), indicating the formation of a continuous lipid bilayer rather than captured intact vesicles.[65] Following a 20-minute injection of 0.01% BSA to minimize nonspecific binding, the active channel was treated with $NiCl_2$ to load the NTA groups, followed by capture of histidine-tagged EGFR. Limited stability of histidine-NTA protein capture in SPR has been previously reported,[66] but in this system the captured protein proved highly stable, with almost no observable dissociation during rinsing (Figure 4.10B). The analyte solutions were prepared in low retention microfuge tubes with HBS-N containing 0.01% BSA to prevent absorptive loss of EGF. It should be noted that using BSA can lead to significant buildup within the SPR fluidics system, necessitating frequent cleaning to maintain instrument performance.

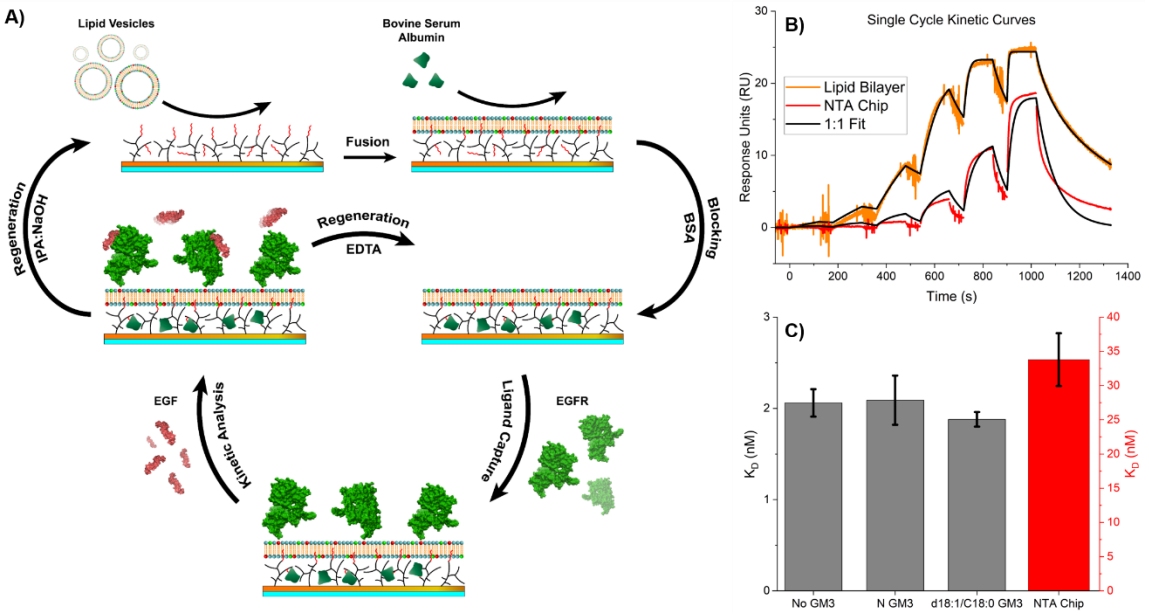

Figure 4.11. A) Schematic illustration of surface functionalization, kinetic analysis, and regeneration of the membrane-captured EGFR SPR platform. B) Representative single-cycle kinetic sensorgrams and corresponding fits for the EGFR-EGF interaction measured on a supported lipid bilayer (SLB) and an NTA chip interface. C) Comparison of affinity values (K_D) for the EGFR–EGF interaction obtained using lipid bilayers with varying ganglioside compositions and a commercial dextran-based NTA chip. The captured vesicles were composed of a molar ratio of 50:30:10:5:5 POPC:CH:SP:GM3:DGS-NTA (55:30:10:5 for membranes lacking GM3). No statistically significant differences in affinity were observed among the membrane compositions tested, but they all exhibited substantially lower K_D values than those measured using the commercial NTA chip.

The overall experimental workflow for surface functionalization, passivation, ligand capture, kinetic analysis, and regeneration is illustrated in Figure 4.11A. Single cycle kinetic experiments were conducted with EGF over a concentration range of 0.33–81 nM prepared through 3-fold serial dilutions. The membrane-bound system exhibited markedly improved fitting to a 1:1 binding model, indicating a more homogeneous population of binding-competent EGFR conformations on this surface (Figure 4.11B). Next, we determined the K_D values for the EGFR-EGF interaction on membranes with three different compositions and compared them with those previously determined on the

commercial NTA surface (Figure 4.11C). Sensorgrams, kinetic parameters (k_a and k_d), and K_D values were obtained in triplicate for each membrane condition. Figure 4.12 show 3 sets of measurements for the no ganglioside membrane and associated affinity and kinetic parameters.

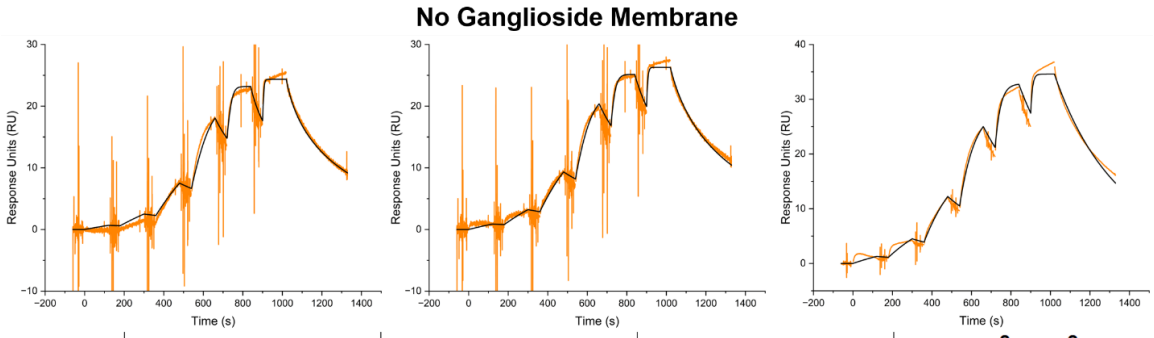

Run	k_a (1/Ms)	k_d (1/s)	K_D (nM)	Chi^2 (RU^2)
1	3.93×10^6	8.21×10^{-3}	2.09	1.27
2	2.78×10^6	5.19×10^{-3}	1.86	1.24
3	1.38×10^6	3.06×10^{-3}	2.22	0.896
Avg	**$2.70 \pm 1.04 \times 10^6$**	**$5.49 \pm 2.11 \times 10^{-3}$**	**2.06 ± 0.15**	**1.14**

Figure 4.12. Triplicate SPR single cycle kinetic sensorgrams for the EGFR-EGF interaction on a 55:30:10:5 POPC:CH:SP:DGS-NTA membrane surface. The EGF concentrations are between 0.33 and 81 nM made through 3-fold serial dilution.

Regardless of membrane composition, K_D values of approximately 2 nM were obtained, falling well within the range reported in previous studies. Consistent with prior findings, no clear differences in affinity were observed as a function of GM3 presence or structure within the membrane, further supporting the hypothesis that gangliosides do not inhibit EGFR activation through modulation of EGF binding affinity. However, this result should be interpreted with caution rather than considered definitive, as our FRAP analysis suggested that DGS-Ni-NTA lipids, and EGFR by extension, may not preferentially

partition into ganglioside-enriched membrane domains. Such spatial segregation could minimize the influence of gangliosides on the observed EGFR binding behavior.

4.4 Conclusion

The work presented here demonstrates the application of new and existing synthetic and chemoenzymatic strategies for the production and purification of structurally distinct gangliosides. Structural variations included modifications to ceramide chain length in both the fatty acyl chain and sphingosine backbone, alterations to the headgroup sialic acid, and NBD labeling at multiple positions along the lipid tails. These compounds were subsequently incorporated into artificial membrane mimics to evaluate their effects in compositionally controlled environments. FRAP analysis revealed that the position of the NBD label strongly influences ganglioside mobility within membranes, whereas the presence of EGFR exerts comparatively little effect. In addition, increasing ganglioside ceramide tail length substantially reduced overall membrane fluidity, with sphingosine elongation producing a greater effect on a per-carbon basis than fatty acyl chain extension. Modification of the GM3 sialic acid from Neu5Ac to Neu5Gc, as well as incorporation of fluorinated fatty acyl analogs, also significantly reduced membrane fluidity, highlighting the importance of sialic acid structure in regulating ganglioside clustering and membrane organization.

We also present an SPR platform that utilizes these membrane mimics to investigate how individual ganglioside structures influence the EGFR–EGF binding interaction. Using this approach, we found that conventional SPR capture strategies for a

membrane-associated protein such as EGFR may lead to substantial misestimation of binding affinity. EGFR captured on conventional NTA surfaces exhibited K_D values at least an order of magnitude higher than those obtained for membrane-captured EGFR, regardless of membrane composition. In addition, poor fits to a 1:1 binding model fits and less-than-expected maximal binding response (R_{max}) suggested heterogeneity in EGFR accessibility and/or conformational state on traditional capture surfaces. In contrast, membrane-based capture appeared to preserve a more native, binding-competent receptor conformation, resulting in markedly improved fitting behavior, enhanced binding responses, and affinity measurements that more closely matched previously reported values. Collectively, these results demonstrate that the SPR platform developed here provides a robust and versatile strategy for both the capture of membrane proteins and quantitative analysis of their ligand-binding interactions within a highly tunable biomimetic membrane environment.

Future studies should aim to expand the range of synthetic gangliosides evaluated for their effects on membrane diffusion, lipid raft formation, and EGFR binding activity. Such efforts could include broader variations in ceramide chain length, additional headgroup modifications, and incorporation of cancer-associated lyso-gangliosides. Incorporation of full-length EGFR into a similar biomimetic membrane platform may further enable investigation of ganglioside-mediated regulation of EGFR activity in a context that more closely reflects native biological environments.

4.5 References

1. Milusev, A., Rieben, R. & Sorvillo, N. The Endothelial Glycocalyx: A Possible Therapeutic Target in Cardiovascular Disorders. *Front Cardiovasc Med* **9**, 897087 (2022).

2. Sullivan, R. C., Rockstrom, M. D., Schmidt, E. P. & Hippensteel, J. A. Endothelial glycocalyx degradation during sepsis: Causes and consequences. *Matrix Biol Plus* **12**, 100094 (2021).

3. Xu, G., Goonatilleke, E., Wongkham, S. & Lebrilla, C. B. Deep Structural Analysis and Quantitation of O-Linked Glycans on Cell Membrane Reveal High Abundances and Distinct Glycomic Profiles Associated with Cell Type and Stages of Differentiation. *Anal Chem* **92**, 3758–3768 (2020).

4. Merrill Jr., A. H. Sphingolipid and glycosphingolipid metabolic pathways in the era of sphingolipidomics. *Chem Rev* **111**, 6387–6422 (2011).

5. Li, Q., Xie, Y., Wong, M. & Lebrilla, C. B. Characterization of Cell Glycocalyx with Mass Spectrometry Methods. *Cells* **8**, (2019).

6. Russo, D., Parashuraman, S. & D'Angelo, G. Glycosphingolipid-Protein Interaction in Signal Transduction. *Int J Mol Sci* **17**, (2016).

7. Palmano, K., Rowan, A., Guillermo, R., Guan, J. & McJarrow, P. The role of gangliosides in neurodevelopment. *Nutrients* **7**, 3891–3913 (2015).

8. Kabayama, K. *et al.* Dissociation of the insulin receptor and caveolin-1 complex by ganglioside GM3 in the state of insulin resistance. *Proc. Natl. Acad. Sci. U.S.A.* **104**, 13678–13683 (2007).

9. Das, A. *et al.* Gangliosides are essential endosomal receptors for quasi-enveloped and naked hepatitis A virus. *Nat Microbiol* **5**, 1069–1078 (2020).

10. van der Haar Avila, I., Windhouwer, B. & van Vliet, S. J. Current state-of-the-art on ganglioside-mediated immune modulation in the tumor microenvironment. *Cancer Metastasis Rev* **42**, 941–958 (2023).

11. Regina Todeschini, A. & Hakomori, S. I. Functional role of glycosphingolipids and gangliosides in control of cell adhesion, motility, and growth, through glycosynaptic microdomains. *Biochim Biophys Acta* **1780**, 421–433 (2008).

12. O'Brien, J. P. & Brodbelt, J. S. Structural characterization of gangliosides and glycolipids via ultraviolet photodissociation mass spectrometry. *Anal Chem* **85**, 10399–10407 (2013).

13. Jin, X. *et al.* A modular chemoenzymatic cascade strategy for the structure-customized assembly of ganglioside analogs. *Commun Chem* **7**, 17 (2024).

14. Guberman, M. & Seeberger, P. H. Automated Glycan Assembly: A Perspective. *J Am Chem Soc* **141**, 5581–5592 (2019).

15. Gucchait, A. *et al.* Advancing Chemoenzymatic Synthesis and Covalent Immobilization of a Comprehensive Ganglio-glycosphingolipid Library Enables Functional Multiplex Bead Assays. *J. Am. Chem. Soc.* **147**, 36717–36733 (2025).

16. Dhar, C., Sasmal, A. & Varki, A. From 'Serum Sickness' to 'Xenosialitis': Past, Present, and Future Significance of the Non-human Sialic Acid Neu5Gc. *Front. Immunol.* **10**, 807 (2019).

17. Samraj, A. N., Läubli, H., Varki, N. & Varki, A. Involvement of a Non-Human Sialic Acid in Human Cancer. *Front. Oncol.* **4**, 33 (2014).

18. Yu, H. *et al.* Chemoenzymatic Total Synthesis of GM3 Gangliosides Containing Different Sialic Acid Forms and Various Fatty Acyl Chains. *Journal of Organic Chemistry* **86**, 8672–8682 (2021).

19. Hedlund, M., Padler-Karavani, V., Varki, N. M. & Varki, A. Evidence for a human-specific mechanism for diet and antibody-mediated inflammation in carcinoma progression. *Proc. Natl. Acad. Sci. U. S. A.* **105**, 18936–18941 (2008).

20. Fazzari, M., Lunghi, G., Chiricozzi, E., Mauri, L. & Sonnino, S. Gangliosides and the Treatment of Neurodegenerative Diseases: A Long Italian Tradition. *Biomedicines* **10**, (2022).

21. Alpaugh, M. *et al.* Disease-modifying effects of ganglioside GM1 in Huntington's disease models. *EMBO Mol Med* **9**, 1537–1557 (2017).

22. Schneider, J. S. GM1 Ganglioside as a Disease-Modifying Therapeutic for Parkinson's Disease: A Multi-Functional Glycosphingolipid That Targets Multiple Parkinson's Disease-Relevant Pathogenic Mechanisms. *Int J Mol Sci* **24**, (2023).

23. Hegde, M. *et al.* Harnessing potential role of gangliosides in immunomodulation and cancer therapeutics. *Life Sci* **351**, 122786 (2024).

24. Yoon, S., Nakayama, K., Hikita, T., Handa, K. & Hakomori, S. Epidermal growth factor receptor tyrosine kinase is modulated by GM3 interaction with N-linked GlcNAc termini of the receptor. *Proc. Natl. Acad. Sci. U.S.A.* **103**, 18987–18991 (2006).

25. Palomo, A. G. *et al.* Frequent co-expression of EGFR and NeuGcGM3 ganglioside in cancer: it's potential therapeutic implications. *Clin Exp Metastasis* **33**, 717–725 (2016).

26. Hiroshima, M. *et al.* Transient Acceleration of Epidermal Growth Factor Receptor Dynamics Produces Higher-Order Signaling Clusters. *J Mol Biol* **430**, 1386–1401 (2018).

27. Yahi, N., Aulas, A. & Fantini, J. How cholesterol constrains glycolipid conformation for optimal recognition of Alzheimer's beta amyloid peptide (Abeta1-40). *PLoS One* **5**, e9079 (2010).

28. Patel, D. S. *et al.* Influence of Ganglioside GM1 Concentration on Lipid Clustering and Membrane Properties and Curvature. *Biophys J* **111**, 1987–1999 (2016).

29. Jordan, L. R., Blauch, M. E., Baxter, A. M., Cawley, J. L. & Wittenberg, N. J. Influence of brain gangliosides on the formation and properties of supported lipid bilayers. *Colloids Surf B Biointerfaces* **183**, 110442 (2019).

30. Arkhipov, A. *et al.* Architecture and membrane interactions of the EGF receptor. *Cell* **152**, 557–569 (2013).

31. Hedger, G., Shorthouse, D., Koldsø, H. & Sansom, M. S. P. Free Energy Landscape of Lipid Interactions with Regulatory Binding Sites on the Transmembrane Domain of the EGF Receptor. *Journal of Physical Chemistry B* **120**, 8154–8163 (2016).

32. Kawashima, N., Yoon, S. J., Itoh, K. & Nakayama, K. Tyrosine kinase activity of epidermal growth factor receptor is regulated by GM3 binding through carbohydrate to carbohydrate interactions. *J Biol Chem* **284**, 6147–6155 (2009).

33. Malinick, A. S. *et al.* Curvature-tuning membrane mimetics as novel sensing interface to probe affinity fluctuation of bridging integrator 1 protein by SPR. *Biosens. Bioelectron.* **287**, 117713 (2025).

34. Stuart, D. D., Pike, C. D., Malinick, A. S. & Cheng, Q. Characterization of a Charged Biomimetic Lipid Membrane for Unique Antifouling Effects against Clinically Relevant Matrices in Biosensing. *ACS Appl. Mater. Interfaces* **16**, 56447 (2024).

35. Malinick, A. S., Stuart, D. D., Lambert, A. S. & Cheng, Q. Curved Membrane Mimics for Quantitative Probing of Protein-Membrane Interactions by Surface Plasmon Resonance. *ACS Appl. Mater. Interfaces* **16**, 84–94 (2024).

36. Yu, H. *et al.* Chemoenzymatic Synthesis of N-Acetyl Analogues of 9-O-Acetylated b-Series Gangliosides. *Tetrahedron* **142**, (2023).

37. Yu, H., Zhang, L., Yang, X., Bai, Y. & Chen, X. Process Engineering and Glycosyltransferase Improvement for Short Route Chemoenzymatic Total Synthesis of GM1 Gangliosides. *Chemistry – A European Journal* **29**, e202300005 (2023).

38. Schwarzmann, G., Wendeler, M. & Sandhoff, K. Synthesis of novel NBD-GM1 and NBD-GM2 for the transfer activity of GM2-activator protein by a FRET-based assay system. *Glycobiology* **15**, 1302–1311 (2005).

39. Schwarzmann, G. Labeled gangliosides: their synthesis and use in biological studies. *FEBS Lett* **592**, 3992–4006 (2018).

40. Schwarzmann, G. & Sandhoff, K. [26] Lysogangliosides: Synthesis and use in preparing labeled gangliosides. *Methods Enzymol.* **138**, 319–341 (1987).

41. Xu, X. *et al.* Fucosyl-GM1a, an endoglycoceramidase-resistant ganglioside of porcine brain. *J. Biochem.* **141**, 1–7 (2007).

42. Polyakova, S. M. *et al.* New GM1 Ganglioside Derivatives for Selective Single and Double Labelling of the Natural Glycosphingolipid Skeleton. *European J. Org. Chem.* **2009**, 5162–5177 (2009).

43. Lippincott-Schwartz, J., Snapp, E. L. & Phair, R. D. The Development and Enhancement of FRAP as a Key Tool for Investigating Protein Dynamics. *Biophys. J.* **115**, 1146 (2018).

44. Bieberich, E. Sphingolipids and lipid rafts: Novel concepts and methods of analysis. *Chem Phys Lipids* **216**, 114–131 (2018).

45. Crane, J. M. & Tamm, L. K. Role of Cholesterol in the Formation and Nature of Lipid Rafts in Planar and Spherical Model Membranes. *Biophys J.* **86**, 2965–2979 (2004).

46. Falck, E., Patra, M., Karttunen, M., Hyvönen, M. T. & Vattulainen, I. Lessons of Slicing Membranes: Interplay of Packing, Free Area, and Lateral Diffusion in Phospholipid/Cholesterol Bilayers. *Biophys. J.* **87**, 1076 (2004).

47. Goose, J. E. & Sansom, M. S. P. Reduced Lateral Mobility of Lipids and Proteins in Crowded Membranes. *PLoS Comput. Biol.* **9**, e1003033 (2013).

48. Schnaar, R. L., Sandhoff, R., Tiemeyer, M. & Kinoshita, T. Glycosphingolipids. *Essentials of Glycobiology* (2022)

49. Guo, Z. The Structural Diversity of Natural Glycosphingolipids (GSLs). *J. Carbohydr. Chem.* **41**, 63–154 (2022).

50. Sonnino, S. & Chigorno, V. Ganglioside molecular species containing C18- and C20-sphingosine in mammalian nervous tissues and neuronal cell cultures. *Biochim. Biophys. Acta* **1469**, 63–77 (2000).

51. Lyu, Y. *et al.* Effect of GM1 concentration change on plasma membrane: molecular dynamics simulation and analysis. *Phys Chem Chem Phys* **26**, 12552–12563 (2024).

52. Manna, M. *et al.* Long-chain GM1 gangliosides alter transmembrane domain registration through interdigitation. *Biochim Biophys Acta Biomembr* **1859**, 870–878 (2017).

53. Machan, R. & Hof, M. Lipid diffusion in planar membranes investigated by fluorescence correlation spectroscopy. *Biochim Biophys Acta* **1798**, 1377–1391 (2010).

54. Sipione, S., Monyror, J., Galleguillos, D., Steinberg, N. & Kadam, V. Gangliosides in the Brain: Physiology, Pathophysiology and Therapeutic Applications. *Front Neurosci* **14**, 572965 (2020).

55. Sezgin, E., Levental, I., Mayor, S. & Eggeling, C. The mystery of membrane organization: composition, regulation and roles of lipid rafts. *Nat Rev Mol Cell Biol* **18**, 361–374 (2017).

56. Labrada, M. *et al.* GM3(Neu5Gc) ganglioside: an evolution fixed neoantigen for cancer immunotherapy. *Semin Oncol* **45**, 41–51 (2018).

57. Hayashi, N. *et al.* Detection of N-glycolyated gangliosides in non-small-cell lung cancer using GMR8 monoclonal antibody. *Cancer Sci* **104**, 43–47 (2013).

58. Malinick, A. S., Stuart, D. D., Lambert, A. S. & Cheng, Q. Curved Membrane Mimics for Quantitative Probing of Protein-Membrane Interactions by Surface Plasmon Resonance. *ACS Appl Mater Interfaces* **16**, 84–94 (2024).

59. Duan, J., Linman, M. & Cheng, Q. Ultrathin Calcinated Films on a Gold Surface for Highly Effective Laser Desorption/Ionization of Biomolecules. *Anal. Chem.* **82**, 5088–5094 (2010).

60. Meuillet, E. J., Mania-Farnell, B., George, D., Inokuchi, J. I. & Bremer, E. G. Modulation of EGF Receptor Activity by Changes in the GM3 Content in a Human Epidermoid Carcinoma Cell Line, A431. *Exp. Cell Res.* **256**, 74–82 (2000).

61. Björkelund, H., Gedda, L. & Andersson, K. Comparing the Epidermal Growth Factor Interaction with Four Different Cell Lines: Intriguing Effects Imply Strong Dependency of Cellular Context. *PLoS One* **6**, e16536 (2011).

62. Özcan, F., Klein, P., Lemmon, M. A., Lax, I. & Schlessinger, J. On the nature of low- and high-affinity EGF receptors on living cells. *Proc. Natl. Acad. Sci. U. S. A.* **103**, 5735–5740 (2006).

63. Kuo, W. T. *et al.* Quantitative Analysis of Ligand-EGFR Interactions: A Platform for Screening Targeting Molecules. *PLoS One* **10**, e0116610 (2015).

64. Macdonald, J. L. & Pike, L. J. Heterogeneity in EGF-binding affinities arises from negative cooperativity in an aggregating system. *Proc. Natl. Acad. Sci. U. S. A.* **105**, 112–117 (2008).

65. Cytiva. *Biacore Sensor Surface Handbook*. (Cytiva, Uppsala, Sweden, 2022).

66. Fischer, M., Leech, A. P. & Hubbard, R. E. Comparative assessment of different histidine-tags for immobilization of protein onto surface plasmon resonance sensorchips. *Anal. Chem.* **83**, 1800–1807 (2011).

Chapter 5: Native Membranes on a Chip for Probing Lateral Interaction Effects on Transmembrane Protein Binding and Activation

5.1 Introduction

Accurately assessing the binding behavior of transmembrane proteins and gaining mechanistic insights into their interactions with their membrane environment requires the examination of the protein at full length and functionality.[1] Traditionally, studies of full transmembrane proteins have been primarily limited to cell studies due to the inherent difficulties to expressing, isolating, and recapturing them on an artificial substrate.[2] The main limitation of cell studies is in the isolation of specific experimental variables due to the heterogeneity of cellular membrane environments.[3] Additionally, many favored analytical techniques are incompatible with whole cell studies. For these reasons, there have been numerous attempts to collect transmembrane proteins and reconstitute them on biosensing platforms. This is usually done through the solubilization and capture in lipid vesicles or nanodiscs using detergent-based methods that risk damaging the protein's structure.[4–6] These systems also generally lacking the tunability and size for large-scale diffusivity necessary to examine the effects of lipid environment on protein-protein interactions.[7,8]

Supported lipid bilayers (SLB) however, lend themselves very well to a range of analytical techniques,[9] including SPR,[10,11] fluorescence microscopy, quartz crystal microbalance (QCM),[12] and atomic force microscopy (AFM),[13] but they struggle with the functional and fluid integration of large transmembrane proteins due to limited submembrane spacing[9,14] and challenges with maintaining protein structure and orientation

during the rupture process.[14] The typical vesicle fusion to hydrophilic substrates, solvent-assisted lipid bilayer formation, and Langmuir-Blodgett depositions all carry these fundamental limitations without specific adaptations. Fortunately, there have been many advancements that have greatly increased the feasibility of building more function cell membrane mimics on a chip.[15] The use of cell-free protein synthesis methods (CFPS) for direct expression of transmembrane proteins into pre-formed SLBs in the absence of detergents has been suggested and demonstrated for a considerable amount of time, but have been generally limited to smaller channel proteins that don't require a large submembrane space to accommodate their insertion and function.[16,17] More recent works have utilized tethers and polymer cushions to provide additional space to address these limitations.[18,19] However, these methods come with their own limitations of potentially poor protein density on the surface and a lack of control of protein orientation, with both of these factors limiting the viability of this method for SPR analysis.[20]

Another alternative for studying the function of membrane proteins is by collecting cell membrane fractions and reconstituting them on a planar surface for biosensing (Figure 5.1). This field was largely pioneered initially by Höök group[21] followed by the Daniel group at Cornell over the past decade where they've demonstrated numerous methods for the induction, collection, and capture of these cell "blebs". Furthermore, they've examined and confirmed the orientation and fluidity of capture membrane proteins using fluorescent methods.[21] Capture has been achieved on glass,[22] polyethylene glycol (PEG) cushions,[23] and polyelectrolyte brushes,[24] with each offering distinct advantages in terms of fluidity, protein function, compositional control, and other experimental considerations.

Additionally, cells can be induced to produce great amounts of proteins of interest, including those with modifications useful for downstream applications or mutations reflecting those found in disease states.

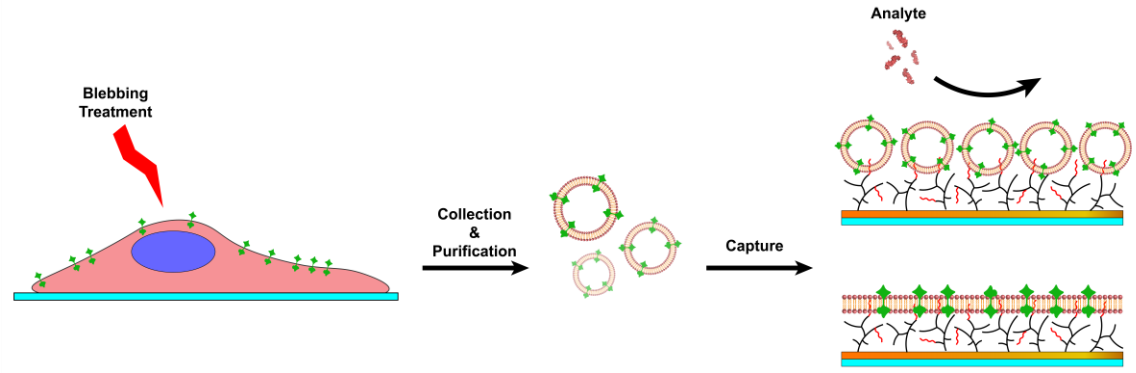

Figure 5.1. Scheme showing the formation of cell blebs, their isolation from the cellular media, and their reconstitution on a solid substrate for biosensing applications.

Considering the flexibility of this method from these many angles, we determined that it would be ideal for the generation of an EGFR-integrated lipid bilayer biointerface for use with SPR. This project is an extension of the work presented in chapter 4 of this dissertation, and the biointerface will be redeveloped to probe the effects of gangliosides on the full-length EGFR protein. This is necessary as the lone extracellular domain may lack the key residues or conformational properties to accurately assess the regulatory mechanism of gangliosides, a theory that is supported by existing computational assessments.[25] This chapter outlines our preliminary work toward achieving these goals with a focus on the characterization and optimization of bleb formation, collection, and composition for eventual integration into a new biosensing platform.

5.2 Experimental Methods

Materials and Reagents.

HeLa and A431 cell lines were purchased from the American Type Culture Collection (ATCC, Manassas, VA). Cells were cultured in Gibco™ Dulbecco's Modified Eagle Medium (DMEM) containing high glucose, GlutaMAX™ supplement, and pyruvate purchased from Thermo Fisher Scientific (Waltham, MA). The media was supplemented with 1% penicillin/streptomycin, and 10% fetal bovine serum (Fisherbrand™, Research Grade, Waltham, MA). Cells were cultured in 25 mL or 75 mL culture flasks with vented caps purchased from VWR (Radnor, PA). For Annexin V staining and imaging, cells were grown on Lab-Tek II Chamber Slides (Grand Rapids, MI). Alexa Fluor 488 conjugated Annexin V was purchased from Thermo Fisher Scientific. A mini stainless steel extruder kit, and 200 nm polycarbonate thin film membranes used were purchased from Avanti Polar Lipids (Alabaster, Al). A Halt™ protease and phosphatase inhibitor cocktail and EGFR polyclonal antibody (PA1-1110) were purchased from Thermo Fisher Scientific. For western blotting, an IRDye 800CW goat anti-rabbit secondary antibody was purchased from LICORbio (Lincoln, NE). Low fluorescence PVDF blotting membranes were purchased from Bio-Rad (Hercules, CA). For SPR analysis, a series S sensor chip L1 was purchased from Cytiva Life Sciences (Uppsala, SE).

Chemical and Serum Starvation Blebbing.

For HeLa cells, 1.5 x 10^6 cells were passaged to 75 cm^2 cell culture flasks two days prior to blebbing and collection. For A431 cells, 1.5 x 10^6 cells were passaged to T75 flasks four days prior to blebbing and collection. However, fresh media was added after three days to ensure the cells were healthy prior to blebbing. On the day of blebbing, the flasks were first washed once with pre-warmed 1x phosphate buffered saline (PBS). Next, serum starving flasks were washed twice with serum-free DMEM, before adding 3 mL of serum-free DMEM and placing back into the incubator for the treatment period. For chemical blebbing, the same process was carried out with serum-free DMEM replaced by chemical blebbing buffer (10 mM HEPES, 150 mM NaCl, 2.0 mM $CaCl_2$, 25 mM Formaldehyde (FA), and 4 mM dithiothreitol (DTT). After the treatment time was completed, flasks were pulled from the incubator, and the contents were transferred to 1.5 mL microfuge tubes. These were centrifuged at 200 RPM and 4 ºC for 5 minutes to remove large cellular debris before the supernatant was transferred to fresh tubes and stored at -80 ºC.

Annexin V Staining and Imaging.

Two days prior to imaging, 1.5 x 10^5 cells were passaged to each chamber on the Lab-Tek II slides and placed into a CO_2 incubator at 37 ºC. On the day of analysis, chambers were washed three times with 1 mL of 1x PBS pre-warmed to 37 ºC. Chemical blebbing and serum starving wells were rinsed one time with pre-warmed chemical blebbing buffer or serum-free DMEM respectively. Next 1 mL of the respective solution was added to each well and they were placed back in the incubator. Control wells were prepared in a similar

manner, though using standard DMEM supplemented with fetal bovine serum (FBS). After the treatment time was completed, wells were rinsed 3 times with room temperature annexin V binding buffer (10 mM HEPES, 150 mM NaCl, 2.0 mM $CaCl_2$, pH 7.4). Next, 0.5 mL of annexin V binding buffer containing 5 μL of the annexin V conjugate were added to each well, excluding the negative control which was exposed to no annexin V. Wells were then wrapped in foil and brought to an LSM 880 inverted confocal microscope (Zeiss, Oberkochen, DE) for analysis. Prior to imaging, excess annexin V was removed by rinsing twice with 1 mL of HEPES buffered saline (HBS, pH 7.4). HeLa cells were imaged only after 3 hours of treatment, while A431 cells were imaged after 2, 4, and 6 hours of treatment. Brightfield and fluorescence images were processed and overlayed using the Fiji package for ImageJ.

Osmotic Shock Blebbing.

HeLa and A431 cells were passaged into T75 flasks and allowed to grow as was described for the chemical and starvation treatments. When ready for collection, the cells were washed once with pre-warmed 1x PBS. Next, they were washed once with a pre-warmed hypotonic PBS buffer (5% 1x PBS in water), before adding more hypotonic PBS and incubating for 15 minutes at 37 ºC. Next, the cells were washed once with pre-warmed vesiculation buffer (100 mM NaCl, 50 mM Na_2HPO_4, 5 mM KCl, and 0.5 mM $MgSO_4$, pH 8.5). Vesiculation buffer containing a protease and phosphatase inhibitor cocktail was added to the flasks before 20 minutes of shaking at room temperature, followed by 1 hour of shaking at 37 ºC. Following this, the flasks were decanted into pre-cooled centrifuge tubes that were spun at 150 xg for 5 minutes at 4 ºC to remove large debris. The supernatant

was transferred to new tubes, spun down at 17,000 xg for 30 minutes at 4 ºC. The pellet containing the membrane fractions was then resuspended in 1x HBS and centrifuged again with the same parameters. The pellet was resuspended once more in 1x HBS, aliquoted, and stored at -80 ºC.

HeLa Cell Lysis and Western Blotting.

For lysis, HeLa cells were first grown in a T75 flask to approximately 75% confluency. The cells were washed three times with ice-cold PBS. Next, 2 mL of cold NP-40 lysis buffer (50 mM Tris-HCl, 150 mM NaCl, 1% NP-40, 1 mM EDTA) containing the complete inhibitor cocktail was added to the flask, and the cells were scraped. The solution was transferred to two ice-cold 1.5 mL centrifuge tubes and placed on ice for 30 minutes with 5 seconds of vigorous vortexing performed every 10 minutes. The samples were then centrifuged at 16,000 xg for 20 minutes, before the supernatant was collected and stored at -80 ºC prior to analysis.

Lysate and bleb samples were prepared for SDS-PAGE separation by mixing 35 µL of the samples with 12.5 µL of 4x Laemmli buffer, and 2.5 µL of 100 mM DTT for maximum protein concentration. Additionally, ½ concentration samples were prepared with 17.5 µL of sample, 17.5 µL of nanopure water, 12.5 µL of 4x Laemmli buffer, and 2.5 µL of 100 mM DTT. Samples were heated at 90 ºC for 5 minutes, allowed to cool and separated at 60 V for the 5% acrylamide stacking gel, and 105 V for the 8% acrylamide resolving gel. Protein bands were transferred to a PVDF membrane in Towbin buffer (25 mM Tris, 192 mM glycine, 20% MeOH, 0.050% SDS, pH 8.3). After transfer, the

membrane was washed with distilled water and dried on a filter paper for 10 minutes at 37 ºC. After rewetting with methanol followed by rinsing with PBS, the membrane was blocked with 5% BSA in PBS for 1 hour. The primary rabbit anti-human EGFR antibody (1:10,000 dilution) in PBS containing 0.2 (v/v) tween-20 (PBS-T) was added and incubated overnight at 4 ºC. The next morning, the membrane was rinsed 5 times with PBS-T and the goat anti-rabbit secondary antibody (1:20,000 dilution) was incubated for 1 hour prior to rinsing 5 times with PBS-T. The blot was then imaged using the 800 nm channel of a LICOR Fc Odyssey imager.

Nanoparticle Tracking Analysis of Blebs

Bleb concentration and size characterization was performed using a Nanosight NS300 (Malvern Panalytical, Malvern, UK) equipped with a 405 nm laser. A431 chemical and starvation blebs were diluted 25-fold in 1x HBS prior to analysis. Osmotic shock blebs were diluted 10-fold, extruded through a 200 nm extrusion filter (15 passes), and further diluted another 10-fold prior to analysis. Five replicates were collected for each sample, and the sizing results were averaged. Each measurement was conducted for 30 seconds at a flow rate of 100 (a.u.) and a flow cell temperature of 25 ºC.

SPR Methodology for Osmotic Bleb Capture

The SPR experiment was conducted using a Biacore 1K SPR System (Cytiva, Marlborough, MA) with Biacore Insight Control Software Version 6.0.7.1750 and a Series S Sensor Chip L1. Data analysis was performed with Biacore Insight Evaluation Software Version 6.0.7.1750. The running buffer used was 1x HBS with a flow rate of 30 µL/min.

Prior to capture, the surface was cleaned and prepared with three 30-second injections of 20 mM CHAPS. The A431 blebs were diluted 10-fold and extruded to 200 nm before being captured on the surface for 1 hour at a flow rate of 2 μL/min. After rinsing the flow system twice with running buffer, the surface was further passivated with 1% (w/v) BSA in HBS for 5 minutes at a flow rate of 10 μL/min. Anti-EGFR antibodies were injected at a concentration of 10 μg/mL for 120 seconds at a flow rate of 10 μL/min.

5.3 Results and Discussion

For our initial attempts to generate cell membrane blebs, HeLa cells were selected due to their quick growth and division allowing for rapid testing of blebbing conditions. Previous work had also utilized HeLa cells for blebbing, providing a point of comparison.[26] Furthermore, HeLa cells do contain a physiologically average amount of EGFR, with general estimates placing the density at ~3-5 x 10^4 receptors per cell.[27–29] This will provide another point of comparison for the later use of A431 cells with highly upregulated EGFR production that have estimated densities of 2-3 x 10^6 receptors per cell.[30,31] Generation of cell blebs was first conducted using two common methods. Serum starvation is achieved by simple removal of fetal bovine serum from media, resulting in cellular stress and eventual apoptosis coinciding with an increased release of extracellular vesicles from the plasma membrane.[32] Chemical blebbing can be induced in a number of ways including activation of myosin phosphatase inhibition, disruption of actin structure with cytochalasin D, or use of apoptosis inducers, but these methods require use of specialized materials.[33,34] The use of formaldehyde (FA) and dithiothreitol (DTT) is a more accessible and established alternative. These chemicals work synergistically with FA acting to crosslink

the actin network of the cell cortex and disrupt its interactions with the cell membrane above.[35] The DTT acts as a reducing agent, cleaving the disulfide bonds of the proteins that link the cortex to the cell membrane. With these forces acting together, the cellular membrane is greatly destabilized, resulting in a high degree of shedding into the surrounding media.

These distinct processes were monitored using fluorescence microscopy of an Alexa Fluor 488-conjugated apoptosis reporter commonly used in flow cytometry called annexin V. Apoptosis is monitored through changes to membrane composition, as phosphatidylserine (PS), typically confined to the inner leaflet, migrates to the outer leaflet and becomes available for binding by annexin V during this process.[36] Figure 5.2 shows overlaid brightfield and fluorescence images of HeLa cells before and after 3 hours of serum starvation as well as chemical induction, revealing clear differences in the blebbing process. The serum starved cells show highly localized signal, indicating that only a portion of the cells have begun apoptosis at the 3-hour mark. By comparison, chemical induction appears to act quickly and ubiquitously, showing clear annexin V binding to every cell.

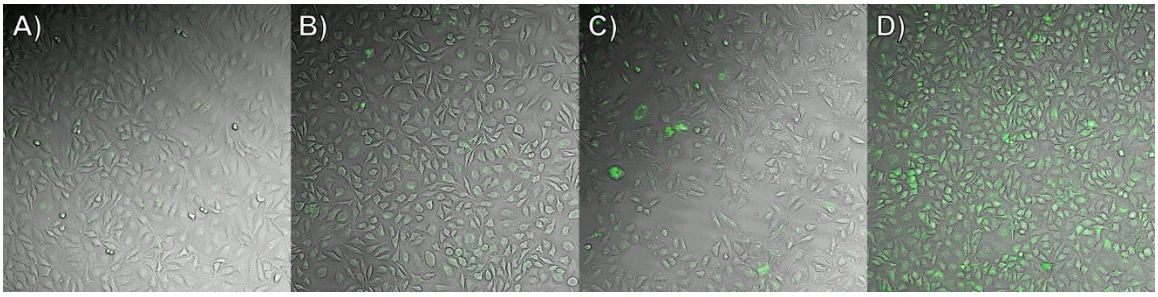

Figure 5.2. Overlaid brightfield and fluorescence images of annexin V-stained HeLa cells. A) Untreated control (no annexin V). B) Healthy cells. C) 3-hour serum-starved. D) 3-hour chemical treatment.

Though bleb formation was more or less confirmed from these methods, each does present some concerning considerations for its use in downstream applications. The downside to chemical induction with FA and DTT is obvious – the structure of the EGFR is likely to be irreversibly altered through crosslinking one of its many interacting nearby proteins, and through cleavage of important structural disulfide bonds. This would throw into question the validity of results generated by future sensing experiments. Serum starvation has other practical limitations, with long starvation times being required to generate a sizeable amount of membrane blebs being one. During this long starvation, the EGFR is also at risk of degradation by extracellular proteases due to the lack of inhibitors such as α2-macroglobulin found in FBS.[37] Furthermore, EGFR in membrane blebs is at risk of shedding by membrane-associated proteases such as A Disintegrin and Metalloproteases (ADAMs) and has no pathway for replacement.[38]

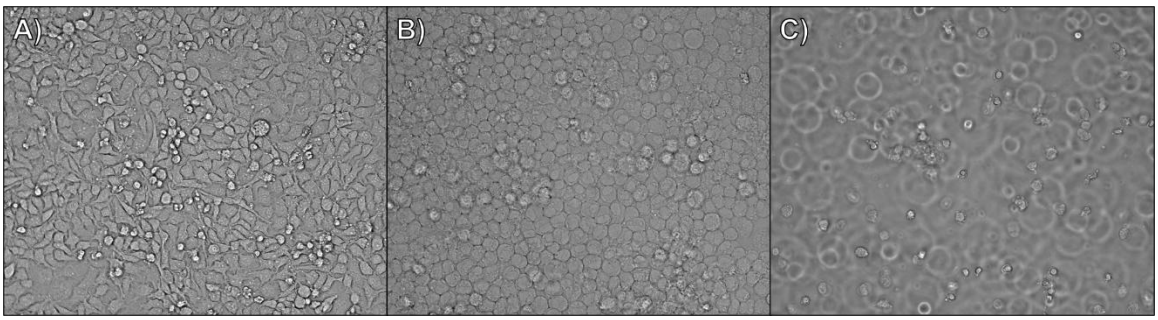

Figure 5.3. Brightfield images of HeLa cells at different stages of the osmotic shock blebbing process. A) Pre-treatment. B) In hypotonic PBS. C) In vesiculation buffer after shaking.

Due to these concerns, we thought it prudent to attempt one additional method that could produce membrane fractions more rapidly and in higher yields without use of harsh chemicals – osmotic shock (Figure 5.3). In this method adapted from Cohen et al.,[39] cells are first exposed to a hypotonic buffer, causing a large influx of water to the interior of the

cell that mechanically stresses and weakens the actin cortex (Figure 5.3B).[40] This is followed with a high pH (8.5) vesiculation buffer that further weakens the actin network,[41] when combined with vigorous shaking causes massive disruption and shedding of the cell membrane (Figure 5.3C). Not only is this method relatively fast and chemically gentle, but it also produces larger blebs that can be easily removed from solution through centrifugation, allowing for buffer exchange and concentration.

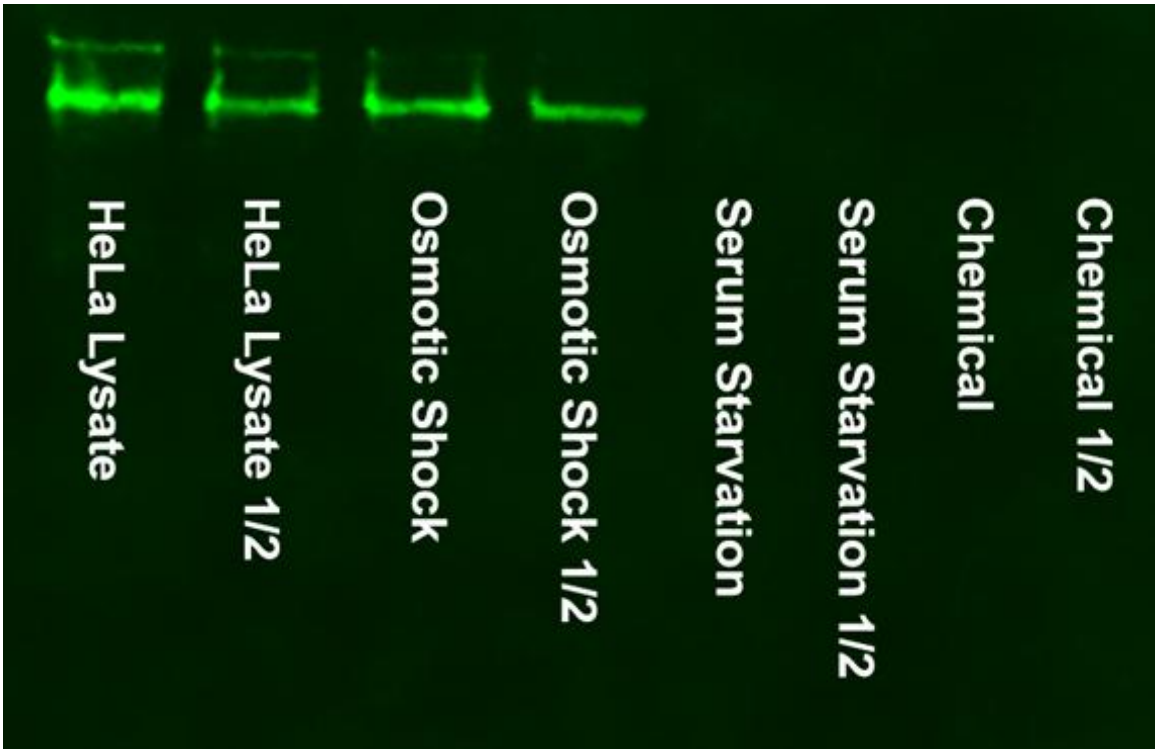

Figure 5.4. Western blot of HeLa cell lysates and blebs samples. No EGFR was observed for the serum starved or chemical treated blebs. Samples for loading into the lanes were prepared either in the maximum possible concentration of lysate/bleb solution or with one-half of that amount.

With blebs collected with all three methods, we next assessed their concentrations of EGFR compared to a HeLa lysate using a western blot (Figure 5.4). The bleb measurements were taken agnostic of total protein loading to compare them without use of

additional challenging purification and concentration steps. The wells were loaded with the maximum volume of the bleb samples possible as well as half of that concentration. Unsurprisingly, it was found that EGFR was only detectable in the lysate and the osmotic shock blebs. The superior results from the osmotic shock blebs are likely from an increase in total generation of blebs, a substantially reduced total volume of solution from each flask (100 µL vs 1 mL per T75 flask), and is supported by another study showing blebs produced by FA/DTT chemical induction do not contain EGFR.[42]

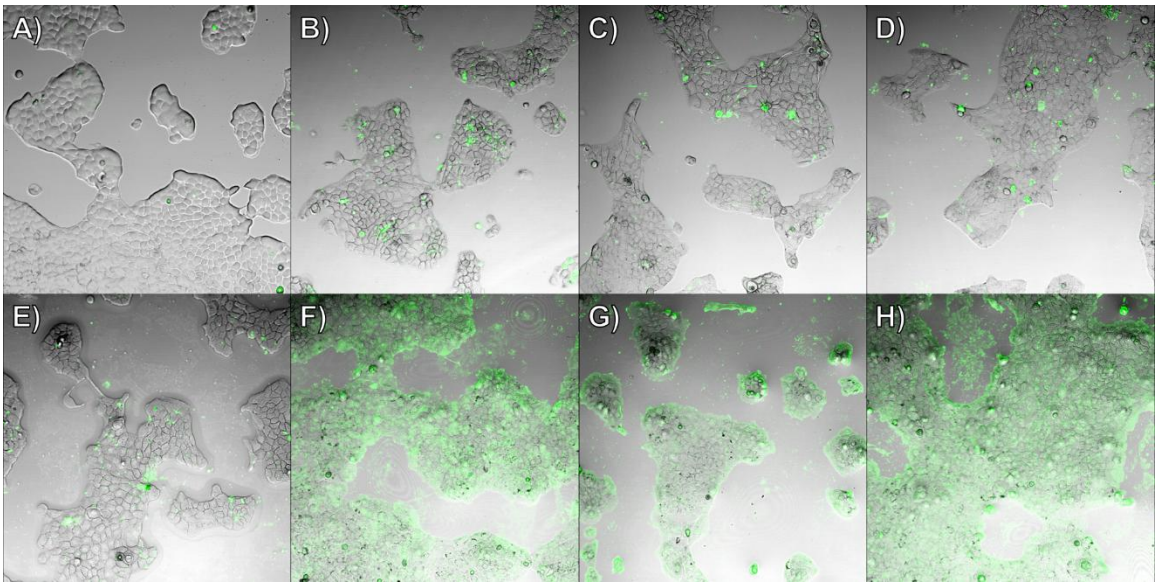

Figure 5.5. Overlayed brightfield and fluorescence images of A431 cells treated with annexin V. A) No annexin V control. Cells after 2 hours (B), 4 hours (C), and 6 hours (D) of serum starvation. E.) Healthy cells. Cells after 2 hours (F), 4 hours (G), and 6 hours (H) of chemical treatment.

With the blebbing methods and the low total yield of EGFR under even ideal conditions established, all future experiments were changed to use A431 cells. Using these, apoptosis analysis was repeated with annexin V staining (Figure 5.5). Serum starvation produced a similar result of highly localized staining, but interestingly a substantial difference in the number of apoptotic cells was not observed between 2 and 6 hours. Some

studies have indicated that A431 cells are made more resistant to serum starvation conditions by producing their own transforming growth factor alpha (TGFα), a ligand that activates their overexpressed EGFR to maintain receptor phosphorylation and promote cellular survival.[43] Alternatively, the different origins of the cell lines (epidermoid for A431 and cervical for HeLa) could result in a different presentation of the PS lipids to the surface during starvation. Chemical induction, however, produced a much more similar result to the HeLa cells, with ubiquitous labelling of the cultured cells regardless of treatment time over the 2–6-hour range. Finally, the osmotic shock procedure was repeated using the A431 cells (Figure 5.6). The cells showed a strong swelling response to the hypotonic buffer (Figure 5.6B) and obvious disruption after addition of the vesiculation buffer and shaking (Figure 5.6D). One intriguing difference from the same treatment of HeLa cells is that the A431 cells showed formation of long fibrils. Presumably these are vesicles/blebs that agglomerated due to vigorous shaking inducing trans-interactions of membrane proteins and glycans that are prevalent in epithelial cells.[44]

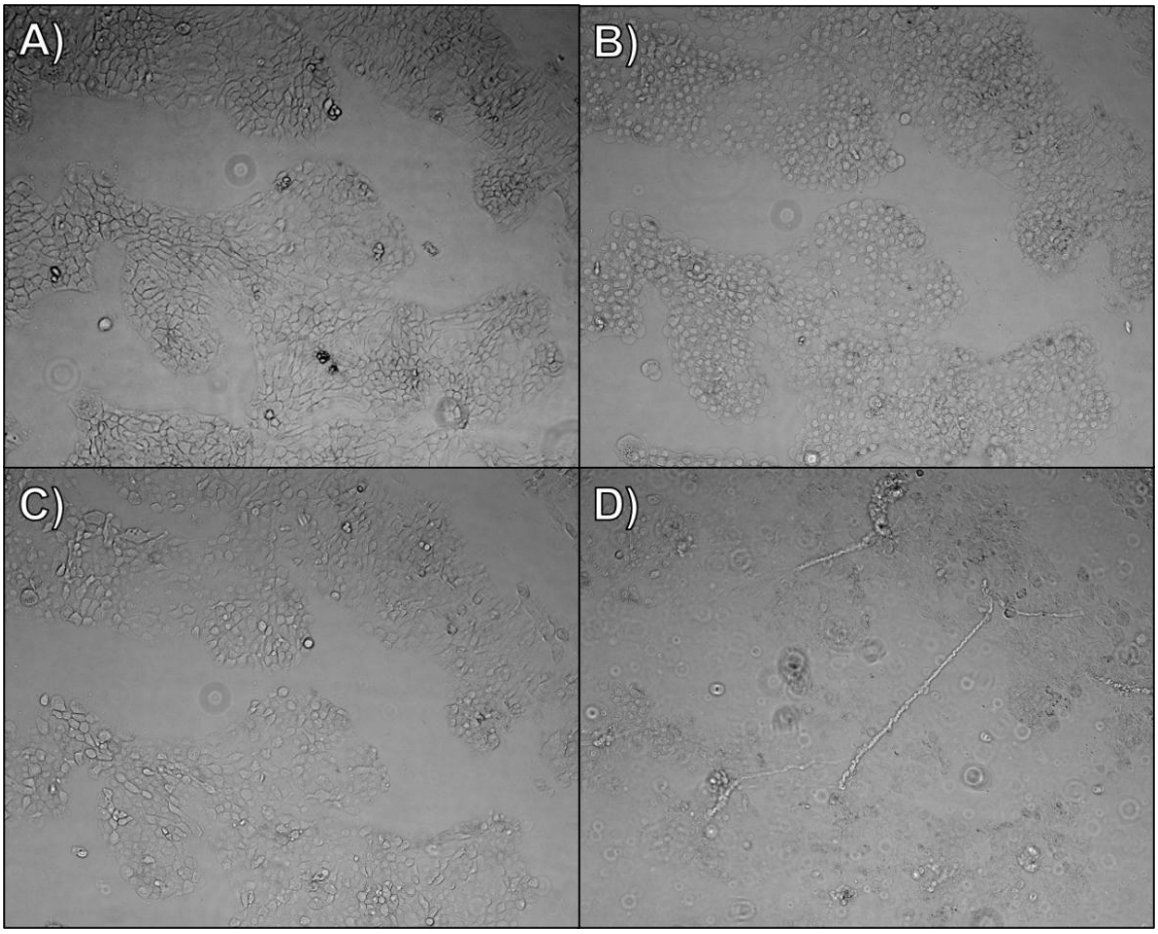

Figure 5.6. Brightfield images of A431 cells at different stages in the osmotic shock process. A) Pre-treatment. B) Hypotonic PBS. C) Vesiculation buffer. D) Vesiculation buffer after shaking.

The A431 cell blebs obtained from the three methods were next compared and characterized for both their concentrations and size distribution using nanoparticle tracking analysis (NTA). Serum starvation blebs (Figure 5.7A) showed the smallest average size, very distinct peaks in the distribution, and the lowest overall concentration at 8.53 x 10^8 particles/mL. Chemically induced blebs (Figure 5.7B) were larger, more heterogeneous, and had approximately twice the concentration of particles. Blebs formed by osmotic shock are almost entirely significantly larger than can be measure by our NTA instrument, which performs optimally below 1 μm, so the osmotic shock blebs were extruded through a 200 nm filter to allow for more accurate comparison to the other methods. Extrusion has the additional benefit of better compatibility with downstream formation of SLBs, with the high elastic stress found in small and highly curved vesicles promoting rupture on the sensing substrate.[45] Due to the extrusion, the osmotic shock blebs were the most normally distributed in size (Figure 5.7C). Additionally, these particles showed a concentration significantly higher than the chemically induced blebs, as was expected.

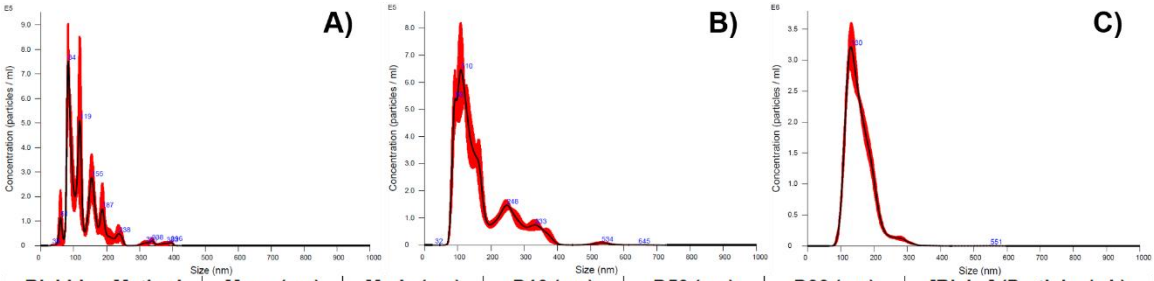

Blebbing Method	Mean (nm)	Mode (nm)	D10 (nm)	D50 (nm)	D90 (nm)	[Blebs] (Particles/mL)
Serum Starving	129.3 ± 4.5	94.5 ± 8.4	77.1 ± 4.5	112.9 ± 3.4	195.7 ± 12.7	8.53 x 10^8
Chemical	169.2 ± 2.0	98.6 ± 5.3	93.5 ± 2.3	140.4 ± 4.1	298.6 ± 4.7	1.54 x 10^9
Osmotic Shock	156.1 ± 1.1	130.3 ± 3.3	114.7 ± 0.8	149.0 ± 1.8	203.0 ± 2.6	2.47 x 10^{10}

Figure 5.7. Nanoparticle tracking analysis results comparing the size of A431 blebs generated through A) serum starvation, B) chemical treatment, C) and osmotic shock. Note the osmotic shock blebs were extruded through a 200 nm filter prior to analysis, and table shows the dilution-adjusted particle concentrations.

Just as with the HeLa blebs, the osmotic shock blebs were identified as the optimal choice for downstream sensing with A431 cells. With these, preliminary testing of their use for biosensing was begun using a commercially available lipophilic SPR chip. The extruded A431 osmotic shock blebs were immobilized by 1 hour of flow-through on the surface, achieving a capture level of ~3500 RUs (Figure 5.8A). This is lower than the expected shift of ~5000 RUs for a fused bilayer and the 10,000 RUs expected for whole liposomes.[46] The small shift indicates poor coverage of the lipids that, when tightly packed, result in greater mass shifts than seen with surface saturation with other biomolecules. It is possible that the extruded blebs contain a great deal of free proteins, sugars, or DNA that are blocking lipid binding and preventing formation of a continuous, densely packed, lipid bilayer.

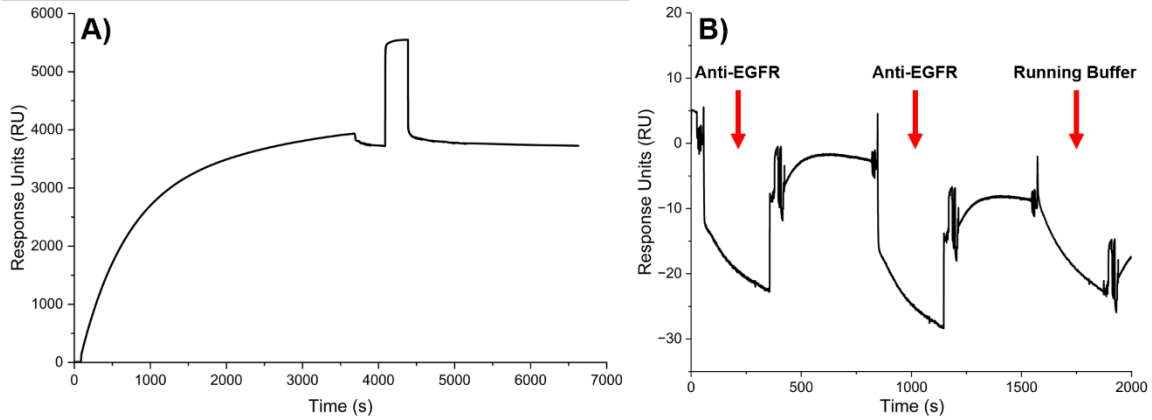

Figure 5.8. A) Sensorgram showing the capture of A431 osmotic shock blebs on a Biacore L1 chip, followed by passivation with BSA that showed very little binding. B) Unstable capture of the blebs leads to consistent rinse-off during injections, potentially obscuring detection of anti-EGFR binding.

To assess whether the surface was fully saturated as well as to reduce nonspecific binding in following tests, a solution of 1% bovine serum albumin (BSA) was injected for 5 minutes, showing a small shift of ~100 RUs. However, it appears that the BSA was largely removed during the following rinsing period, indicating weak attachment. Furthermore, any injections following this rinsing period, regardless of flow rate, resulted in a reduction of bound material. This can be observed in Figure 5.8B, where 10 µg/mL solutions of a polyclonal anti-EGFR antibody were injected over the surface resulting in a negative net shift. Buffer injections under the same conditions showed a similar downward shift indicating that the antibodies were not binding to surface-captured EGFR to a significant degree. Taken in their totality, these results indicate that this capture method did not result in a significant amount of EGFR immobilization on the surface. In the future, additional sample cleanup steps and other capture methodologies will need to be explored to address these challenges.

5.4 Conclusion

In this chapter, preliminary work for the generation of full-length EGFR-containing cell membrane blebs for use with downstream biosensing techniques is presented. The formation of blebs using three distinct methods was first explored using HeLa cells due to their rapid growth rate. Serum starvation and chemical induction of blebbing presented many concerns in terms of protein quantity and quality as well as ease of purification. Osmotic shock resolved these potential issues with rapid and thorough disruption of cellular membranes, gentle chemical conditions, and simple purification schemes. As

predicted, the EGFR concentration was shown to be below detectable levels in a western blot for both the serum starvation and chemical induction blebs, but not for the osmotic shock blebs. With methods established, collection was repeated using A431 cells that show greatly enhanced production of EGFR. Outcomes were similar to those with HeLa cells, excluding longer starvation times being necessary for the A431 cells to begin apoptosis.

Collected A431 blebs were next quantified and characterized using nanoparticle tracking analysis. Serum starvation resulted in the lowest concentration of blebs relative to the treatment time while chemical induction produced a more uniform distribution of bleb sizes and approximately twice the concentration. Osmotic shock blebs were extruded to a comparable size range and had a concentration more than 10 times greater than the chemical induction blebs, heavily indicating better compatibility with biosensing applications. This method was then used for preliminary SPR testing for response to the binding of an anti-EGFR antibody. However, poor attachment of the blebs to a commercial SPR sensing chip obscured binding results. Furthermore, an unexpectedly low binding shift for the capture indicated that lipid and EGFR loading to the surface may have been insufficient. Further work will be needed to optimize the preparation of blebs, and methods for their attachment to the sensing surface to achieve the desired analysis of the binding kinetics of full-length EGFR to its natural substrates. Further-reaching goals will include the integration of synthetic gangliosides into the bleb-derived biointerfaces for investigation of their effects on the binding behavior of the protein.

5.5 References

1. Piper, S. J., Johnson, R. M., Wootten, D. & Sexton, P. M. Membranes under the Magnetic Lens: A Dive into the Diverse World of Membrane Protein Structures Using Cryo-EM. *Chem. Rev.* **122**, 13989–14017 (2022).

2. Lin, S. H. & Guidotti, G. Chapter 35 Purification of Membrane Proteins. *Methods Enzymol.* **463**, 619–629 (2009).

3. Meyer, C. *et al.* Designer artificial environments for membrane protein synthesis. *Nature Communications* **16**, 4363 (2025).

4. Kotov, V. *et al.* High-throughput stability screening for detergent-solubilized membrane proteins. *Scientific Reports* **9**, 10379 (2019).

5. Ren, Q. *et al.* DeFrND: detergent-free reconstitution into native nanodiscs with designer membrane scaffold peptides. *Nature Communications* **16**, 7973 (2025).

6. Zhou, Z. *et al.* Advances in solubilization and stabilization techniques for structural and functional studies of membrane proteins. *PeerJ* **13**, e19211 (2025).

7. Koh, Y. H., Kim, S. J. & Roh, S. H. Unraveling membrane protein localization and interactions in nanodiscs. *FEBS Lett.* **599**, 512–529 (2025).

8. Rouck, J. E., Krapf, J. E., Roy, J., Huff, H. C. & Das, A. Recent Advances in Nanodisc Technology for Membrane Proteins Studies (2012–2017). *FEBS Lett.* **591**, 2057 (2017).

9. Castellana, E. T. & Cremer, P. S. Solid supported lipid bilayers: From biophysical studies to sensor design. *Surf. Sci. Rep.* **61**, 429–444 (2006).

10. Stuart, D. D., Pike, C. D., Malinick, A. S. & Cheng, Q. Characterization of a Charged Biomimetic Lipid Membrane for Unique Antifouling Effects against Clinically Relevant Matrices in Biosensing. *ACS Appl. Mater. Interfaces* **16**, 56447 (2024).

11. Malinick, A. S. *et al.* Curvature-tuning membrane mimetics as novel sensing interface to probe affinity fluctuation of bridging integrator 1 protein by SPR. *Biosens. Bioelectron.* **287**, 117713 (2025).

12. Parkkila, P., Elderdfi, M., Bunker, A. & Viitala, T. Biophysical Characterization of Supported Lipid Bilayers Using Parallel Dual-Wavelength Surface Plasmon Resonance and Quartz Crystal Microbalance Measurements. *Langmuir* **34**, 8081–8091 (2018).

13. Mingeot-Leclercq, M. P., Deleu, M., Brasseur, R. & Dufrêne, Y. F. Atomic force microscopy of supported lipid bilayers. *Nature Protocols* **3**, 1654–1659 (2008).

14. Girard-Egrot, A. P. & Maniti, O. Why Do Tethered-Bilayer Lipid Membranes Suit for Functional Membrane Protein Reincorporation? *Applied Sciences* **11**, 4876 (2021).

15. Selivanovitch, E., Ostwalt, A., Chao, Z. & Daniel, S. Emerging Designs and Applications for Biomembrane Biosensors. *Annual Review of Analytical Chemistry* **17**, 339–366 (2024).

16. Debnath, D. K. & Otzen, D. E. Cell-free synthesis and folding of transmembrane OmpA reveals higher order structures and premature truncations. *Biophys. Chem.* **152**, 80–88 (2010).

17. Soranzo, T., Martin, D. K., Lenormand, J. L. & Watkins, E. B. Coupling neutron reflectivity with cell-free protein synthesis to probe membrane protein structure in supported bilayers. *Scientific Reports 2017 7:1* **7**, 3399- (2017).

18. Chadli, M. *et al.* New Tethered Phospholipid Bilayers Integrating Functional G-Protein-Coupled Receptor Membrane Proteins. *Langmuir* **33**, 10385–10401 (2017).

19. Green, T. P., Talley, J. P. & Bundy, B. C. Recent Advances in Developing Cell-Free Protein Synthesis Biosensors for Medical Diagnostics and Environmental Monitoring. *Biosensors (Basel).* **15**, 499 (2025).

20. Ando, M., Schikula, S., Sasaki, Y. & Akiyoshi, K. Proteoliposome Engineering with Cell-Free Membrane Protein Synthesis: Control of Membrane Protein Sorting into Liposomes by Chaperoning Systems. *Advanced Science* **5**, 1800524 (2018).

21. Pace, H. *et al.* Preserved Transmembrane Protein Mobility in Polymer-Supported Lipid Bilayers Derived from Cell Membranes. *Anal. Chem.* **87**, 9194–9203 (2015).

22. Liu, H. Y. *et al.* Supported Planar Mammalian Membranes as Models of in Vivo Cell Surface Architectures. *ACS Appl. Mater. Interfaces* **9**, 35526–35538 (2017).

23. Stuebler, M. *et al.* Plant Membrane-On-A-Chip: A Platform for Studying Plant Membrane Proteins and Lipids. *ACS Appl. Mater. Interfaces* **16**, (2023).

24. Liu, H. Y., Chen, W. L., Ober, C. K. & Daniel, S. Biologically Complex Planar Cell Plasma Membranes Supported on Polyelectrolyte Cushions Enhance Transmembrane Protein Mobility and Retain Native Orientation. *Langmuir* **34**, 1061–1072 (2018).

25. Hedger, G., Shorthouse, D., Koldsø, H. & Sansom, M. S. P. Free Energy Landscape of Lipid Interactions with Regulatory Binding Sites on the Transmembrane Domain of the EGF Receptor. *Journal of Physical Chemistry B* **120**, 8154–8163 (2016).

26. Richards, M. J. *et al.* Membrane Protein Mobility and Orientation Preserved in Supported Bilayers Created Directly from Cell Plasma Membrane Blebs. *Langmuir* **32**, 2963–2974 (2016).

27. Berkers, J. A. M., Van Bergen En Henegouwen, P. M. P. & Boonstra, J. Three classes of epidermal growth factor receptors on HeLa cells. *Journal of Biological Chemistry* **266**, 922–927 (1991).

28. Pinilla-Macua, I., Watkins, S. C. & Sorkin, A. Endocytosis separates EGF receptors from endogenous fluorescently labeled HRas and diminishes receptor signaling to MAP kinases in endosomes. *Proc. Natl. Acad. Sci. U. S. A.* **113**, 2122–2127 (2016).

29. Yu, C., Hale, J., Ritchie, K., Prasad, N. K. & Irudayaraj, J. Receptor overexpression or inhibition alters cell surface dynamics of EGF–EGFR interaction: New insights from real-time single molecule analysis. *Biochem. Biophys. Res. Commun.* **378**, 376–382 (2009).

30. Watkins, S. J., Mesyanzhinov, V. V., Kurochkina, L. P. & Hawkins, R. E. The 'adenobody' approach to viral targeting: specific and enhanced adenoviral gene delivery. *Gene Therapy* **4**, 1004–1012 (1997).

31. Björkelund, H., Gedda, L., Barta, P., Malmqvist, M. & Andersson, K. Gefitinib Induces Epidermal Growth Factor Receptor Dimers Which Alters the Interaction Characteristics with 125I-EGF. *PLoS One* **6**, e24739 (2011).

32. Elsner, C., Ergün, S. & Wagner, N. Biogenesis and release of endothelial extracellular vesicles: Morphological aspects. *Annals of Anatomy - Anatomischer Anzeiger* **245**, 152006 (2023).

33. Charras, G. T., Hu, C. K., Coughlin, M. & Mitchison, T. J. Reassembly of contractile actin cortex in cell blebs. *Journal of Cell Biology* **175**, 477–490 (2006).

34. Mills, J. C., Stone, N. L., Erhardt, J. & Pittman, R. N. Apoptotic Membrane Blebbing Is Regulated by Myosin Light Chain Phosphorylation. *Journal of Cell Biology* **140**, 627–636 (1998).

35. Doherty, W., Benson, S., Pepdjonovic, L., Koppes, A. N. & Koppes, R. A. Cell Line and Media Composition Influence the Production of Giant Plasma Membrane Vesicles. *ACS Biomater. Sci. Eng.* **10**, 1880–1891 (2024).

36. Lee, S. H., Meng, X. W., Flatten, K. S., Loegering, D. A. & Kaufmann, S. H. Phosphatidylserine exposure during apoptosis reflects bidirectional trafficking between plasma membrane and cytoplasm. *Cell Death & Differentiation* **20**, 64–76 (2012).

37. Meng, H. & Day, P. J. R. Exploring ethical, sustainable and effective foetal bovine serum alternatives for in vitro mammalian cell culture. *Frontiers in toxicology* **8**, 1776815 (2026).

38. Sahin, U. *et al.* Distinct roles for ADAM10 and ADAM17 in ectodomain shedding of six EGFR ligands. *Journal of Cell Biology* **164**, 769–779 (2004).

39. Cohen, S., Ushiro, H., Stoscheck, C. & Chinkers, M. A native 170,000 epidermal growth factor receptor-kinase complex from shed plasma membrane vesicles. *Journal of Biological Chemistry* **257**, 1523–1531 (1982).

40. Del Piccolo, N., Placone, J., He, L., Agudelo, S. C. & Hristova, K. Production of plasma membrane vesicles with chloride salts and their utility as a cell membrane mimetic for biophysical characterization of membrane protein interactions. *Anal. Chem.* **84**, 8650–8655 (2012).

41. Wioland, H., Jegou, A. & Romet-Lemonne, G. Quantitative Variations with pH of Actin Depolymerizing Factor/Cofilin's Multiple Actions on Actin Filaments. *Biochemistry* **58**, 40–47 (2019).

42. Sarabipour, S., Chan, R. B., Zhou, B., Di Paolo, G. & Hristova, K. Analytical characterization of plasma membrane-derived vesicles produced via osmotic and chemical vesiculation. *Biochimica et Biophysica Acta (BBA) - Biomembranes* **1848**, 1591–1598 (2015).

43. Van De Vijver, M. J., Kumar, R. & Mendelsohn, J. Ligand-induced activation of A431 cell epidermal growth factor receptors occurs primarily by an autocrine pathway that acts upon receptors on the surface rather than intracellularly. *Journal of Biological Chemistry* **266**, 7503–7508 (1991).

44. Varki, A. Biological roles of glycans. *Glycobiology* **27**, 3–49 (2017).

45. Hamai, C., Yang, T., Kataoka, S., Cremer, P. S. & Musser, S. M. Effect of Average Phospholipid Curvature on Supported Bilayer Formation on Glass by Vesicle Fusion. *Biophys. J.* **90**, 1241 (2005).

46. Cytiva. *Biacore Sensor Surface Handbook*. (Cytiva, Uppsala, Sweden, 2022).

Chapter 6: Conclusion and Future Perspectives

6.1 Summary of Dissertation Work

The work presented in the prior chapters of this dissertation was committed to one fundamental goal – to expand the frontiers of biosensing through the development of new materials, biointerfaces, and methodologies. The work was mainly presented through the lens of surface plasmon resonance (SPR), but many of the developments are more broadly applicable to the larger field of biosensing. The first project, dedicated to expanding the range of accessible metals for plasmonic sensing through study of indium thin films nicely illustrates this theme.

While overall aimed at demonstrating the use of indium thin films for SPR sensing, the extensive use of various fabrication and characterization methods provided previously unknown fundamental information about indium that could see more broad application across other biosensing techniques and beyond. This study provided new information about the morphology, oxidation, and optical properties of indium thin films. Additionally, it provided much-needed condensation of the scarce existing information in literature, thus providing a solid base from which to launch future studies utilizing this material.

In the following chapter, we instead leverage existing instrumentation, interfaces, and data processing technologies to characterize the binding behavior of novel monovalent, bivalent, and covalent cancer-targeting therapeutics. SPR is a delicate technique that requires careful consideration of experimental conditions and parameters, along with data processing methods, to accurately assess the binding kinetics of biological interactions. Because of this, there is a strong need for a framework that allows for rapid selection of

experimental factors based on the nature of the binding interactions being measured. Chapter 3 aims to provide this framework from the perspective of analyte valency to the target protein, largely due to the increasing recent recognition of drugs with polyvalent or covalent binding behaviors as potent alternatives to those demonstrating traditional 1:1 binding.

Finally, novel biomimetic lipid interfaces were developed to enable exploration of the effects of membrane composition on transmembrane protein function. This is specifically examined using the well-established regulatory relationship between gangliosides and the cancer-associated epidermal growth factor receptor (EGFR). Synthetically produced and structurally defined gangliosides are integrated into lipid bilayers with highly controlled composition to examine the structure-function relationship of gangliosides in an environment free of the confounding variables to be expected in cellular membranes. The effects of the gangliosides on the binding behavior of EGFR to one of its natural ligands was evaluated using a simplified system whereby the truncated extracellular domain was captured on the surface of the membrane. Little difference in this binding was observed, reinforcing previous work indicating a different regulatory mechanism. However, to confirm these observations, sensing needs to be performed on membranes integrating the full-length EGFR protein, a challenging proposal with initial forays into this area making up the final chapter of this work.

6.2 Future Research Directions

Improved Fabrication and Application of Indium Thin Films

Throughout the work on this project, it was clear that the sensing performance from the perspective of Kretschmann configuration SPR sensing was being negatively impacted by the coarseness of the film. Though we were able to achieve sensitivity approximately 77% that of gold, substantial improvements in both sensitivity and noise could likely be achieved by determining a method for reducing surface roughness.[1] This could theoretically be achieved based on some previous studies that utilized cold substrate temperatures during deposition and/or high temperature annealing while the film was sandwiched between carbon layers.[2] Cold deposition suppresses ordered crystallinity and favors a smoother amorphous film,[3] but achieving deposition on cryogenic substrates does bring practical concerns in terms of instrumental accessibility and throughput. Additionally, other studies using aluminum have indicated that rapid deposition rates and reduced vacuum pressure can aid in improving film uniformity.[4] Despite all of these potential avenues, the current bulk of literature does not provide clear indications that it is possible to generate metallic indium films with optimal thicknesses for SPR without compromising surface roughness.[5]

While achieving metallic indium films with optimal thickness and surface roughness might not be possible, we have demonstrated that Kretschmann configuration sensing is indeed achievable.[6] Furthermore, there is room for improvement based on the aforementioned literature, meaning performance that is competitive with gold films may still be possible. Combining these improvements with SPR excitation by a UV source could

further improve sensing performance, making indium a genuinely viable plasmonic material. Due to indium's ability to achieve SPR response a wide range of excitation wavelengths, similar to aluminum,[7,8] this would also open the door for use in multiwavelength SPR optical setups which provide additional information on a variety of factors such surface layer thickness, bulk refractive index effects, and size of immobilized extracellular vesicles.[9–11] Finally, the presence of the indium oxide layer presents another angle for optimization of films through altering the crystallinity, thickness, or surface chemistry of this layer.

Cellular Study of EGFR Regulation by Gangliosides

For decades, cellular studies have been used to establish and explore the regulatory effects of gangliosides on EGFR. This has most often been achieved through western blot analysis of EGFR phosphorylation before and after cells (most often A431) have been subjected to a treatment. For example, the Hakomori group demonstrated two decades ago that ganglioside inhibition of EGFR was largely specific to GM3, concentration dependent, and likely a result of direct interactions of GM3 with N-glycans on the extracellular domain of the protein using this method.[12,13] However, the many studies conducted in this manner had a limitation of available material and were restricted to naturally sourced ganglioside mixtures containing a variety of structures.

With the vast library of structurally defined and pure gangliosides that were acquired for the studies covered in this work, these methods could be repeated to identify the inhibitory ability of individual GM3 structures. If a structure with an optimal inhibitory effect can be identified, it would provide a strong candidate for ganglioside treatment of

EGFR-positive cancers.[14] Ganglioside treatments have long been proposed but were limited by the availability of pure and defined structures.[15–17] Furthermore, this system could provide insights into the inhibitory mechanism by relating reductions in ligand-dependent phosphorylation to other membrane properties such as lateral diffusion, with additional support being provided by computational studies simulating ganglioside clustering and interaction sights on the protein.[18,19] If this methodology proves itself valuable it could logically be extended to other transmembrane proteins regulated by gangliosides, along with cancer-associated mutations to EGFR such as the exon 19 deletion or exon 20 insertion,[20,21] providing real avenues to ganglioside treatments of cancer.

Full-Length Transmembrane Protein Platforms

While chapter 5 presented work on collecting full-length membrane-bound EGFR in the form of blebs from cell membranes, those goals were very much preliminary inroads toward achieving the ultimate goal of creating an SPR platform that integrates the protein for sensing experiments. Completing this aim will require a great deal further experimentation and will open many other avenues for future research directions – some of which will be related here. Through western blot analysis, it is already clear that the osmotic shock blebs, which were identified as the most optimal for downstream applications, contain large amounts of EGFR. However, some questions about the protein still remain that, when answered, will determine the viability of the method. First and foremost, the activity must be confirmed from two perspectives. Kinase activity (i.e. the ability for the protein to perform phosphorylation) can be confirmed through the usage of commercially available kinase activity kits that operate by measuring the conversion of

ATP to ADP in the presence of an artificial substrate containing many tyrosine moieties.[22] Furthermore, the protein's ability to perform transphosphorylation can be determined by exposing the blebs to EGF and performing a western blot using an antibody specific to autophosphorylated EGFR tyrosine residues such as Tyr1068.[23,24]

With the activity confirmed from multiple perspectives, then the SPR platform integrating the protein will become the goal. There are numerous ways this could be achieved based on existing literature, but these can be generally narrowed down and sorted into two practical categories – capture on a tethered membrane system or the use of polyethylene glycol (PEG) to create a polymer cushioned membrane.[25,26] Extensive work from the Daniel group at Cornell has provided detailed methods for and indicated the practicality of the PEG capture method for forming polymer cushioned membranes with integration of transmembrane proteins that retain lateral mobility.[27–30] Following these capture methods as well as their characterization of protein fluidity and orientation is likely the best starting point for creating the biointerface. Furthermore, some of these methods introduce opportunities to integrate our ganglioside library through either co-rupture or sonication of the blebs with artificial liposomes containing PEG and the ganglioside of choice.

Even if all of these steps can be achieved, there will likely be one major limitation to the blebbing method as it currently exists that will prevent effective SPR sensing of the EGFR-EGF interaction. The magnitude of signal that can be generated is dependent on the ratios of the molecular weights of the ligand and the analyte of interest, as well as the valency of their interaction.[31] Full-length EGFR has a molecular weight in the range of

170-180 kDa depending on the degree of glycosylation; making it approximately 30 times larger than EGF.[32,33] This means that a substantial amount of functional and properly oriented EGFR must be immobilized to generate a useable binding signal from EGF. It is doubtful that the A431 blebs will contain a sufficient concentration of EGFR, meaning that some form of enrichment will likely be necessary. Due to the lack of affinity tags on the protein, this will need to be achieved through immunoprecipitation. Fortunately, a successful method for immunoprecipitation of functional protein from osmotic shock blebs has been previously reported.[34] If this is still insufficient, the expression of transmembrane proteins into membranes using cell-free protein synthesis (CFPS) is an alternative method we have previous attempted with little success. However, our attempts were made with an *E. coli*-based system that may not be compatible with EGFR due to its size and post-translational modification.[35] Future attempts should instead attempt to use insect or mammalian CFPS methods and materials.[36,37] All-in-all, while building this biosensing platform will certainly present many challenges, integration of existing techniques from across literature provides many reasonable pathways to future success.

6.3 References

1. Agarwal, S., Giri, P., Prajapati, Y. K. & Chakrabarti, P. Effect of Surface Roughness on the Performance of Optical SPR Sensor for Sucrose Detection: Fabrication, Characterization, and Simulation Study. *IEEE Sens. J.* **16**, 8865–8873 (2016).

2. Boulesteix, C., Devant, G., Marraud, A. & Rateau, R. Structure and Recrystallization of Indium Thin Film. *J. Vac. Sci. Technol.* **6**, 780–783 (1969).

3. Kurt J. Lesker Company | Physical Vapor Deposition (PVD) of Indium Bumps | Enabling Technology for a Better World. https://www.lesker.com/newweb/ped/applications/indium-bumps.cfm.

4. He, C. *et al.* Sensitive Aluminum SPR Sensors Prepared by Thermal Evaporation Deposition. *ACS Omega* **8**, 43188–43196 (2023).

5. Fan, Z. *et al.* Hydrogen plasma exposure of In/ITO bilayers as an effective way for dispersing In nanoparticles. https://arxiv.org/abs/1611.05606v2 (2016).

6. Ebel, C. P., Stuart, D. D., Valiulis, S. N., Van Zant, W. & Cheng, Q. Indium Plasmonic Thin Films as Substrates for Kretschmann Configuration-Based SPR Sensing and FDTD Analysis of Oxide-Enhanced UV-SERS. *ACS Appl. Nano Mater.* **8**, 23237–23246 (2025).

7. Horák, M., Foltýn, M., Bajo, V., Dub, P. & Šikola, T. Plasmonics of non-noble metals. http://arxiv.org/abs/2603.19996 (2026).

8. Knight, M. W. *et al.* Aluminum for plasmonics. *ACS Nano* **8**, 834–840 (2014).

9. Granqvist, N. *et al.* Characterizing ultrathin and thick organic layers by surface plasmon resonance three-wavelength and waveguide mode analysis. *Langmuir* **29**, 8561–8571 (2013).

10. Rupert, D. L. M. *et al.* Dual-Wavelength Surface Plasmon Resonance for Determining the Size and Concentration of Sub-Populations of Extracellular Vesicles. *Anal. Chem.* **88**, 9980–9988 (2016).

11. Dostálek, J., Vaisocherová, H. & Homola, J. Multichannel surface plasmon resonance biosensor with wavelength division multiplexing. *Sens. Actuators B Chem.* **108**, 758–764 (2005).

12. Haga, Y., Hatanaka, K. & Hakomori, S. itiroh. Effect of lipid mimetics of GM3 and lyso-GM3 dimer on EGF receptor tyrosine kinase and EGF-induced signal transduction. *Biochimica et Biophysica Acta (BBA) - General Subjects* **1780**, 393–404 (2008).

13. Yoon, S. J., Nakayama, K. I., Hikita, T., Handa, K. & Hakomori, S. I. Epidermal growth factor receptor tyrosine kinase is modulated by GM3 interaction with N-linked GlcNAc termini of the receptor. *Proc. Natl. Acad. Sci. U. S. A.* **103**, 18987 (2006).

14. Hegde, M. *et al.* Harnessing potential role of gangliosides in immunomodulation and cancer therapeutics. *Life Sci* **351**, 122786 (2024).

15. Schneider, J. S. GM1 Ganglioside as a Disease-Modifying Therapeutic for Parkinson's Disease: A Multi-Functional Glycosphingolipid That Targets Multiple Parkinson's Disease-Relevant Pathogenic Mechanisms. *Int J Mol Sci* **24**, (2023).

16. Alpaugh, M. *et al.* Disease-modifying effects of ganglioside GM1 in Huntington's disease models. *EMBO Mol Med* **9**, 1537–1557 (2017).

17. Fazzari, M., Lunghi, G., Chiricozzi, E., Mauri, L. & Sonnino, S. Gangliosides and the Treatment of Neurodegenerative Diseases: A Long Italian Tradition. *Biomedicines* **10**, (2022).

18. Sega, M., Vallauri, R., Brocca, P. & Melchionna, S. Molecular dynamics simulation of a GM3 ganglioside bilayer. *Journal of Physical Chemistry B* **108**, 20322–20330 (2004).

19. Lyu, Y. *et al.* Effect of GM1 concentration change on plasma membrane: molecular dynamics simulation and analysis. *Physical Chemistry Chemical Physics* **26**, 12552–12563 (2024).

20. Du, Z. *et al.* Structure-Guided Strategies of Targeted Therapies for Patients with EGFR-Mutant Non–Small Cell Lung Cancer. *Biomolecules* **13**, 210 (2023).

21. Zhang, Z., Stiegler, A. L., Boggon, T. J., Kobayashi, S. & Halmos, B. EGFR-mutated lung cancer: a paradigm of molecular oncology. *Oncotarget* **1**, 497 (2010).

22. A. Haubrich, B. & C. Swinney, D. Enzyme Activity Assays for Protein Kinases: Strategies to Identify Active Substrates. *Curr. Drug Discov. Technol.* **13**, 2 (2016).

23. Schulze, W. X., Deng, L. & Mann, M. Phosphotyrosine interactome of the ErbB-receptor kinase family. *Mol. Syst. Biol.* **1**, MSB4100012 (2005).

24. Carpenter, G. & Cohen, S. Epidermal growth factor. *Journal of Biological Chemistry* **265**, 7709–7712 (1990).

25. Andersson, J. & Köper, I. Tethered and Polymer Supported Bilayer Lipid Membranes: Structure and Function. *Membranes* **6**, 30 (2016).

26. Chiang, P. C., Tanady, K., Huang, L. T. & Chao, L. Rupturing Giant Plasma Membrane Vesicles to Form Micron-sized Supported Cell Plasma Membranes with Native Transmembrane Proteins. *Scientific Reports* **7**, 15139 (2017).

27. Liu, H. Y. *et al.* Supported Planar Mammalian Membranes as Models of in Vivo Cell Surface Architectures. *ACS Appl. Mater. Interfaces* **9**, 35526–35538 (2017).

28. Richards, M. J. *et al.* Membrane Protein Mobility and Orientation Preserved in Supported Bilayers Created Directly from Cell Plasma Membrane Blebs. *Langmuir* **32**, 2963–2974 (2016).

29. Liu, H. Y., Chen, W. L., Ober, C. K. & Daniel, S. Biologically Complex Planar Cell Plasma Membranes Supported on Polyelectrolyte Cushions Enhance Transmembrane Protein Mobility and Retain Native Orientation. *Langmuir* **34**, 1061–1072 (2018).

30. Selivanovitch, E., Ostwalt, A., Chao, Z. & Daniel, S. Emerging Designs and Applications for Biomembrane Biosensors. *Annu. Rev. Anal. Chem.* **17**, 339 (2024).

31. Davis, T. M. & Wilson, W. D. Determination of the Refractive Index Increments of Small Molecules for Correction of Surface Plasmon Resonance Data. *Anal. Biochem.* **284**, 348–353 (2000).

32. Gregory, H. Isolation and structure of urogastrone and its relationship to epidermal growth factor. *Nature* **257**, 325–327 (1975).

33. Ullrich, A. *et al.* Human epidermal growth factor receptor cDNA sequence and aberrant expression of the amplified gene in A431 epidermoid carcinoma cells. *Nature* **309**, 418–425 (1984).

34. Cohen, S., Ushiro, H., Stoscheck, C. & Chinkers, M. A native 170,000 epidermal growth factor receptor-kinase complex from shed plasma membrane vesicles. *Journal of Biological Chemistry* **257**, 1523–1531 (1982).

35. Zemella, A., Thoring, L., Hoffmeister, C. & Kubick, S. Cell-Free Protein Synthesis: Pros and Cons of Prokaryotic and Eukaryotic Systems. *ChemBioChem* **16**, 2420–2431 (2015).

36. Ezure, T. *et al.* A Cell-Free Translocation System Using Extracts of Cultured Insect Cells to Yield Functional Membrane Proteins. *PLoS One* **9**, e112874 (2014).

37. Moghimianavval, H., Hsu, Y. Y., Groaz, A. & Liu, A. P. In Vitro Reconstitution Platforms of Mammalian Cell-Free Expressed Membrane Proteins. *Methods in Molecular Biology* **2433**, 105–120 (2022).